Department of Physics and Astronomy

University of Heidelberg

Master thesis

in Physics

submitted by

Helena Almazán Molina

born in Almería, Spain

2016

Consistencies of the neutron detection efficiency in the Double Chooz reactor neutrino detectors

This Master thesis has been carried out by Helena Almazán Molina

at the

Max-Planck-Institut für Kernphysik

under the supervision of

Prof. Dr. Manfred Lindner

Vereinbarkeitsstudien der Detektionseffizienz von Neutronen beider Double Chooz Reaktorneutrinodetektoren:

Das Double Chooz Experiment befindet sich an einem Kernkraftwerk in Chooz (Frankreich) und analysiert dort das Signal der erzeugten Reaktorantineutrinos. Ziel ist es, eine präzise Messung des Neutrinomischungswinkels θ_{13} durchzuführen, aktuell mit den neuen kombinierten Daten eines nahen und eines fernen Detektors. Dazu ist es wichtig die Nachweiseffizienz der Reaktionsprodukte des Inversen Betazerfalls $\bar{\nu}_e + p \rightarrow e^+ + n$ genau zu kennen. Insbesondere stellt die Effizienz der Neutronendetektion eine dominante Unsicherheit in der Bestimmung von θ_{13} dar. Neben anderen Kalibrationsmethoden liefert die Analyse von Neutronenereignissen einer ^{252}Cf Quelle eine wichtige Messung dieser Effizienz und ihrer Unsicherheit.
Im Rahmen dieser Masterarbeit wurden Daten von ^{252}Cf Messungen in den inneren Detektorvolumina sowie zugehörige Monte Carlo Studien untersucht. Der Prozentanteil von Neutroneneinfängen an Gadolinium (Atome des beladenen Flüssigszintillators) wurde bestimmt und die zeitliche Stabilität, die Übereinstimmung zwischen beiden Detektoren in dieser Größe und die damit verbundenen systematischen Unsicherheiten ermittelt. Des Weiteren wurden Randeffekte des Neutroneneinfangs untersucht. Die dabei erhaltenen Ergebnisse bilden einen wichtigen Beitrag zur Antineutrinoanalyse mit zwei Detektoren.

Consistencies of the neutron detection efficiency in the Double Chooz reactor neutrino detectors:

The Double Chooz experiment, analysing the reactor antineutrinos signal from the nuclear power plant in Chooz (France), aims for a precision measurement of the neutrino mixing angle θ_{13} with the new data collected at the near and far detectors. An accurate and precisely known detection efficiency of the electron antineutrino interaction $\bar{\nu}_e + p \rightarrow e^+ + n$, called inverse beta decay (IBD), is required in order to reach that goal. The correlated signal caused by the IBD interaction requires a good estimation of the neutron detection efficiency, dominant uncertainty in the θ_{13} estimation. Among other calibration methods, the deployment of the ^{252}Cf radioactive source along the detectors' inner volumes is used to understand the behaviour of the neutron captures in the detectors.
The recently collected ^{252}Cf data and Monte Carlo simulations are studied along this thesis. The fraction of n-captures on Gadolinium (atoms loaded in the neutrino target) has been estimated to prove the time stability and consistency between detectors, and to study the behaviour of the neutron captures at the inner volume borders. These results and the performed estimation of the systematic uncertainties of the neutron capture efficiency provide a crucial input for the antineutrino oscillation analysis with two detectors.

Contents

Chapter 1

Neutrino Physics

1.1 Introduction

Radioactivity played an important role during the early decades of the past century. For that reason, the history of the neutrinos began with the investigation of β-decays. Missing energy in the energy spectrum of the emitted electrons started a controversial discussion. In 1930 Pauli [1] postulated the existence of an additional undetectable particle carrying the additional emitted energy. Four years later, Fermi developed the complete theory of the β-decay introducing a new neutral and massless particle: the neutrino ν [2]. In 1953-1959 the study of the reactor neutrinos played a very significant part in its experimental discovery: the first $\bar{\nu}_{\mathrm{e}}$ from a β-decay was detected in a nuclear reactor in the known "Poltergeist Project"[3]. After the next decades, up to three different ν where observed: one for each charged lepton. The ν_μ was postulated be emitted in π-decay by Pontecorvo in 1959 [4], and its first observation was in 1962 [5]. On the other side, the ν_τ was discovered 2001 by the DONUT collaboration [6], some time after the discovery of the τ.

Today the Standard Model (SM) incorporates 3 flavours of light neutrinos (and their antiparticles). They are the partners of the three charged leptons (e, μ, τ), forming the left-handed weak isospin doublets. Neutrinos behave as singlets under U(1) and SU(3) transformations, making them color and electrically neutral. However, they interact weakly via charge-current (CC) interactions and the neutral-current (NC) interactions. As a consequence of the local gauge symmetry in the SM, the total lepton number in these interactions is always conserved.

After some experimental evidences, in the early 60s Pontecorvo suggested the idea of a possible oscillation behaviour between the neutrinos and their own antineutrino $\nu \leftrightarrow \bar{\nu}$ as an analogy of the already known Kaon mixing [7, 8]. Some years later, the Homesake solar neutrino experiments reported a deficit in the solar neutrino fluxes, i.e the measured flux was less than the one expected by the Standard Solar Model. It was called the "solar neutrino problem" and was finally solved with an improved understanding of the properties of neutrinos [9, 10]: the explanation of the deficit was the neutrino oscillation (in this specific case, the disappearance of the electron flavour) and consequently the existence of a non-zero neutrino mass. Nowadays, experiments measuring neutrinos have provided results which demonstrate the occurrence of these transitions from one type of neutrino flavour to another, $\nu_\alpha \rightarrow \nu_\beta$ $(\alpha, \beta = \mathrm{e}, \mu, \tau)$.

Along this chapter, the neutrino oscillation theory is going to be developed for vacuum and matter oscillations. Besides, the search of one of the oscillation angles using reactor experiments will be described.

1.2 Neutrino oscillations

A general neutrino state can be described in terms of the production (flavour) eigenstates $\{|\nu_\alpha\rangle\}$ with $\alpha = e, \mu, \tau$. However, this basis does not correspond with the propagation (mass) eigenstates $\{|\nu_i\rangle\}$ with $i = 1, 2, 3$. One can always connect both bases with an appropriate unitary transformation $\mathcal{U}$:

$$|\nu_\alpha\rangle = \sum_{j=1}^{n} \mathcal{U}_{\alpha j} |\nu_j\rangle \quad , \tag{1.1}$$

where n is the number of light neutrino species. The fact that the flavour basis is not diagonal under the Hamiltonian originates an effective mixing of flavours provided that each mass eigenstate propagates with a different relative phase. After travelling a distance L (or equivalently for relativistic neutrinos, time t), a neutrino originally produced with a flavour α, $|\nu(0)\rangle = |\nu_\alpha\rangle$, evolves as

$$|\nu(\mathrm{L})\rangle = \sum_{\beta\,=\,\mathrm{e},\tau,\mu} \left(\sum_i \mathcal{U}^*_{\alpha i}\, e^{-i\mathrm{E}_i \mathrm{L}}\, \mathcal{U}_{\beta i} \right) |\nu_\beta\rangle \quad , \tag{1.2}$$

where $|\nu(\mathrm{L})\rangle$ corresponds now to the most general ν state. The corresponding phase for each mass eigenstate is given by the relativistic approximation for neutrinos, treated as plane waves $\mathrm{E}_j = \sqrt{p_j^2 + m_j^2} \approx p + m_j^2/2\mathrm{E}$. Hence, the transition probability from an initial state $|\nu(0)\rangle = \nu_\alpha$ to a ν_β state is written as [11]

$$\begin{aligned} \mathrm{P}_{\nu_\alpha \to \nu_\beta}(\mathrm{L}, \mathrm{E}) = |\langle \nu_\beta | \nu(\mathrm{L}) \rangle|^2 = \delta_{\alpha\beta} - 4 \sum_{i>j} \mathrm{Re}\left[\mathcal{U}^*_{\alpha i} \mathcal{U}_{\beta i} \mathcal{U}_{\alpha j} \mathcal{U}^*_{\beta j} \right] \sin^2 \left(\frac{\Delta m^2_{ij} \mathrm{L}}{4\mathrm{E}} \right) \\ - \; 2 \sum_{i>j} \mathrm{Im}\left[\mathcal{U}^*_{\alpha i} \mathcal{U}_{\beta i} \mathcal{U}_{\alpha j} \mathcal{U}^*_{\beta j} \right] \sin \left(\frac{\Delta m^2_{ij} \mathrm{L}}{2\mathrm{E}} \right) \quad , \end{aligned} \tag{1.3}$$

with $\Delta m^2_{ij} = m^2_i - m^2_j$. The case of the survival probability of a flavour state ν_α is then

$$\mathrm{P}_{\nu_\alpha \to \nu_\alpha}(\mathrm{L}, \mathrm{E}) = 1 - \sum_{\alpha \neq \beta} \mathrm{P}_{\nu_\alpha \to \nu_\beta}(\mathrm{L}, \mathrm{E}) \, . \tag{1.4}$$

The mixing matrix $\mathcal{U}$ depends on the choice of parametrization. The standard parametrization of the mixing matrix is given by Pontecorvo-Maki-Nakagawa-Sakata (PMNS) matrix, where the three neutrino flavours are parametrized in terms of the three mixing angles θ_{ij} and the CP violating phase δ:

$$\mathcal{U}_{\mathrm{PMNS}} = \begin{pmatrix} 1 & 0 & 0 \\ 0 & c_{23} & s_{23} \\ 0 & -s_{23} & c_{23} \end{pmatrix} \times \begin{pmatrix} c_{13} & 0 & s_{13} e^{-i\delta} \\ 0 & 1 & 0 \\ -s_{13} e^{i\delta} & 0 & c_{13} \end{pmatrix} \times \begin{pmatrix} c_{12} & s_{12} & 0 \\ -s_{12} & c_{12} & 0 \\ 0 & 0 & 1 \end{pmatrix} \tag{1.5}$$

with $c_{ij} = \cos\theta_{ij}$ and $s_{ij} = \sin\theta_{ij}$. Dominant oscillations are well described by effective two-flavours oscillations. The three-flavour oscillation neutrino effects are suppressed because of the small value of θ_{13} and the hierarchy between the two mass splittings, $\Delta m^2_{21} \ll \Delta m^2_{32}$. Hence, in most of the cases, the problem can be reduced to two-flavour oscillations.

Survival probability in two flavour scenario

In the simplest case of two-flavour mixing, the mixing matrix depends only on one mixing angle θ and a mass squared difference. The probability that a neutrino ν_α with energy E_ν did not oscillate into a neutrino ν_β after a travelling a distance L is then given by

$$P_{\nu_\alpha \to \nu_\alpha}(L, E) = 1 - \sin^2 2\theta \sin^2 \left(\frac{\Delta m^2 L}{4E} \right) . \tag{1.6}$$

This survival probability is the same for neutrinos and antineutrinos, since there are no imaginary entries in the mixing matrix. It has an oscillating behaviour with a period determined by the oscillation length

$$L_{osc} = \frac{4\pi E_\nu}{\Delta m^2} \tag{1.7}$$

which is proportional to the neutrino energy and inversely proportional to the neutrino squared mass difference, and an amplitude proportional to $\sin^2 2\theta$. Experimentally, the free parameters of this oscillation length relation are the source-detector distance and the neutrino energy. Considering a fixed Δm^2 value, three cases have to be considered with respect to a possible observation of oscillations (under Eq. (1.6), see Fig. 1.2.1)

(a) $L/E \ll \frac{1}{\Delta m^2}$: the experiment is too close to the source and the oscillation period is too long (low frequency) to be observed.

(b) $L/E \sim \frac{1}{\Delta m^2}$: this is a necessary condition to observe oscillations and it is the most sensitive region.

(c) $L/E \gg \frac{1}{\Delta m^2}$: several oscillations happen between the source and the detector. In this situation, experiments normally do not measure L/E precisely enough to resolve the oscillation pattern but measure only an averaged transition probability.

Thus, the part of the Δm^2-$\sin^2 2\theta$ parameter space explored in Eq. (1.6) depends on the ration L/E. The most sensitive range of an experiment is at $\Delta m^2 \approx E/L$.

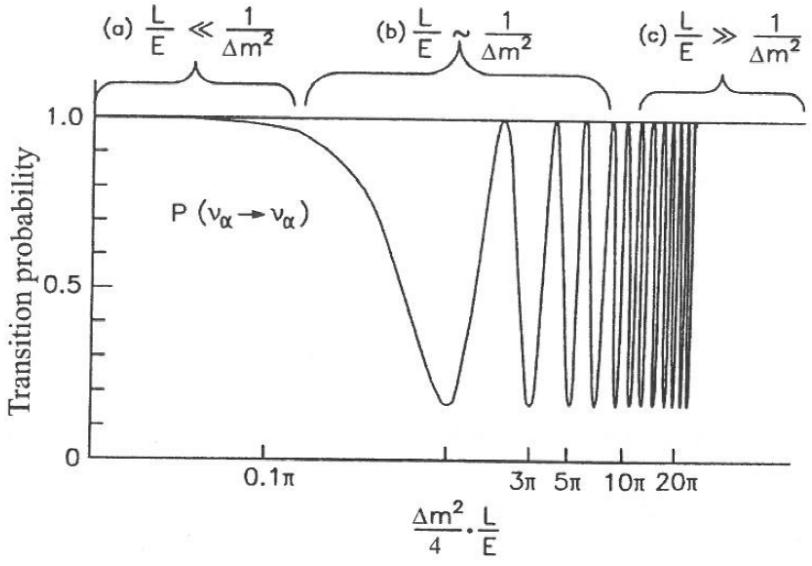

Figure 1.2.1: Logarithmic plot of the oscillation probability as a function of L/E for $\sin^2 2\theta = 0.83$. The braces denote the three possible classes [12].

Neutrino oscillations in matter

When neutrinos propagate through matter, their interactions with the medium can affect the propagation amplitude due to coherent forward scattering on electrons and nucleons. The effect of the medium can be described by an effective potential that depends on the density and composition of the matter. Besides, this potential should be different for each neutrino flavour because their interactions with ordinary matter differ. The effective potential for the evolution of $\nu_{\rm e}$ in a medium with electrons, protons and neutrons is affected by its CC and NC interactions. For ν_μ and ν_τ the potential due to CC interactions is zero, since neither muons nor taus are present in the medium. Consequently, for a given ν_α with $\alpha = {\rm e}, \mu, \tau$ the effective potential for the evolution is

$$V_\alpha \;=\; V_{\rm CC}\delta_{\alpha{\rm e}} + V_{\rm NC} \;=\; \pm\sqrt{2}G_F n_{\rm e}\delta_{\alpha{\rm e}} \mp \frac{\sqrt{2}}{2}G_F n_{\rm n} \quad , \tag{1.8}$$

where $n_{\rm e}$ is the electron number density, G_F is the Fermi constant, $n_{\rm n}$ is the number density of neutrons, and the sign is different for neutrinos and antineutrinos.

In general, the neutrino oscillations in a medium can be described as in vacuum, but with the addition of an effective potential term, as follows:

$$\mathcal{H} \;=\; \mathcal{H}_0 + \mathcal{H}_I \text{ where } \begin{array}{l} \mathcal{H}_0|\nu_i\rangle = {\rm E}_i|\nu_i\rangle \\ \mathcal{H}_I|\nu_\alpha\rangle = V_\alpha|\nu_\alpha\rangle \end{array} \tag{1.9}$$

Considering this matter effect term, the relevant evolution equation for the flavour transition amplitudes is [13],

$$i\frac{\rm d}{{\rm d}x}\Psi_\alpha = \mathcal{H}_{\rm F}\psi_\alpha \quad \text{with} \quad \mathcal{H}_{\rm F} \;=\; \frac{1}{2E}\left(\mathcal{U}\mathbb{M}^2\mathcal{U}^\dagger + \mathbb{A}\right) \quad , \tag{1.10}$$

with

$$\Psi_\alpha = \begin{pmatrix} \psi_{\alpha{\rm e}} \\ \psi_{\alpha\mu} \\ \psi_{\alpha\tau} \end{pmatrix}, \qquad \mathbb{M}^2 = \begin{pmatrix} 0 & 0 & 0 \\ 0 & \Delta m^2_{21} & 0 \\ 0 & 0 & \Delta m^2_{31} \end{pmatrix}, \qquad \mathbb{A} = \begin{pmatrix} 2EV_{\rm CC} & 0 & 0 \\ 0 & 0 & 0 \\ 0 & 0 & 0 \end{pmatrix}, \tag{1.11}$$

where the NC term is not considered because it is irrelevant for the flavour transitions, since it generates a phase common to all flavours. The Hamiltonian matrix in the flavour basis $\mathcal{H}_{\rm F}$ can be diagonalized by an orthogonal transformation $\mathcal{U}_{\rm M}^T\,\mathcal{H}_{\rm F}\,\mathcal{U}_{\rm M} = \mathcal{H}_{\rm M}$ into the mass basis. For a two flavours scenario, with flavours α and β, the mass matrix and unitary matrix are reduced to 2x2 matrices. The oscillation parameters can be described in terms of an effective mixing angle $\theta_{\rm M}$ and the effective squared-mass difference $\Delta m^2_{\rm M}$ in matter as

$$\tan 2\theta_{\rm M} = \frac{\Delta m^2 \sin 2\theta}{\Delta m^2 \cos 2\theta - A} \quad , \tag{1.12}$$

and

$$\Delta m^2_{\rm M} = \sqrt{(\Delta m^2 \cos 2\theta - A)^2 + (\Delta m^2 \sin 2\theta)^2} \quad . \tag{1.13}$$

The quantity $A \equiv 2{\rm E}V_{\rm CC}$ is defined as the potential difference factor between α and β flavours. Depending on the sign of A, the mixing angle in matter can be larger or smaller than in vacuum. For constant potential, the mixing angle and effective masses are constant along the neutrino evolution. Matter effects are important when the potential difference factor A is comparable to the mass difference term $\Delta m^2 \cos 2\theta$, such as in solar oscillations where they played an important role. Nuclear reactor experiments, due to their short baselines, are not sensitive to matter effects.

1.3 The search of the θ_{13}-angle: nuclear reactor experiments

Neutrinos can be produced by natural sources or in an artificial way. On one hand, *natural sources* are for example the atmosphere and the Sun. In the Sun several fusion chains (pp-cycle and the CNO cycle) produce electron antineutrinos. These low energy neutrinos (sub-MeV range) can be detected on the Earth after a travel of $\sim 10^8$ km. Atmospheric neutrinos are produced because of the collision of cosmic rays with atoms of the atmosphere. These neutrinos are detected after a shorter distance than the solar antineutrinos, approximately 10^4 km with energies in the GeV range. On the other hand, neutrinos produced or enhanced on Earth by human processes are called "artificial". *Artificial sources* are accelerators or nuclear reactors. Accelerators can produce ν-pulses in three different ways (π-decay, μ-decay and kaon decay bumps) with different energies (usually in the GeV range). Nuclear reactors are also an artificial source of electron antineutrinos $\bar{\nu}_e$. These are produced in the reactor fission chains, and are emitted from the reactor isotropically. In this case, the energy range of these neutrinos is lower (few MeV). The advantage of the artificial sources is that they can provide a broad range of neutrino energies at lower distances (lower than the solar/atmospheric ones), they have comparably well defined baselines (point like sources) and are monitored on the percent level.

Reactor neutrinos have played a crucial role in neutrino oscillation measurements. They have helped to understand the solar anomaly and they have provided unique information on θ_{13}. Along this section, the properties of the reactor neutrino production and propagation are going to be discussed, so that the ground is settled to explain in upcoming chapters how reactor neutrino experiments can measure the θ_{13}.

1.3.1 Neutrino production in nuclear reactors

Light Water Reactors (LWR) induce fission reactions of fuel isotopes mainly by thermal neutrons. The fuel components contributing to the neutrino production consist of four kind: ^{235}U, ^{239}Pu, ^{238}U and ^{241}Pu. These are bombarded by thermal neutrons, causing an instability in the atom. Consequently, a fission is produced releasing energy ($\sim$ 200 MeV), free neutrons and breaking the fissioning atom in fragments.

A schematic representation of a fission chain for a ^{235}U isotope is shown in Fig. 1.3.1a. This fuel isotope is the most common to undergo fission, and it produces two unequal fragments, and

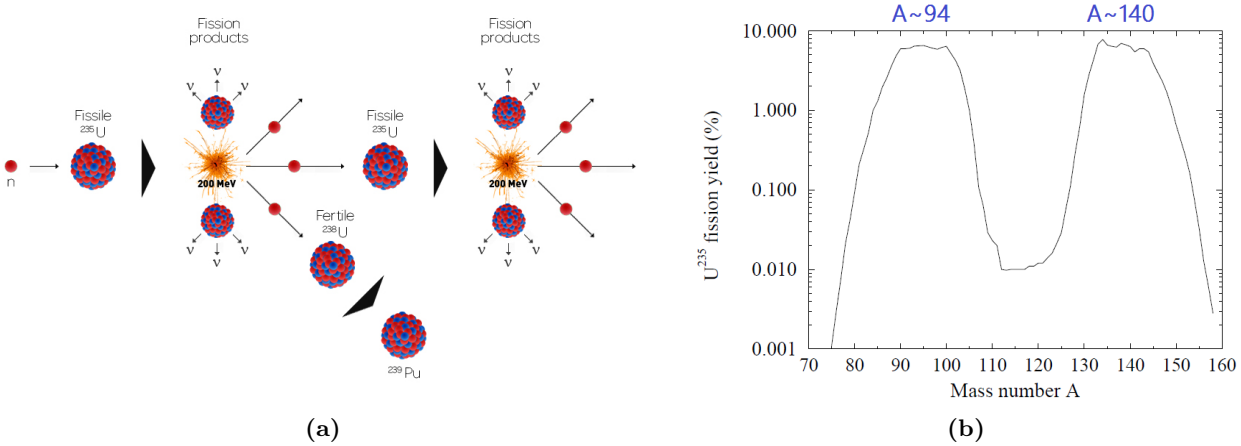

(a) **(b)**

Figure 1.3.1: **(a)** Schematic representation of a fission chain a nuclear reactor [14]. **(b)** Mass distribution of the light fission fragments produced by the fission of ^{235}U [15].

typically two new neutrons that sustain the chain reaction [15],

$$^{235}\mathrm{U} + \mathrm{n} \rightarrow \mathrm{X}_1 + \mathrm{X}_2 + 2\mathrm{n}\,.$$

The mass distribution of the fragments is shown in Fig. 1.3.1b. The lighter fragments correspond to the stable nucleus with $\mathrm{A} \simeq 94$ (e.g. $^{94}_{40}\mathrm{Zr}$) and the heavier to $\mathrm{A} \simeq 140$ (e.g. $^{140}_{58}\mathrm{Ce}$). These two nuclei have together 98 protons and 136 neutrons, while the initial fragments have 92 protons and 142 neutrons. To reach the stability, on average 6 neutrons bound in the fragments have to β^--decay, emitting approximately 6 pure $\overline{\nu}_e$.

Typical modern reactors have a thermal power around $3\,\mathrm{GW_{th}}$, and a flux of $6 \cdot 10^{20}\ \overline{\nu}_e\,\mathrm{core}^{-1}\,\mathrm{s}^{-1}$ is generated. In this way, it is possible to say that reactors are a strong and pure source of neutrinos. The instantaneous fission rates of the four isotopes (^{235}U, ^{239}Pu, ^{238}U and ^{241}Pu) are used as an input for the evaluation of the $\bar{\nu}_\mathrm{e}$ spectrum. Careful measurements of the β spectrum from fission induced by thermal and fast neutrons are performed for all isotopes. Since β-decays are mostly three body decays in which the recoil energy of the daughter nucleus can be neglected, the conversion from a measured beta-spectrum to the neutrino spectrum is possible due to energy conservation adding correction terms. For a single β-branch with endpoint energy Q_β this is given by $\mathrm{E}_{\bar{\nu}_\mathrm{e}} = Q_\beta - \mathrm{E_e}$. New approaches for the calculation of the $\bar{\nu}_\mathrm{e}$ spectra have been presented in Ref. [16] and [17].

1.3.2 Neutrino propagation: survival probability for reactor neutrinos

Reactor electron antineutrinos oscillate after their production and have a survival probability which depends on the mixing parameters in the PMNS matrix (Eq. (1.5)). The pattern of the $\overline{\nu}_\mathrm{e}$ survival probability can be estimated plugging the matrix elements from Eq. (1.5) into Eq. (1.4),

$$\begin{aligned} \mathrm{P}_{\bar{\nu}_\mathrm{e}\rightarrow\bar{\nu}_\mathrm{e}}(\mathrm{L},\mathrm{E}) = 1 &- 4\cos^2(\theta_{12})\cos^2(\theta_{13})\sin^2(\theta_{12})\sin^2(\theta_{13})\sin^2\left(\frac{\Delta m^2_{21}\mathrm{L}}{4\mathrm{E}}\right) \\ &- 4\cos^2(\theta_{12})\cos^2(\theta_{13})\sin^2(\theta_{13})\sin^2\left(\frac{\Delta m^2_{31}\mathrm{L}}{4\mathrm{E}}\right) - 4\sin^2(\theta_{12})\cos^2(\theta_{13})\sin^2(\theta_{13})\sin^2\left(\frac{\Delta m^2_{32}\mathrm{L}}{4\mathrm{E}}\right) \end{aligned} \tag{1.14}$$

In Fig. 1.3.2 a representation of the flavour fraction evolution (from Eq. (1.14)) for an initial $\bar{\nu}_\mathrm{e}$ flux is observed. This expression can be simplified by accounting two considerations. First of all, in the

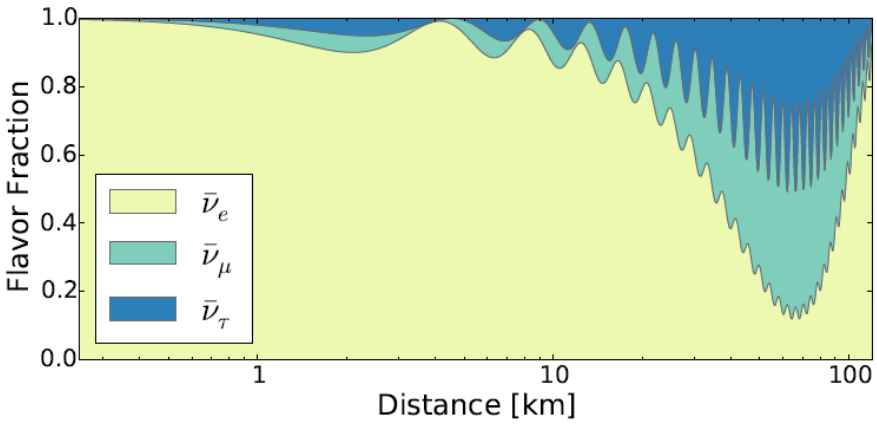

Figure 1.3.2: Flavour fraction evolution of an initially $\overline{\nu}_\mathrm{e}$ flux [18].

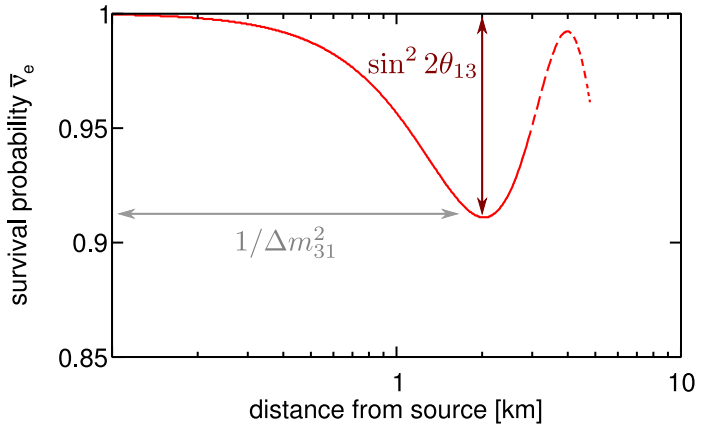

Figure 1.3.3: Electron antineutrino survival probability for $E_\nu = 4\,\text{MeV}$ [14].

1 km baseline reactor experiments the L/E ratio has a specific value $\sim 5 \cdot 10^2$ km/GeV. Secondly, $|\Delta m^2_{ij}|$ is known, and in this case $|\Delta m^2_{31}| \gg |\Delta m^2_{21}|$. Consequently, the survival probability for an electron antineutrino can be approximated to

$$P_{\bar{\nu}_e \to \bar{\nu}_e}(L, E) \simeq 1 - \sin^2 2\theta_{13} \sin^2 \left(\frac{\Delta m^2_{31} L}{4E_\nu} \right) . \tag{1.15}$$

The probability has been simplified to the two flavour scenario depicted in Eq. (1.6). Now the oscillation amplitude comes in terms of the mixing angle θ_{13} and the oscillation length in terms of L/E and Δm^2_{31}. Hence for a given experiment with a known L/E ratio, and a Δm^2_{31}, the mixing angle θ_{13} can be easily estimated measuring the survival probability amplitude of a reactor antineutrino flux (see Fig. 1.3.3). Note that matter effects are not relevant for reactor neutrino experiment with short baselines [13].

1.3.3 θ_{13} experiments

Reactor experiments are perfectly designed for a precise estimation of θ_{13}. It is computed with the observed to expected electron antineutrino ratio for a certain L/E and a given value of the Δm^2_{31} parameter. The independence of the CP phase and θ_{23} allows a high precision measurement.
In the 1990's two first-generation kilometer-baseline reactor experiments, CHOOZ and PALO VERDE tried to measure θ_{13}. The CHOOZ detector was built at the Chooz power plant of Électricité de France in the Ardennes region of France. It took data from April 1997 until July 1998. The PALO VERDE detector was built at the Palo Verde Nuclear Generating Station in the Arizona desert of the United States. It took data between October 1998 and July 2000. Neither experiment was able to observe the $\overline{\nu}_e$ deficit caused by θ_{13} oscillation. As a result, only an upper limit of $\sin^2 2\theta_{13} < 0.15$ at 90% C.L. could be established for a $|\Delta m^2_{13}| = 2.4 \cdot 10^{-3}\,\text{eV}^2$ [18]. The null results from these experiments combined with the measured values of θ_{23} and θ_{12} motivated many phenomenological speculations of neutrino mixing parameters. A direct consequence of a vanishing θ_{13} is that CP violation in the leptonic sector would never be observed in neutrino oscillation experiments. The importance of knowing the precise value of θ_{13} triggered a series of world-wide second generation kilometer-baseline reactor experiments in the 21st century, including Double Chooz in France, RENO in Korea and Daya Bay in China. Table 1.3.1 summarizes some of the key parameters of the five mentioned experiments (first and second generation) and in Fig. 1.3.4 a better picture about how the second generation of experiments are configured is shown.

Table 1.3.1: Key parameters of the five past and present reactor θ_{13} experiments, including the thermal power, flux baseline, and target mass [18].

	Power [GW_{th}]	Baseline [m]	Mass [tons]
CHOOZ	8.5	1050	5
PALO	11.6	750	12
VERDE		890	12

	Power [GW_{th}]	Baseline [m]	Mass [tons]
Double	8.5	400	8
Chooz		1050	8
RENO	16.8	290	16
	1380	16	
Daya Bay	17.4	360	2x20
		500	2x20
		1580	4x20

Both (the first and second generation experiments) are placed underground, and a common technology is used as $\overline{\nu}_e$ detection target: a gadolinium-loaded liquid scintillator. The addition of near detectors at baselines of a few hundred meters is one of the most significant improvement of the second-generation experiments over the previous ones. The uncertainty in predicting the reactor antineutrino flux is relatively large, although it can be greatly diminished by the relative measurement between near and far detectors. Compared to the first-generation, the second-generation have much larger signal statistics by using higher power reactors (Daya Bay and RENO) and larger detectors. The underground sites are deeper to allow better shielding from cosmogenic background. Better chemical recipes of the gadolinium-loaded liquid scintillator also improve the overall detector performance and long term stability. The second-generation reactor experiments have been a huge success. In 2011 Double Chooz reported the first hint of $\overline{\nu}_e$ disappearance at kilometer baselines after only a few months running [19], and in 2012 Daya Bay and RENO confirmed it. The precision of the θ_{13} measurement improved quickly with more data, where the current best combined value is $\sin^2 2\theta_{13} = 0.085 \pm 0.005$ [20].

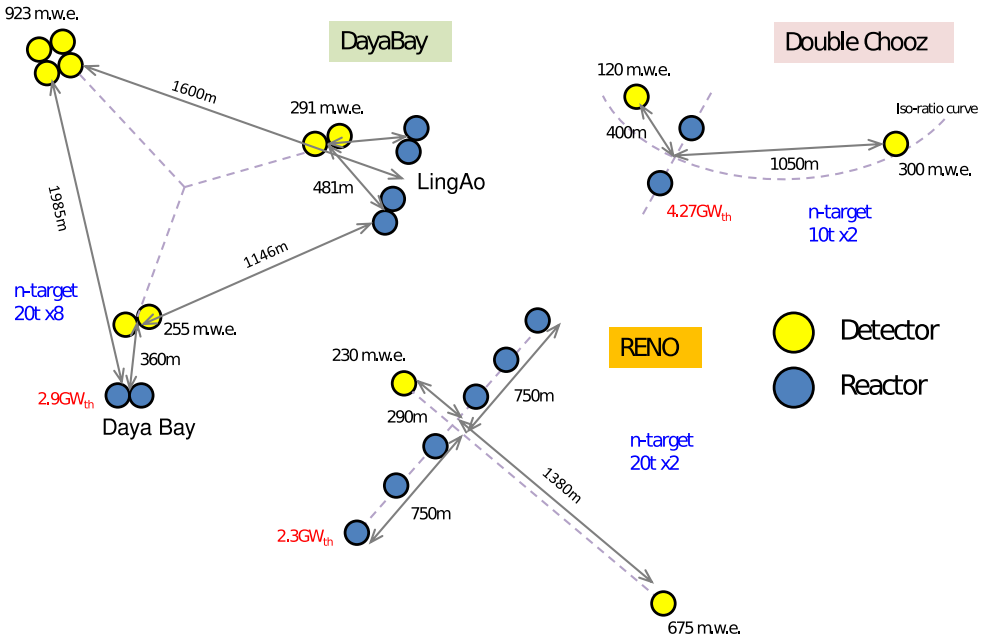

Figure 1.3.4: Configuration for three kind of reactor experiments: Daya Bay (China), RENO (Korea) and Double Chooz (France). The reactor-detector properties of these experiments are collected in Table 1.3.1 [21].

Chapter 2

The Double Chooz experiment

The Double Chooz (DC) experiment is located at the Électricité de France (EDF) nuclear power plant in Chooz (France). There are two identical in DC: the so-called Near Detector (ND) measures the emitted neutrino flux at ∼400 m distance from the two reactor cores producing each 4.25 GW_{th} thermal power; the other one, called Far Detector (FD) is placed at 1050 m distance measuring the oscillated flux. The FD commenced its operation in April 2011, built in the experimental hall of the preceding CHOOZ experiment. The construction of the ND was finished out at the end of 2014. Up to now, summer 2016, the Double Chooz Collaboration published measurements of the θ_{13} using only the data from the single far detector, by the comparison of the measured neutrino rate and spectral shape to a prediction. With the recently collected data from both ND and FD detectors a new physics result has been provided by the relative comparison of both detectors measured neutrino rate [22]. In the next subsections, the detectors' set-up and the detection principle are described together with the analysis developed for the estimation of θ_{13}.

2.1 Detector description

2.1.1 Detector set-up

The Double Chooz detectors (Fig. 2.1.1) are calorimetric liquid scintillator detectors optimized for detection of reactor neutrinos. Both detectors are located underground, being covered by 300 and 120 meter water equivalent (m.w.e) overburden respectively for the FD and the ND. Their volume is divided in several layers: the inner detector, the inner veto veto and the outer veto.

Inner detector. Three inner concentric cylindrical vessels form the inner detector (ID), where the neutrino is expected to interact. The inner most volume, named *ν-target*, has a diameter of 2300 mm and is filled with 10 m^3 Gd-loaded liquid scintillator. The scintillator mixture (n-dodecane, PXE, PPO, bis-MSB and 1g Gd/l as beta-diketonate complex) has been chosen setting the radio-purity and a long term stability as priorities [23]. The ν-target is surrounded by a 8 mm thick transparent acrylic vessel, separating it from a 550 mm thick Gd-free liquid scintillator layer, called the *γ-catcher*. This volume of 3416 mm of diameter is used to detect the γ-rays escaping from the ν-target, for that reason the light yield was chosen to provide identical photoelectron yield across these two layers [24]. A *buffer* of 105 cm thick non-scintillating mineral oil is outside the γ-catcher acrylic vessel. 390 low background 10-inch photomultiplier tubes (PMTs) are positioned on the inner surface of the buffer tank, and are used to detect the radiative signal from the ν-target and the γ-catcher. Besides, the buffer oil shields from radioactivity of photomultipliers and of the surrounding rock. The buffer volume is surrounded by a steel tank and optically separated from the outer layers described below.

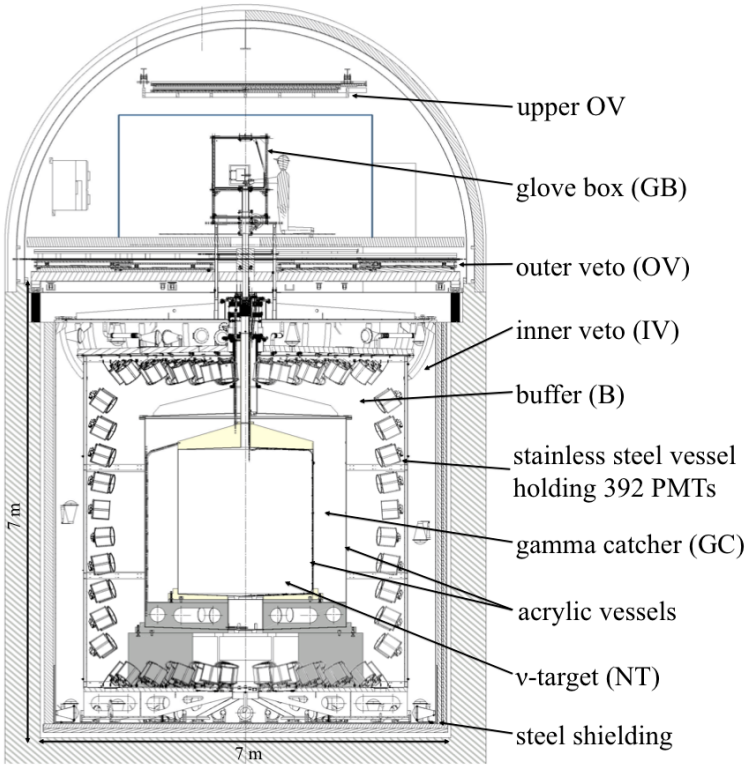

Figure 2.1.1: Schematic view of the Double Chooz detector [35].

Inner veto. Outside of the ID there are the veto systems. The first is a 50 cm thick liquid scintillator layer called the inner veto (IV). The IV is equipped with 78 8-inch PMTs. It works not only as an active veto to cosmic rays muons but as a shield to fast neutrons produced outside of the detector. In addition, fast neutrons can be often tagged by the IV since the recoil of protons is visible in a scintillator detector.
The whole main detector (ID + IV) is further surrounded in the FD by a 15 cm thick steel shield to protect it against external γ-rays (and in the near detector by a 1 m water shielding instead). Each inner PMT from the inner detector and the inner veto is surrounded by a mu-metal to suppress the magnetic field from the Earth [26]. A central chimney, connected to all layers, allows the introduction of the liquids and calibration sources.

Outer veto. An outer veto (OV) made of plastic scintillator covers the top of the detector tank [27]. Each plastic scintillator strip has a cross section of (5×1) cm, and forms an array of orthogonally oriented strips covering a (13×7) m area (except for around the Chimney, where an *upper outer veto* is additionally installed). This external part of the detector is built in order to veto the cosmic rays that do not hit the active regions of the ID.

2.1.2 Calibration devices

Several calibration methods are used in order to either study the detection systematic uncertainties in the neutrino measurement or to test the detector response.

- As part of the normal data taking routine, a calibration is performed in the Double Chooz detectors using *multi-wavelength LED fiber-systems*. These light injection (LI) systems are used to illuminate the ID and the IV volumes from a set of fixed points mounted on the PMT

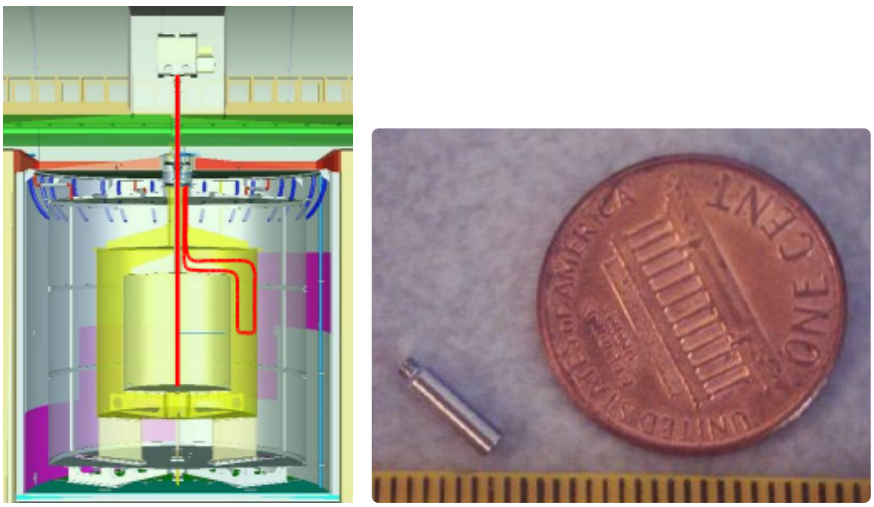

(a) **(b)**

Figure 2.1.2: **(a)** Source deployment systems. **(b)** Source encapsulation [28]

covers. Analysing these data, it is possible to test the readout electronics, mainly time offset and PMTs gain and their stability during the operation.

- Radio-isotopes can be deployed in the detector via two calibration systems (see Fig. 2.1.2a red lines): a tube along the symmetry axis of the ν-target (*z-axis* deployment system) and a *Guide Tube* along the boundaries of the ν-target and the Buffer (inside of the γ-catcher). Several calibration sources are used in the Double Chooz calibration (Fig. 2.1.2b): ^{68}Ge, ^{137}Cs, ^{60}Co, and ^{252}Cf. The ^{252}Cf is used, among other duties, to evaluate systematic uncertainties on the detection efficiency of neutron captures on Gd.
- Besides the LI system, a laser ball system has been used to illuminate ID PMTs through an optical fiber and to measure the speed of light inside the detector liquids.

In addition to these calibration devices, background events can be used for various calibration purposes: spallation neutrons captured on Hydrogen, Carbon and Gadolinium nuclei and residual natural radioactivity e.g. Bi-Po coincidences from the Uranium and Thorium series in the liquid scintillator. These events are homogeneously distributed in the detector volume, and constantly observed in the data taken. For that reason, they are suitable to extract information on both time stability corrections and energy scale position dependence.

2.2 Reactor neutrino detection

Reactor electron antineutrinos are produced with an upper limit energy of about 10 MeV. Considering the threshold energies for the CC interactions of the three antineutrino flavours in Table 2.2.1, the Double Chooz detectors can only be sensitive to *inverse beta decays* (IBD). This process happens when an electron antineutrino interacts with a proton, creating a positron and a free neutron, $\overline{\nu}_e + p \rightarrow e^+ + n$. The mentioned threshold energy of this process is given by [15]

$$E_{th} = \frac{(m_e + M_n)^2 - M_p^2}{2M_p} = 1.806\,\text{MeV} \quad . \tag{2.1}$$

IBD interactions are possible in the DC liquid scintillators because Hydrogen nuclei can be considered to be similar to free protons. The cross-section of this process is analytically known. It

Table 2.2.1: Threshold energies for the different CC interactions of antineutrinos [13].

Reaction	$E^{th}_{\bar{\nu}_e}$
$\bar{\nu}_e + p \rightarrow n + e^+$	1.81 MeV
$\bar{\nu}_\mu + p \rightarrow n + \mu^+$	110.16 MeV
$\bar{\nu}_\tau + p \rightarrow n + \tau^+$	3.45 GeV

is estimated from the neutron lifetime, and expressed in terms of the electron antineutrino energy $E_{\bar{\nu}_e}$ [29],

$$\sigma_{IBD}(E_{\bar{\nu}_e}) = K \cdot (E_{\bar{\nu}_e} - \Delta)\sqrt{(E_{\bar{\nu}_e} - \Delta)^2 - m_e^2} \tag{2.2}$$

with the difference in rest mass between a neutron and a proton $\Delta = M_n - M_p = 1.293\,\text{MeV}$ and the constant $K = 0.961 \cdot 10^{-43}\,\text{cm}^2/\text{MeV}^2$ (including the neutron lifetime from MAMBO-II measurement [30]). The resulting IBD energy spectrum detectable by the DC detectors is plotted in Fig. 2.2.1a. It has the product form of the IBD cross section σ_{IBD} from Eq. (2.2) and the emitted spectrum from the reactor.

The IBD reaction products are detected in organic liquid scintillators via a correlated signal. A coincidence signal in the detector enables to discriminate between a neutrino event and background. It is divided in two processes, related to the e^+ and n interactions (See Fig. 2.2.1b):

1. **Prompt event:** The positron slows down losing its kinetic energy within picoseconds and it eventually annihilates with an electron of the liquid scintillator. The visible energy of this process is measured in the ID. It results in a signal of,

$$E_{vis,e^+} = E_{kin} + 2m_e \simeq E_{\bar{\nu}_e} - \Delta + m_e = E_{\bar{\nu}_e} - 0.782\,\text{MeV} \quad ,$$

   where a small neutron recoil energy is considered. Therefore, a direct detection of the E_{vis,e^+} allows to estimate $E_{\bar{\nu}_e}$. The observed positron spectrum has the same resolution and energy loss as the electron antineutrino energy distribution in Fig. 2.2.1a. This property enables the spectrum analysis of the neutrino oscillation.

2. **Delayed event:** The neutron slowly thermalizes by scatterings on Hydrogen atoms. Approximately $\sim$ 30µs later, it is captured in the detector target. In most of the cases it occurs on Gd-nuclei, but it can also happen on Hydrogen nuclei. The capture process excites the nucleus, producing a short-lived excited state that quickly decays releasing the excess energy as a gamma cascade [31]. For Gd-captures this sum of gammas amounts to $E_{tot\text{-}\gamma} \approx 8\,\text{MeV}$,

$$n + Gd \rightarrow Gd^* + \gamma' s\,(\sum_i E_{\gamma,i} \sim 8\text{MeV}) \quad .$$

   On Hydrogen nuclei it yields a single gamma with 2.224MeV,

$$n + H \rightarrow d + \gamma\,(E_\gamma \sim 2.2\text{MeV}) \quad .$$

   The γ-rays which escape from the target region (Gd-captures can only occur in the ν-target) deposit their energy in the γ-catcher scintillator. Therefore, the original energies of the neutrino and the Gd signals can be obtained by the sum of the scintillation lights from both the ν-target and the γ-catcher.

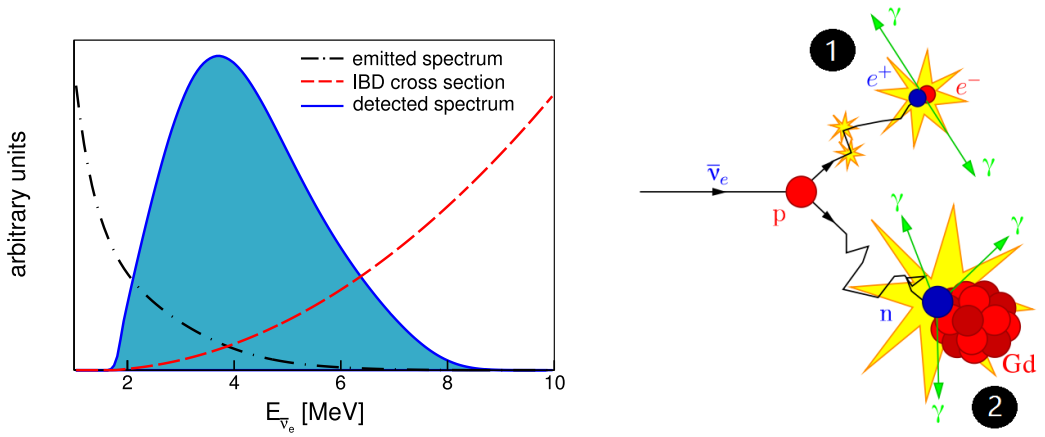

Figure 2.2.1: **(a)** Neutrino spectrum detected via IBD reactions. Blue shape is the product of the emitted reactor spectrum (black dashed line) and the IBD cross section (red dashed line). *(Image courtesy of Antoine Collin).* **(b)** Depicted IBD reaction.

The neutrino signal is identified by the delayed coincidence of the positron and the neutron capture signals. Neutrino selection considers as delayed signal the Gd neutron captures. As the Gd signals happens only in the neutrino target, the fiducial volume cut based on the position reconstruction is not necessary (avoiding its associated uncertainty). However, a neutrino selection considering also H neutron captures is feasible. The systematic uncertainty is slightly worse due to event isolation (low energy events are more sensitive to be misidentified as background events, and are not easy to neglect because correlation times are higher). But taking into account these events the statistics become 3 times larger. Since the events in the Hydrogen and Gadolinium samples are statistically almost independent, the accuracy of the θ_{13} measurement improves by combining both detection channels.

2.3 Data analysis

Observed events in the Double Chooz detectors are recollected from the PMTs signal measurement, with some basic information about the data taking process. These signals are reconstructed, in order to test later if they are real electron antineutrino candidate events. In the next subsections, the event reconstruction process [32], and the electron antineutrino selection [32]-[33] are described. In addition, it is detailed how the Double Chooz oscillation analysis is performed in order to estimate a value of θ_{13}.

2.3.1 Event reconstruction

The collected data from the Double Chooz measurements is initially given in binary files, containing information about the waveforms, trigger, run, and data taking conditions. In case of the MC production, simulated events are provided with the same file format than the data. These data and MC files are processed with event reconstruction algorithms in order to create and fill variables used for later analyses. The set of algorithms are made in order to reconstruct the event's *muon track*, *vertex* and *energy*. After the event reconstruction processing, the MC simulation files additionally include among others "truth" information (like true energy, position and particle type).

Pulse reconstruction

During the pulse reconstruction the charge signal and time for each PMT is extracted from the digitized waveform recorded by the flash-analog to digital converter (ADC). Periodic triggers are taken in order to compute the mean ADC counts of the baseline ($B_{\rm mean}$) and its fluctuation as standard deviation ($B_{\rm rms}$) for each readout channel. The integrated charge q is defined as the sum of ADC counts during the integration time window after $B_{\rm mean}$ is subtracted. In order to avoid noise fluctuations identified as signal, some conditions are required

- at least 2 ADC counts are required in the maximum bin,
- and the integrated charge q should be $> B_{\rm rms} \cdot \sqrt{N_{\rm s}}$, where $N_{\rm s}$ is the number of samples in the integration window.

Charge and time in the MC simulation are extrated as for data.

Vertex reconstruction

The vertex position for each event in the detector is reconstructed using a maximum likelihood algorithm for the event likelihood $\mathcal{L}(x, y, z, t, \Phi) \equiv \mathcal{L}(\mathsf{X})$, written in terms of position, time and light intensity per unit solid angle. For this estimation, the observed charge and time for each PMT are used, and the events are assumed to be a point-like light source. The best possible set of X is found by maximizing $\mathcal{L}(\mathsf{X})$, which is equivalent to minimizing the negative log-likelihood function

$$F_{\rm V} = -\ln \mathcal{L}(\mathsf{X}) \quad . \tag{2.3}$$

Calibration data is used to tune the effective light attenuation and PMT angular response, in order to have the same performance in data and MC files.

Energy reconstruction

The first ingredient in the energy reconstruction analysis ($\rm E_{vis}$) is the total number of photoelectrons (PE) $N_{\rm pe}$. It is obtained from the charge-to-PE conversion factor g_i^m considering

$$N_{\rm pe} = \sum_i q_i / g_i^m(q_i, t) \quad , \tag{2.4}$$

where i refers to each readout channel and m refers to either data or MC. The integrated charge by the pulse reconstruction (q_i) and the g_i^m conversion factor are calculated from calibration data, taking into account the variation in the course of data taking (t, elapsed days). The total number of PE is converted into energy considering the absolute energy scale conversion factor $f^m_{\rm MeV}$. It is estimated using the 2.224 MeV peak of neutrons captured on H using the data taking with a ^{252}Cf neutron source deployed at the center of the detector. In addition to these two terms, the visible energy is reconstructed like

$$\mathrm{E_{vis}} = N_{\rm pe} \times f_{\rm u}^{\rm data}(\rho, z) \times f_{\rm MeV}^{\rm data} \times f_{\rm s}(\mathrm{E}^0_{\rm vis}, t) \quad \text{for the data} \quad , \tag{2.5}$$

and

$$\mathrm{E_{vis}} = N_{\rm pe} \times f_{\rm u}^{\rm MC}(\rho, z) \times f_{\rm MeV}^{\rm MC} \times f_{\rm nl}(\mathrm{E}^0_{\rm vis}) \quad \text{for the MC} \quad , \tag{2.6}$$

where some correction terms f are applied for the next reasons:

- A uniformity calibration term $f_{\rm u}^m(\rho, z)$ is considered in order to correct the position dependence of $N_{\rm pe}$. It is estimated using γ's from spallation neutrons captures on Hydrogen nuclei. A similar pattern is seen in the correction map for data and MC.

- The visible energy of the data is corrected with $f_{\rm s}(\mathrm{E}^0_{\rm vis}, t)$ for time variation of the mean gain and detector response. For this pourpose, muon-induced spallation neutrons captures on Gd- and H-nuclei and Bi-Po coincidences are used.
- With the correction factor $f_{\rm nl}(\mathrm{E}^0_{\rm vis})$ MC files correct non-linearities produced by charge (QNL) and light (LNL). The QNL correction is associated with the modeling of the readout system and charge integration algorithm, and to measure it calibration data from the ^{252}Cf source at center is used. The LNL correction arises from the scintillator modeling and it is evaluated with calibration data as well.

Muon track reconstruction

Cosmic muons passing through the detector often create isotopes in the ν-target by spallation interactions. Two muon tracking algorithms are used in the Double Chooz analysis in order to identify these particles: the first uses the spatial pattern of the PMTs hit times in the ID, and the second uses the full detector information (ID, IV and OV).

2.3.2 Neutrino selection

The neutrino selection algorithm is implemented in order to select IBDs from the large amount of events produced by background sources. During neutrino selection several steps has been applied in order to suppress the large fraction of recorded events caused by cosmic muons, sporadic light emissions from the PMTs (called *light noise* [34]) and natural radioactivity. The remaining background contributions are studied thoroughly and several vetoes are applied to suppress them.

IBD candidate selection

The IBD events are selected in two steps. First of all, a set of cuts are applied to data in order to select the valid trigger events, such that events caused by light noise effects and cosmic muons can be suppressed. Secondly, the correlated neutrino candidate selection is applied.

1. Valid trigger selection: a valid trigger event is considered if it

- has an energy **0.3 < E(ID) < 100 MeV**.
- is **NOT a muon trigger:** a muon trigger is defined from combination of following three conditions as:
  - *IV response condition*: a total charge of Q >500 000 digital charge units (DUQ) for the far detector and Q>30 000 DUQ for the near detector is observed.
  - or *IV trigger logic condition*: at the trigger-level, the event is tagged as μ.
  - or *ID response condition*: the energy in the inner detector is >100 MeV (same value for far and near detectors).
- is **NOT a random trigger.**
- is **NOT a μ-correlated trigger:** time reference to last muon Δt > 1 000 µs.
- is **NOT a light noise trigger event:** when
  - The ratio of the largest amount of charge seen by a single PMT and the total charge is smaller than a threshold value, Qmax/Qtot < 0.2.
  - The standard deviation of the pulse arrival times $\sigma_{\rm t}$ and the PMT charges $\sigma_{\rm p}$ are lower than an estimated value, $\sigma_{\rm t} < 36$ or $\sigma_{\rm q} < (1680 - 28\sigma_{\rm t})$.
  - The charge over all the PMTs with maximal distance of 1m to the PMT with largest change Qmax is lower than a threshold, Qdiff < 100 000.

2. IBD candidate selection: after the primary cuts, the IBD candidates are selected by requiring of a prompt-delayed coincidence signal. Depending on the detection channel, the selection cuts are different. In Table 2.3.1 the selection cuts for the latest published Double Chooz analyses using the Gadolinium and Hydrogen selection channels are summarized. For the prompt events, the Hydrogen selection presents a minimum energy cut. This cut is implemented to avoid events where only one of the e^-e^+ annihilation γ's is detected from an IBD coincidence signal in the detector Buffer. For Gd events these kind of events do not occur because γ's are detected in the γ-catcher. The neutron captures from the IBD events are selected by a different cut on the energy of the delayed coincidence signal: Gd captures selected around the 8 MeV, and Hydrogen capture events with an interval based on the energy capture at 2.2 MeV. The cut on the prompt to delayed correlation time (Δt) is determined based on the mean neutron capture time in the ν-target scintillator liquid. Gd-captures occur with a capture time of $\sim 30\mu s$, and for the Hydrogen analysis the upper correlation time cut is enlarged to $800\mu s$ to account for the $\sim 200\mu s$ lifetime of the neutron captures in the γ-catcher liquid. Accidental coincidences are suppressed by a cut on the correlation distance (ΔR). For a H-channel they are the main source of background, and for that reason the cut on the correlation distance is up to 120 cm (additional cut is applied in order to avoid accidental events in the H-analysis, see next "Background" subsection). An additional cut is implemented in order to isolate the coincidence signal. In the time window presented in the event isolation line no events should be observed before the prompt event, and only the delayed candidate event should be the only preceding trigger.

Table 2.3.1: Criteria of the neutrino candidate selection in the last published Gd- and H-analyses using the far detector data [32, 33].

	Gd-selection	**H-selection**
Prompt energy	$0.5 < E_p < 20\,MeV$	$1.0 < E_p < 20\,MeV$
Delayed energy	$4 < E_d < 10\,MeV$	$1.3 < E_d < 3\,MeV$
Corr. time	$0.5 < \Delta t < 150\,\mu s$	$0.5 < \Delta t < 800\,\mu s$
Corr. distance	$\Delta R < 100\,cm$	$\Delta R < 120\,cm$
Event isolation	$[-200, +600]\mu s$	$[-800, +900]\mu s$

In the latest (unpublished) Gd-analysis in the Double Chooz detectors (called DC-IV Gd-analysis, see more information in Subsection 2.3.3) the same IBD selection criteria as in Table 2.3.1 is considered. In this case, the event isolation cut is going to be moved from $[-200, +600]\mu s$ to $[-600, +600]\mu s$ to better isolate the prompt event from possible background trigger events.

Backgrounds

The remaining background events after the IBD selection cuts are caused by correlated background events originating from cosmic muon processes. In order to suppress them, some vetoes need to be applied in addition to the IBD selection cuts. The different background sources and the way to veto them are listed below:

- **Cosmogenic isotopes**: Long-lived isotopes (^{9}Li and ^{8}He) produced by cosmic muon spallation on ^{12}C atoms (abundant in organic compounds of the liquid scintillators and vessel acrylics) are β-n emitters. The energy deposition of these β emission can be misidentified as a prompt event, while the neutron capture on H- or Gd-nuclei creates the delayed energy deposition.
  $\Rightarrow$*Li+He veto*: A ^{8}Li likelihood is estimated for each combination of prompt event and preceding muon based on: distance between the event vertex position to the muon track and the number of neutron candidates following the muon. This veto is applied on the prompt

event selection, and in the last publication it rejected 1.12 ± 0.05 events/day (a 55% of the cosmogenic background estimation) [32].

- **Fast neutrons and stopping muons**: Fast neutrons are generated by cosmic muon spallation in the surrounding rock which penetrate the detector. Recoiling protons can be misidentified as prompt signal, while the preceding neutron capture forms the delayed event. These fast neutrons on their way to the ID can deposit energy in the IV scintillator and can be vetoed. Muons entering the detector through the chimney can be stopped in the ν-target (stopping muons) decaying into a Michel electron/positron and a muon-neutrino. The muon track then mimics the prompt signal.
  ⇒*F_V veto*: Stopping-μs and light noise events can have PMT patterns different to the common physics delay events. For that reason the F_V value (see Eq. (2.3)) has been studied for this purpose, where it has been observed that it becomes larger for events which have a different hit pattern.
  ⇒*OV veto*: Stopping-μs can also be excluded by a OV veto: prompt signal coincidence with a OV event.
  ⇒*IV veto*: Fast-n and stopping-μs events often deposit energy in the IV (below the threshold of the muon identification). They can be reduced by the consideration of an IV veto: considering a distance cut between the ID and IV reconstructed events vertices.
  ⇒*Multiciply Pulse Shape (MPS) veto*: Fast-n can be tagged using the waveform of all the PMT signals. A new cut is included considering small energy depositions in the ID, which can be due to other recoil protons before the main signal in the same FADC window.

The neutrino selection, and the previously mentioned vetoes are focused on filtering the correlated background events, but false coincidences can be among the selected set of candidates. These false coincidences are caused by two uncorrelated events accidentally passing the cuts. These remaining background contribution can be measured by means of a "off-time window method", selecting delayed candidates with 1s offset to a prompt. Dead times affecting the standard neutrino selection are accounted for by application of correction factors. On H-analysis, accidentals are the main source of background events and are additionally suppressed by a multi-variable analysis based on an Artificial Neural Network (ANN). It exploits the fact that the distributions of the delayed energy and time and space correlation of the accidental events differ from the IBD ones.

2.3.3 Oscillation analysis

The θ_{13} value can be estimated from the deficit in the measured IBD candidates compared to the reactor prediction of non-oscillated neutrinos. In the Double Chooz experiment several analysis frameworks have been used in order to perform the estimation of θ_{13}. As the construction of the Double Chooz experiment has been developed in two phases, different analysis configurations have been used in consideration of the detector data taking. Besides, several detection channel techniques have been used for the θ_{13} analysis fit.

Data sets

During the Double Chooz detector data taking, different analysis configurations have been put forward. The current different analysis configurations used in the Double Chooz analyses are labelled DC-I, DC-II, DC-III and DC-IV. In Table 2.3.2 the properties of these analysis configurations are summarized. For DC-I, II and III analyses only far detector data had been considered. The latest DC-IV analysis is including the recent near detector data and consequently a multi-detector analysis. Besides, the run times in each of them are different. The oscillation analyses considered all

Table 2.3.2: Data sets for the different Double Chooz oscillation analyses.

Analysis Configuration	Analysis Type	Detection Channel	Live Time [days] FD-I	FD-II	ND
DC-I	Single Detector	Gd-I [19]	96.8	-	-
DC-II	Single Detector	Gd-II [35]	227.93	-	-
		H-II [25]	240.1	-	-
DC-III	Single Detector	Gd-III [32]	460.67	-	-
		H-III [33]	460.67	-	-
DC-IV	Single + Multi-Detector	Gd-IV [22]	460.67	212.47	150.76

possible neutrino detection channels: Gd- and H-selection channels. In the DC-IV the Gd-analysis channel is currently performed.
Note that these data sets and detection channels for the neutrino search also differ in the analysis techniques, such as energy scale calibration or methods for background rejection.

Fit analyses

Different analysis frameworks were developed and applied in the analysis configurations to extract the oscillation parameter θ_{13} from Eq. (1.15). All of them are based on the minimization of a χ^2 statistics.

Rate+shape (R+S) analysis: studies the energy dependence of the neutrino oscillation deficit. The measured IBD candidate rate is compared to the predicted rate within different energy regions for the prompt visible energy. The binned rate and spectra shape χ^2 definition for separated energy bins of variable size can be simplified in the given form by [35],

$$\chi^2_{\mathrm{R+S}} = \sum_{i,j}^{\mathrm{Bins}} (N_i^{\mathrm{obs}} - N_i^{\mathrm{pred}})(M_{ij})^{-1}(N_j^{\mathrm{obs}} - N_j^{\mathrm{pred}})^T + \chi^2_{\mathrm{Pulls}} + \chi^2_{\mathrm{Off}} \quad , \tag{2.7}$$

where

- $N_{i,j}$ is the number of events observed in each prompt spectrm i, j bin using far or near detector data;
- $N_{i,j}^{\mathrm{pred}}$ is the predicted number of antineutrinos,

$$N_{i,j}^{\mathrm{pred}} = \sum_{R=1,2}^{\mathrm{Reactors}} P_{\bar{\nu}_{\mathrm{e}}\to\bar{\nu}_{\mathrm{e}}}(\theta_{13}) \cdot N_i^{\mathrm{exp},R} \cdot \prod_{e}^{\mathrm{Eff.}} \varepsilon_e + \sum_{b}^{\mathrm{Bkg}} N_i^b \tag{2.8}$$

  considering the expected number of antineutrinos from the two reactors $N_i^{\mathrm{exp},R}$, the survival probability, the four detection efficiencies ε_e (prompt and delayed events, vetoes, and proton number efficiencies), and the three backgrounds N_i^b;
- M_{ij} is the covariance matrix including the related uncertainties to the source and the different backgrounds;
- χ^2_{Pulls} considers other parameters which can modify the $N_{i,j}^{\mathrm{pred}}$ (such as correlated background rates, Δm^2_{31});
- χ^2_{Off} corresponds to a Poisson likelihood term for the reactor-off data.

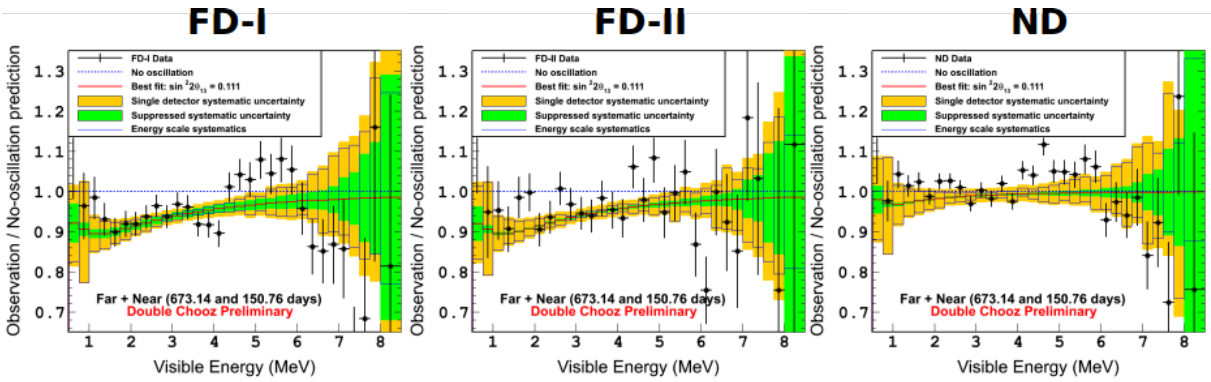

Figure 2.3.1: Ratio of the background subtracted data to the unoscillated prediction for FD-I, FD-II, and ND data samples in the DC-IV Gd-analysis [22]. The best fist result considering the three fitls for the $\sin^2 2\theta_{13}$ is the one summarized in Table 2.3.3.

In order to obtain the best fit value of θ_{13}, the χ^2 of Eq. (2.7) is scanned in $\sin^2 2\theta_{13}$, minimizing over the pulled parameters. The survival probability is considering the Δm^2_{31} from the MINOS experiment as $2.4^{+0.09}_{-0.10} \times 10^{-3}\text{eV}^2$ assuming normal hierarchy [36]. The obtained values of $\sin^2 2\theta_{13}$ for the latest DC publications are summarized in Table 2.3.3, presenting consistent results of $\sin^2 2\theta_{13}$ between them. A frequentist approach was used to exclude in all off them the no-oscillation hypothesis at a certain C.L., given in Table 2.3.3 in the last column. In Fig. 2.3.1 the energy dependence of the neutrino oscillation is plotted for the far detector (divided in 2 samples FD-I and FD-II) and the near detector data. In the three distributions the deficit up to 4 MeV is interpreted as the observation of electron antineutrino disappearance. The spectrum distortion above 4 MeV does not affect the θ_{13} measurement and is not further discussed in this thesis.

Table 2.3.3: Results for the DC publications [19, 35, 32, 22, 25, 33] using Rate+Shape fit analysis..

	$\sin^2 2\theta_{13}$	$\chi^2/d.o.f$	null-oscillation excluded at
Gd-I	$0.086 \pm 0.041\,(\text{stat}) \pm 0.030\,(\text{syst})$	23.7/17	94.6 % C.L.
Gd-II	$0.109 \pm 0.030\,(\text{stat}) \pm 0.025\,(\text{syst})$	42.1/35	99.8 % C.L.(2.9σ)
Gd-III	$0.090^{+0.032}_{-0.029}\,(\text{stat+syst})$	52.2/40	99.9 % C.L.(3.2σ)
Gd-IV	$0.111 \pm 0.018\,(\text{stat+syst})$	128.8/120	5.8σ
H-II	$0.097 \pm 0.034\,(\text{stat}) \pm 0.034\,(\text{syst})$	38.9/30	97.4 % C.L.(2.0σ)
H-III	$0.124^{+0.030}_{-0.039}\,(\text{stat+syst})$	69.4/38	–

Reactor Rate Modulation (RRM) analysis: this fit is a background model independent rate only analysis. It allows to extract the total background rate and θ_{13} simultaneously. The neutrino mixing angle θ_{13} is estimated by the comparison of the observed rate of IBD candidates with the expected one for different reactor power conditions (two reactors are on, one of the reactors is off, and both reactors are off). In the RRM analysis, the data set is divided into seven bins by the reactor thermal power conditions: one bin in the 2 reactor off period, three bins with mostly 1 reactor off, and three bins with 2 reactors off. As in the R+S fit, the RRM analysis minimize the χ^2 defined as follows [32]:

$$\chi^2_{\text{RRM}} = \chi^2_{\text{on}} + \chi^2_{\text{off}} + \chi^2_{\text{bg}} + \frac{\varepsilon^2_{\text{d}}}{\sigma^2_{\text{d}}} + \frac{\varepsilon^2_{\text{r}}}{\sigma^2_{\text{r}}} + \frac{\varepsilon^2_{\nu}}{\sigma^2_{\nu}} \quad , \quad \text{where} \tag{2.9}$$

- χ^2_{on} is the term with the six contributions of reactor-on data, considering the expected rates according to the values of the systematic uncertainties parameters;

- $\chi^2_{\rm off}$ considers the reactor-off data contribution, given by the sum of residual $\bar{\nu}_{\rm e}$ rate and background rate multiplied by the live-time;
- $\chi^2_{\rm bg}$ is the background systematic fit statistic;
- and the other three parameters are the detection, reactor flux and residual neutrinos efficiency terms.

A $\chi^2_{\rm RRM}$ scan of $\sin^2 2\theta_{13}$ is carried out minimizing it with respect to the total background rate and three systematic uncertainty parameters for each value of $\sin^2 2\theta_{13}$. The best fit in the DC-III H-analysis was for $\sin^2 2\theta_{13} = 0.095^{+0.038}_{-0.039}$ and a total background rate of $B = (7.27 \pm 0.49)$events/day, with $\chi^2_{\rm min}/d.o.f = 7.4/6$. This result is in agreement with the obtained values from the R+S analysis in Table 2.3.3. And as they use different information – energy spectrum shape and reactor rate modulation, to extract θ_{13} – they can work as a cross-check to each other.

For the θ_{13} estimation the measurement of the background ratios (and their uncertainty) and the detection efficiency terms is important in order to give a precise computation. Along this thesis, the detection efficiency is going to be evaluated considering the emitted neutrons by a ^{252}Cf source. In Chapter 3, the californium source properties and the way to selected the neutron events are going to be explained. Besides, the neutrino detection efficiency terms will be developed. In Chapter 4 and 5 the neutrino detection efficiency results in the ν-target and γ-catcher volumes are summarized. Furthermore, the estimated efficiency parameters for the preliminary DC-IV Gd-analysis (presented in Table 2.3.3) are going to be estimated.

Chapter 3

The ^{252}Cf calibration source

In the Double Chooz experiment, there are three neutron sources available for calibration: spallation neutrons, inverse beta decay neutrons and the ^{252}Cf source. While the IBD and spallation neutrons are captured in the entire detector volume, the ^{252}Cf source allows us to study the neutron capture behavior in a specific point in the detector. During the first part of this chapter, the properties of this source and the way to select the neutron events will be explained. Secondly, how these events can be useful in the neutrino detection efficiency is developed.

3.1 Cf source data

Californium [37] (Cf, A = 98) is a radioactive element from the actinide series, named by the University of California. It is a gray or silvery white metal, with a density greater than the density of lead. It does not occur in nature, therefore particle accelerators and nuclear reactors are used for its production. Some of the Cf isotopes can undergo spontaneous fission accompanied by neutron emission. The most common one is Californium-252 (^{252}Cf), being the most stable among the others with a life-time of $\tau = 3.816\,\text{yr}$. This element in 97% of the time decays through alpha decay, whereas the 3% of the times it decays via spontaneous fission. In these kind of processes, the excitation energy is emitted via neutron emission and/or gamma-radiation.

Neutrons: These particles are emitted in 99% of the time due to strong excitation of the fission fragments (termed as prompt neutrons) with a life-time of $< 10^{-14}\,\text{s}$ and a mean number of $\overline{\text{n}} = 3.757 \pm 0.005$ neutrons/fission [38]. Their energy distribution depends on the production mechanism, and the most widely applied analytical expressions describing the experimental data are the Watt distribution [39] and the Maxwellian distribution [40]. In Fig 3.1.1 prompt neutron spectra are compared to the Maxwellian distribution behavior, obtaining an averaged neutron energy of $\overline{\text{E}} = 2.13 \pm 0.01\,\text{MeV}$.
Beside these prompt neutrons, delayed neutrons can also be emitted ($\sim 1\,\%$ of the time) from β-decays of the fission fragments into daughter nuclei with an excess of neutrons [38].

Gammas: γ-quanta can be produced as a consequence of the final stage of de-excitation of fission fragments. The time of a γ emission is in the order of $10^{-9} - 10^{-11}$ s, and the expected mean energy of each γ-quanta is about 1 MeV [38]. Several studies have been performed in order to estimate the mean energy of each γ-quantum as well as the total energy relased in form of γs. In Table 3.1.1, some of the obtained values are presented.

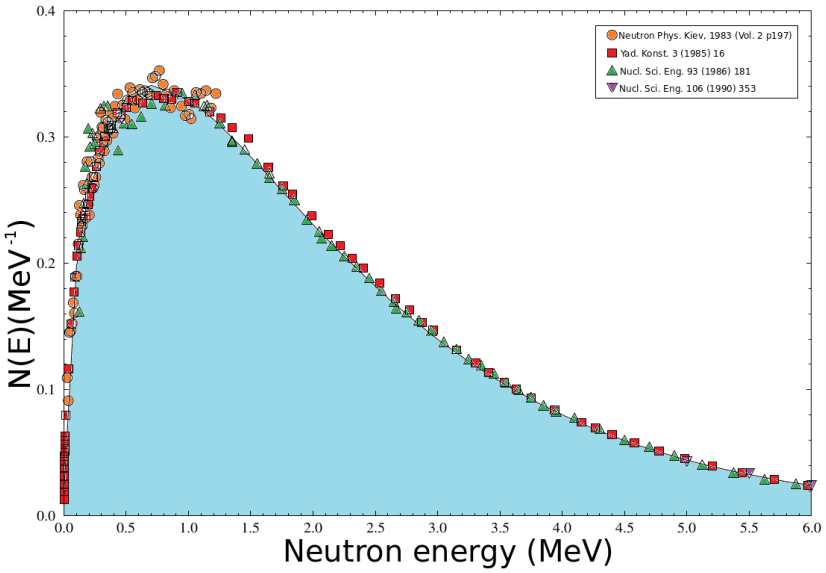

Figure 3.1.1: Prompt neutron spectrum from spontaneous fission of ^{252}Cf. The shaded area corresponds to the Maxwellian distribution, and the different points to several Cf neutron spectra estimations. Maxwellian and Watt distributions describe the experimantal data closely, only differing significantly in the region close to $\approx$ 10 MeV. It is possible to see that the most probable kinetic energy is at 0.7 MeV [38].

Table 3.1.1: Parameters of prompt γ-rays from ^{252}Cf nuclear fission, considering the left columns for energy and time measurement ranges [38].

Range of measurement		**Total energy**	**Number of γs**	**Energy per γ**
ΔE [MeV]	Δt_{max} [ns]	$\overline{E}_{\gamma}^{tot}$ [MeV]	$\overline{N}_{\gamma}$	$\overline{E}_{\gamma}$ [MeV]
-	3	8.2	10.3	0.8
0.14-10	10	6.84 $\pm$ 0.30	7.8 $\pm$ 0.4	0.88 $\pm$ 0.04
0.3-10	10	6.56	6.53	1.0
>0.114	12	7.0 $\pm$ 0.3	9.7 $\pm$ 0.4	0.72
>0.29	12	6.35	6.64	0.95

This sequence of emitting neutrons and γ-quanta is due to the considerably higher probability of neutron emission. According to this concept, the mean energy for γ-radiation per fission should be close to the mean binding energy of neutrons in the primary fission fragments (5 MeV).

3.1.1 Detector deployment

The ^{252}Cf source used in Double Chooz is customized and made at the University of Alabama and double-sealed in an inner and outer cylindrical capsule both of 2 mm radius (both capsules made of stainless steel). In the Double Chooz experiment the radioactive sources can be introduced in the detector using the deployment systems explained in the section 2.1 (a Z-axis one in the ν-target and a Guide Tube in the γ-catcher). Since the beginning of far detector operation, five calibration campaigns have been realized using the ^{252}Cf source (Table 3.1.2). The first two campaigns are enclosed by the DC-III data sample runs, only with the far detector running. The third calibration campaign data (also only in the far detector) is not part of the DC-III data taking period, and it is not considered in the DC-IV data set. The last two calibration campaigns (fourth and fifth calibration campaigns) are part of the DC-IV data samples, including calibration data in both far and near detectors.

Table 3.1.2: Calibration campaigns using a Cf source in the Double Chooz detectors. The information about the run numbers, deployment positions and run length can be found in Appendix A.

Calibration Campaign	Far Detector	Near Detector
1st	2011, August	–
2nd	2012, June-July	–
3rd	2013, June	–
4th	2015, August-October	
5th	2016, April	

3.1.2 Event selection

Considering the emitted particles by the ^{252}Cf source and their properties, an event selection can be applied to the calibration data in order to tag the Californium spontaneous fission events. The first event observed in the detector are the fission fragments gammas. This emission does not start until the neutrons have evaporated off the fission fragments. But the neutron capture cross section depends on the energy and it does not become significant until the neutrons have thermalized (for more information, see Appendix B). For those reasons, fission gammas correspond to the *prompt event* observed in the detector. Subsequently, neutron captures (on Gd, C or H nuclei) are detected in coincidence with the prompt gamma event. Only the events succeeding the prompt trigger in a defined time window will be tagged as *delayed events* (neutron captures). Considering all of this, the events are selected in the next steps:

1. Valid trigger selection: In order to avoid possible backgrounds an initial valid trigger selection is applied. The considered cuts are based in the DC-IV Gd selection, see the list below:

- **0.3 < E(ID) < 100 MeV**
- **NOT a muon trigger:** a muon trigger s defined from combination of following three conditions as:
  - I*V response condition*: a total charge of Q >500 000 DUQ for the far detector and Q>30 000 DUQ for the near detector is observed.
  - or *IV trigger logic condition*: at the trigger-level the event is tagged as μ.
  - or *ID response condition*: the energy in the inner detector is >100 MeV (same value for far and near detectors).
- **NOT a random trigger**
- **NOT a light noise trigger:** events recognized when
  - The ratio of the largest amount of charge seen by a single PMT and the total charge is smaller than a threshold value, Qmax/Qtot < 0.2.
  - The standard deviation of the pulse arrival times σ_t and the PMT charges σ_p are lower than an estimated value, $\sigma_t < 36$ or $\sigma_q < (1680 - 28\sigma_t)$.
  - The charge over all the PMTs with maximal distance of 1m to the PMT with largest change Qmax is lower than a threshold, Qdiff < 100 000.
- **NOT a μ-correlated trigger:** time reference to last muon $\Delta t > 1\,000$ µs.

2. ^{252}Cf coincidence selection: In a last step, taking into account the fission gammas and neutron captures visible energy and correlation time, a Cf coincidence selection is applied (Fig. 3.1.2).

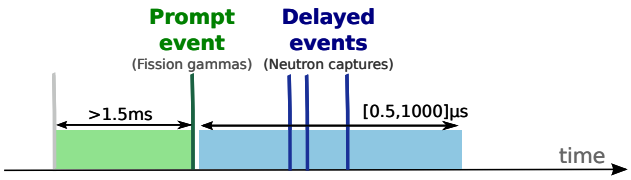

Figure 3.1.2: Representation of the ^{252}Cf fission events selection.

- **Prompt event** (fission gammas):
  - $4 < E_{vis} < 10$ MeV
  - at least after 1.5 ms with reference to the last trigger event
- **Delayed events** (neutron captures):
  More than 1 event can occur (multiplicity > 1) with the next properties:
  - $0.5 < E_{vis} < 25$ MeV
  - $0.5 < \Delta t < 1\,000$ μs

As the visible energies between the prompt and the delayed event are in the same energy range, for the fission gamma events a 1.5 ms time cut with reference to the last trigger event is applied. Also an energy criteria between [4, 10] MeV is taken into account. The fission gammas with energies lower than 4 MeV are neglected because they could be contaminated with correlated and accidental backgrounds (more information in [41]). For the delayed neutron capture events, an open energy criteria is considered ([0.5,25] MeV) and a correlated time cut is applied.

3.1.3 Accidental background subtraction

Due to its clear and powerful signal, the Californium events are expected to be almost background free compared to the IBD events. Nonetheless, when the neutron capture energy spectra is compared to the MC simulations, some discrepancies can be observed at large correlation time and distances (observed in Fig. 3.1.3b and 3.1.3c, concretely on the asymmetry plots), which corresponds to accidental coincidences fulfilling the ^{252}Cf selection criteria. There are several types of events unrelated to the source's fissions that can produce an uncorrelated false coincidence. Some possible accidental background combinations are:

1. **Single events** considered as **prompt** are correlated with a real delayed fission events.
2. Fission event (prompt and delayed) where a **single event** is considered as **delayed subevent**.
3. **Two single events** forming a false coincidence.
4. **Two fission events** occurring too close in time, that the delayed events can be mixed up.

A possible way to measure accidental events is using a technique already implemented in other Double Chooz analyses: the *off-time window method*, depicted schematically in Fig. 3.1.5. In this method, when a real fission event happens (on-time event) virtual prompts are simulated after a specific time Δt_{vp} (where vp comes from virtual prompt). In their corresponding delayed window (called off-time window) single candidates are searched, considering the Californium selection criteria. If a single event is observed in this window, it is considered as a background event. These background events will from now on be named off-time events. In order to increase the statistics not only a single off-time window is 'opened', but several off-time windows related to the same prompt event are used in the off-time events search.

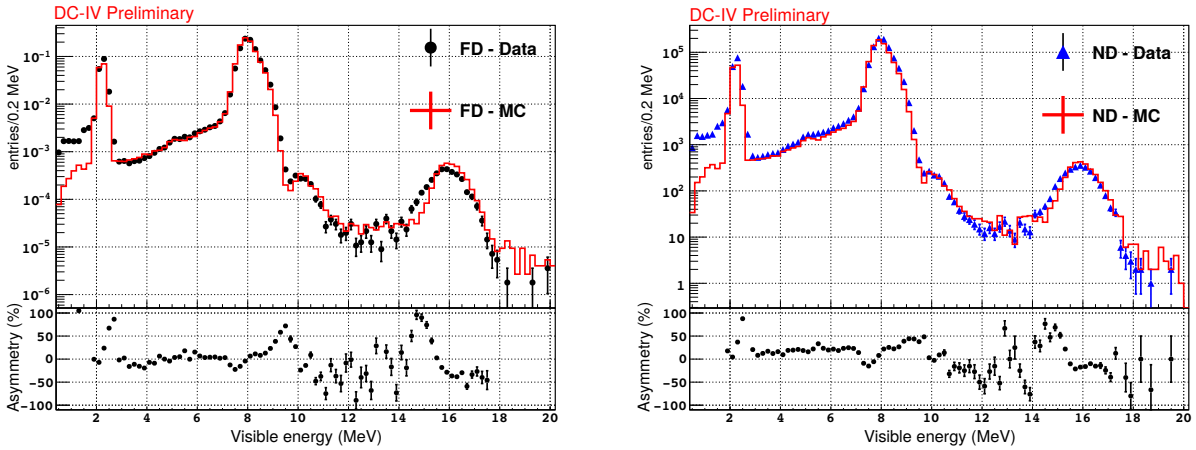

(a) Delayed visible energy.

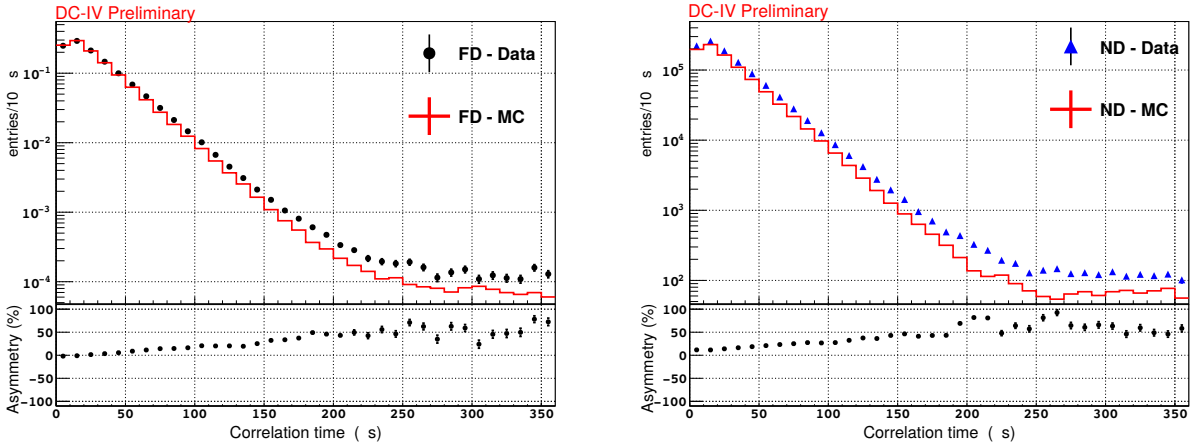

(b) Prompt-Delay correlation time.

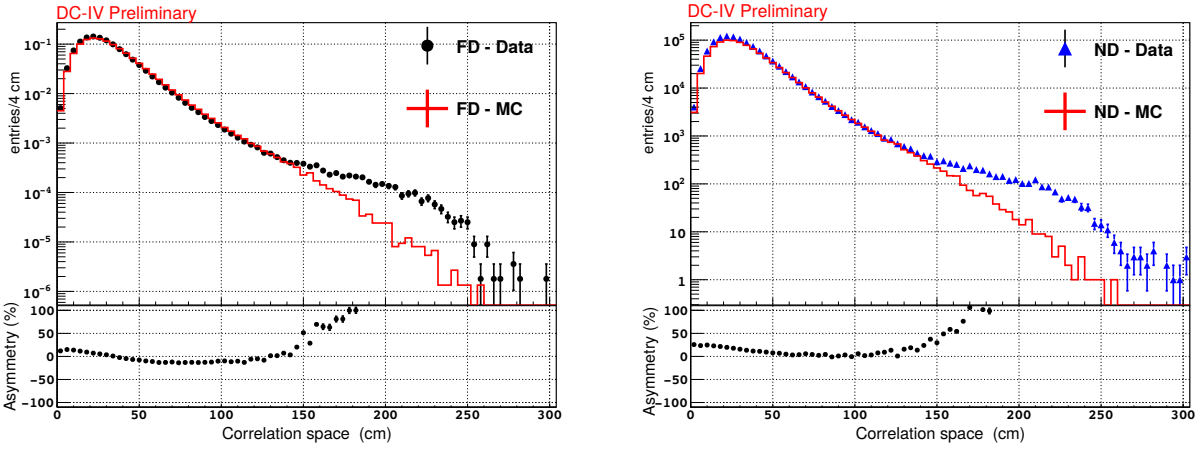

(c) Prompt-Delay correlation distance.

Figure 3.1.3: Data and simulation spectra of the 5th ^{252}Cf calibration campaign at the detector center, (x, y, z) = (0,0,12)mm. *Left plots* correspond to FD and *right plots* to the ND. Plots scaled to the amount of events on the delayed visible energy **(a)** range between [7, 10] MeV. Asymmetry plots corresponds to $2 \cdot \frac{A-B}{A+B}$ where A (B) are FD (MC) number of events. Prompt fission gammas spectra not shown because of imperfect gamma spectrum modeling in the MC, which has no impact on the analysis.

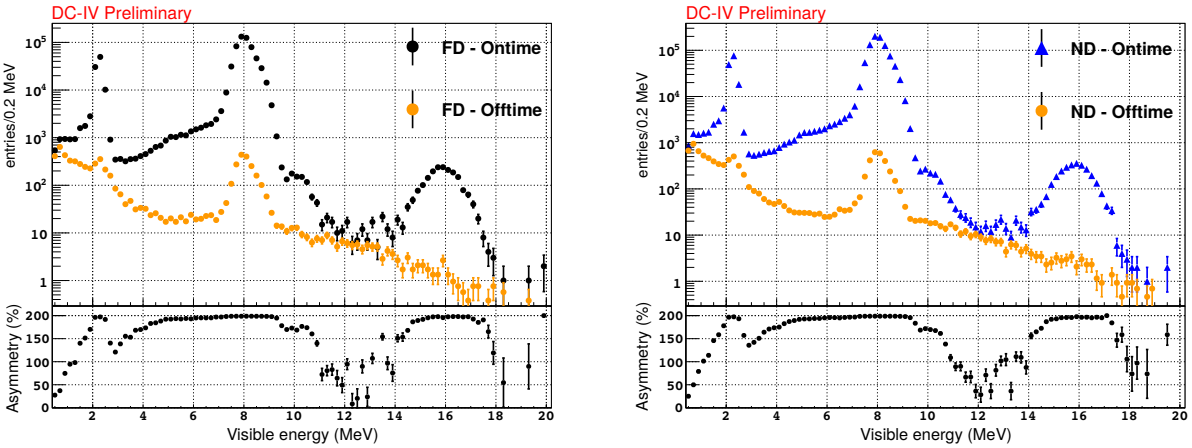

(a) Delayed visible energy.

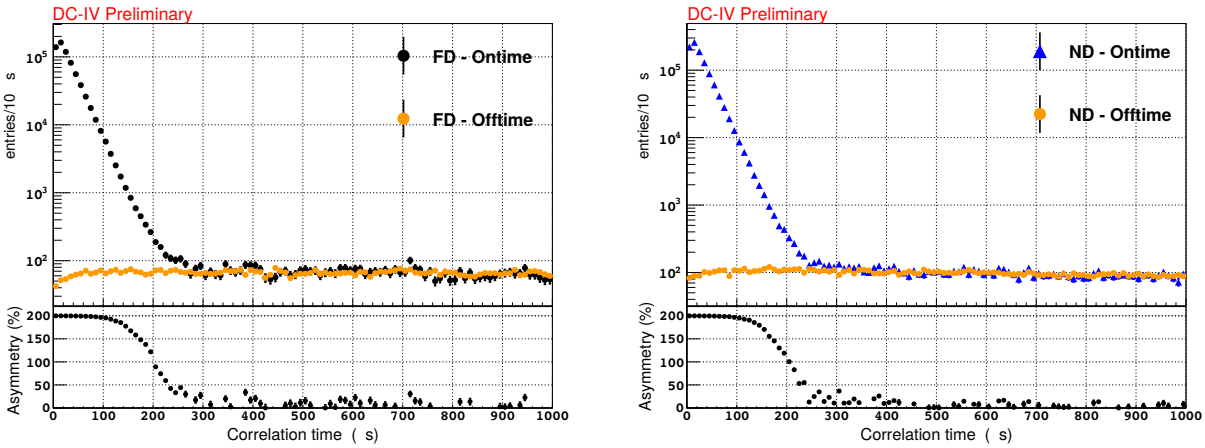

(b) Prompt-Delay correlation time.

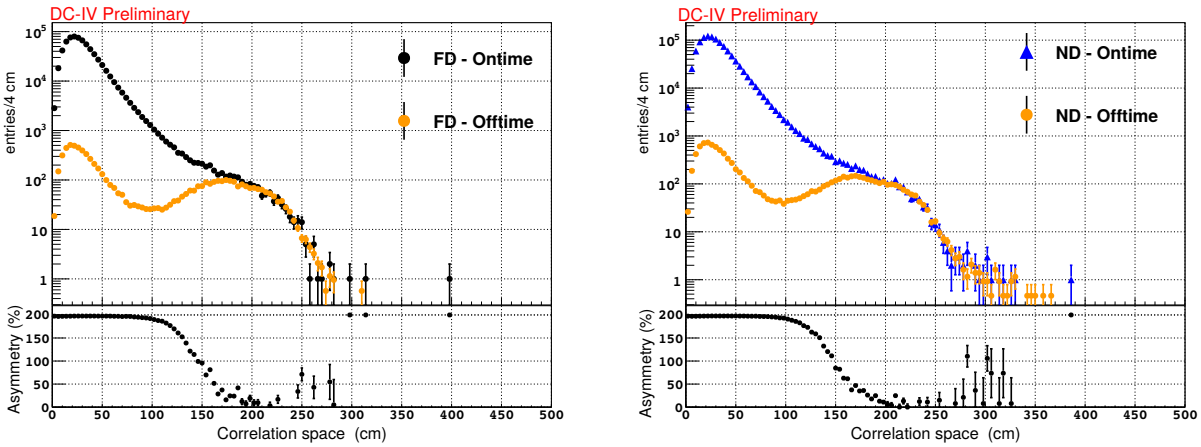

(c) Prompt-Delay correlation distance.

Figure 3.1.4: On-time and off-time spectra of the 5th ^{252}Cf calibration campaign at the detector center, (x, y, z) = (0,0,12)mm. *Left plots* correspond to FD and *right plots* to the ND. Asymmetry plots corresponds to $2 \cdot \frac{A-B}{A+B}$ where A (B) are On-time (Off-time) number of events. Prompt fission gammas spectra not shown because they are background free due to the lower energy cut.

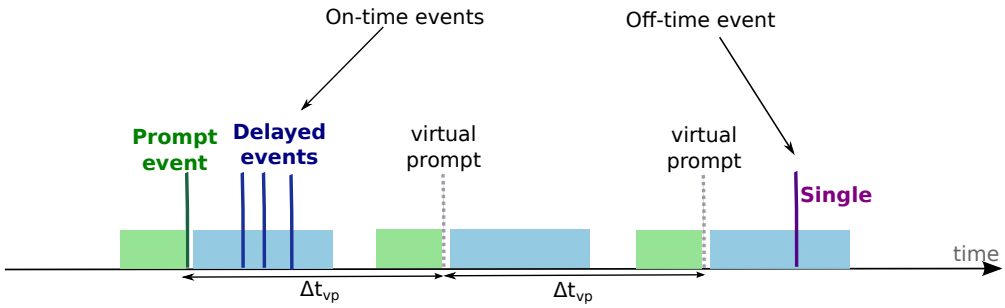

Figure 3.1.5: Representation of the *off-time window method* considering two off-time windows. The green and the blue boxes correspond to the prompt vetoes and delayed event selection respectively.

In order to compare off-time events (accidental background events) to the on-time ones (Cf candidates) a proper scaling factor must be applied. Together with the amount of off-time events per prompt event and the number of background windows used, it should be also considered a correction factor coming from the detector dead-time response. Every time a muon crosses the muon veto, there is a lapse of time where the taken data is vetoed and consequently no new triggers are generated as valid. This trigger loss can affect the off-time measurement. Real events might be lost and confused with single events, and therefore the background is underestimated. For that reason, besides the off-time events scaling factor a dead-time correction factor (CF) is added. In the case of the far detector 45.2 [42] muons per second are measured, corresponding to a $\mathrm{CF}_{\mu-\mathrm{veto}}(\mathrm{FD}) = 1.06 \pm 0.03$, and for the near detector around 239.7 [42] muons per second are observed being then $\mathrm{CF}_{\mu-\mathrm{veto}}(\mathrm{ND}) = 1.31 \pm 0.03$. These correction factors are estimated considering that at large correlation times both on-time and off-time distributions should be identical. In Fig. 3.1.4 the on-time and off-time spectra for both detectors considering the correction factors are shown. Besides, a representation of the background contribution is depicted in Fig. 3.1.6 for the delayed visible energy and correlation distances with orange distributions. It can be observed in Fig.3.1.4a and 3.1.6a that the off-time events contribute to the visible energy at low energies with single events, with a continuous spectra coming from fission prompt gammas mismatched, and neutron capture peaks from uncorrelated fission events. In the case of the prompt-delay correlation times (Fig.3.1.4b) the off-time events at large times $\Delta t > 250\mu$s behave as a flat distribution, being the main source of on-time events at large Δt (see asymmetry plot). Something similar happens in the prompt-delay correlation space distributions in Fig.3.1.4c and 3.1.6b. At large distances,

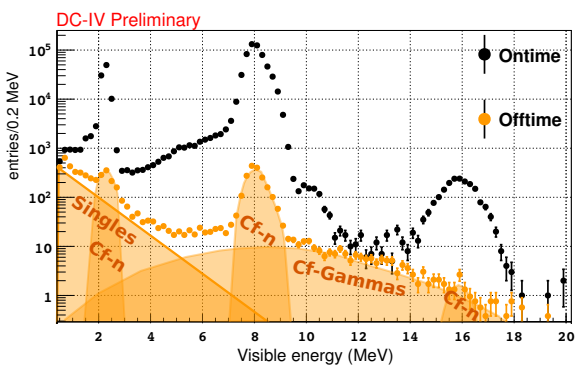

(a) Delayed visible energy.

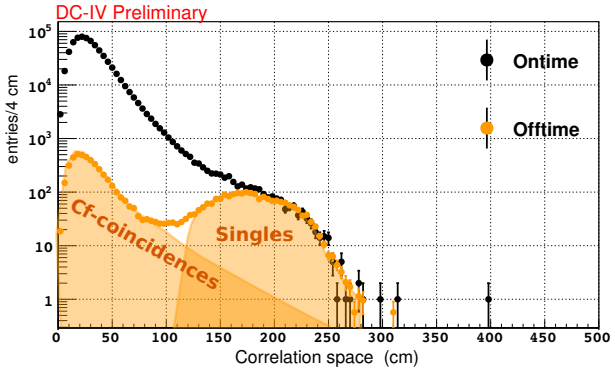

(b) Correlation distances.

Figure 3.1.6: On-time (black) and off-time (orange) spectra at the detector center, (x, y, z) = (0,0,12)mm. The orange shaded areas correspond to a schematic representation of each background contribution on the off-time spectra. Asymmetry plots corresponds to $2 \cdot \frac{A-B}{A+B}$ where A (B) are On-time (Off-time) number of events.

the on-time events are mainly single coincidences (see on the asymmetry plot that all of them are perfectly subtracted). While at short distances there is a contribution coming from Californium coincidences. Note that this background subtraction should also be applied in the simulated data: the source related background events which are uncorrelated in time are part of these off-time events and need to be also neglected in both data and MC files. In further sections, the ^{252}Cf selection spectra will be shown with an off-time event subtraction.

3.1.4 Spectra distributions

Subtracting the accidental background, the ^{252}Cf data and simulation spectra are an interesting and useful tool for the Double Chooz data analysis. The fission prompt spectra can be used for testing the energy scale, and the delayed energy spectra is the key of this thesis for the Double Chooz detection systematics studies.

Fission gammas: The neutrino oscillation analysis using the IBD method requires a precise knowledge of the energy scale due to the direct relation between the positron kinetic energy and the emitted reactor neutrinos. Typical gamma sources as e.g ^{60}Co only cover an energy range up to $\sim$ 3MeV. Where for a good energy scale calibration energy ranges 3-10 MeV are also needed (in order to cover the IBD method energy window). An interesting analysis using the ^{252}Cf data is to observe how the fission prompt spectra looks like for the energies between [0.5,20] MeV. These broad and continuous energy events plotted in Fig.3.1.7 are a powerful tool to test the goodness of the energy scale between detectors. Considering only the energy region where the IBD candidates can occur (energy range between [0.5, 10] MeV), a linear fit in the asymmetry plot in Fig. 3.1.7 can be done. The linear regression $f = m \cdot x + n$ (being x the visible energy, and f the asymmetry factor) can study the possible discrepancies between far and near detector data, considering the statistical fluctuations in the number of events. Taking into account only the data from

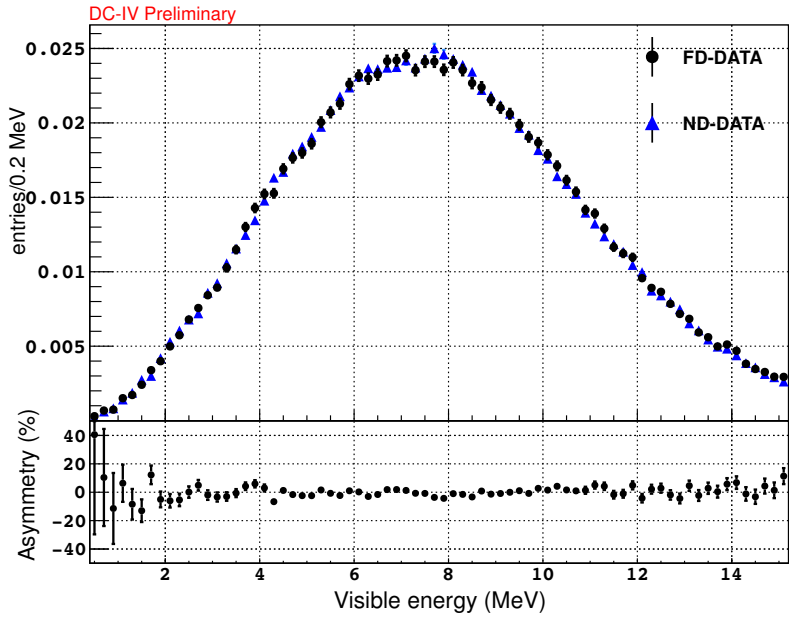

Figure 3.1.7: Fission prompt spectra for all visible energies after an accidental subtraction using the 5th calibration data at the target center (x, y, z) = (0,0,12)mm in both detectors. Plots normalized separately. Asymmetry plot corresponds to $2 \cdot \frac{A-B}{A+B}$ where A (B) is FD (ND) number of events.

the detector center, a slope m of $0.00 \pm 0.20\,\%$ and an intercept n $-0.62 \pm 1.18\,\%$ have been obtained [43]. This result proves that the far and near detector energy spectra are well matched, and any study comparing both detectors data in the ν-target should not be affected by the energy scale.

Neutron captures: The other relevant spectrum we can investigate using the ^{252}Cf source is the neutron capture energy. In Fig. 3.2.1 the delayed energy spectra obtained after a background subtraction for any data or MC simulation is represented. In this energy spectra the possible neutron captures in the ν-target are represented with different colors. Principally neutrons are captured on Gadolinium- and Hydrogen-nuclei, leaving energy capture peaks at around 8 MeV (green color) and 2.2 MeV (blue color) respectively. Each of these peaks is preceded by a Compton tail caused by capture gammas losing their energy. Also other compounds captures are observed. Some Carbon capture events at 5 MeV (red color) can be measure. And with lower probability, gammas from more than one capture at the same time can be measured. Captures of Gd- and H-nuclei can be observed in orange (with 10.2 MeV gammas). And two Gd-captures at the same time depositing 16 MeV gammas are represented with purple color.
The study of these peaks (Gd and H capture) along the ν-target center, and at the γ-catcher is the main topic of this thesis (developed in the Chapter 4 and 5). For that reason in Fig. 3.2.2 the delayed energy spectra for data and MC simulations are plotted at the target center. Nevertheless, it is important to point that looking into the data to MC comparison plots in Fig.3.2.2b and 3.2.2c is still possible to see an excess of data events for energies lower than $\sim 1.8\,\mathrm{MeV}$ (below the Hydrogen capture peak). These non-accidental events (otherwise they would have been subtracted with the off-time window method) are coming from a correlated background related to the ^{252}Cf source, already investigated in [44]. These events could be a source of systematic uncertainties in the future detection efficiency analyses (Section 3.2) due to efficiency energy dependence. For that reason future systematic studies developed in Chapters 4 and 5 are going to take into account this non-negligible events discrepancy considering different energy definitions and correlation times (Section 4.2).

3.2 Detection efficiency using the Cf source

For the estimation of expected neutrino events in our detector it is important to take into account the inverse beta decay detection efficiency. This detection efficiency can be divided in four terms (see Eq. (2.8)). Nevertheless, the dominant part of the detection uncertainty is the one coming from the IBD delayed event, the neutron detection. In order to completely evaluate this detection efficiency and its uncertainty, three different terms are studied:

$$\varepsilon_{\text{delay}} = \varepsilon_{\text{n-capture}} \times \varepsilon_{\text{cut}} \times \varepsilon_{\text{spill}} \tag{3.1}$$

where,

- $\varepsilon_{\text{n-capture}}$ estimates the fraction of neutron captures occurring in the liquid scintillator forming the detector target. Principally, it is called Gd-fraction ($\mathrm{f_{Gd}}$) because it studies the relative abundance of neutron captures on the Gd-nuclei in the ν-target.
- ε_{cut} evaluates the efficiency of the IBD selection cuts (energy, time and vertex).
- $\varepsilon_{\text{spill}}$ studies the border effects between the ν-target and the γ-catcher in the IBD selection due to neutron mobility.

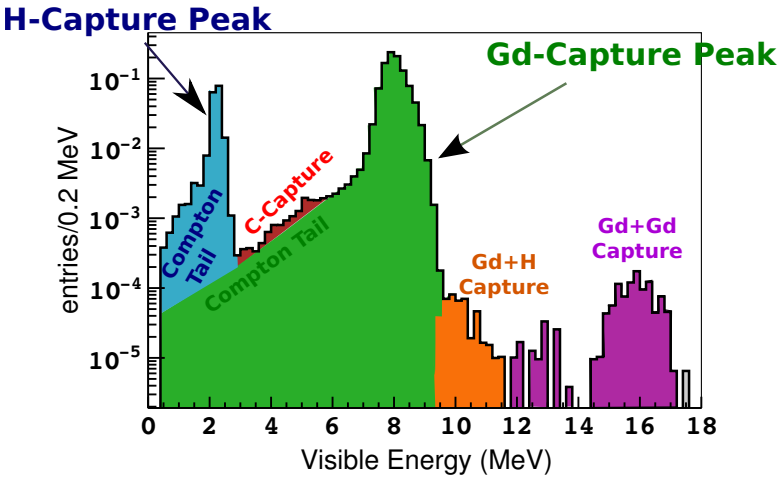

Figure 3.2.1: Delayed energy spectra for Californium data after a background subtraction. Coloured areas represent the observed energies for different captures in the liquid scintillator.

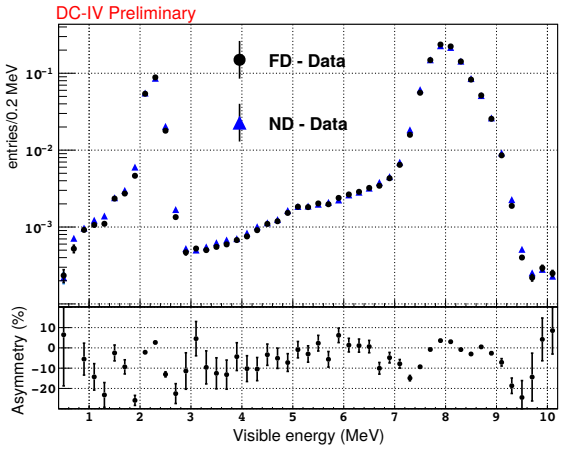

(a) Delayed visible energy for far and near detector data.

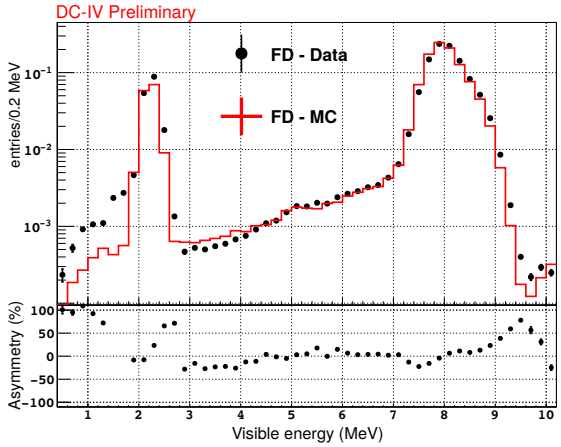

(b) Delayed visible energy for far detector data and MC.

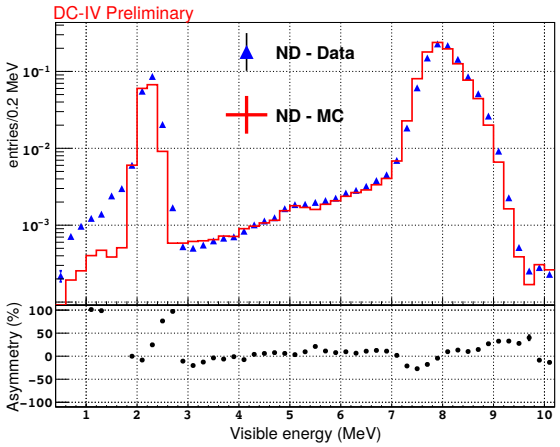

(c) Delayed visible energy for near detector data and MC.

Figure 3.2.2: Delayed energy spectra for far and near detectors data and MC simulations at the target center ((x, y, z) = (0,0,12)mm). Data is taken from the 5th calibration data. Asymmetry plots corresponds to $2 \cdot \frac{A-B}{A+B}$ where A, B are FD, ND or MC number of events depending on the plot.

These detection efficiency terms are studied using different neutron sources or simulations. First of all, for the $\varepsilon_{\text{n-capture}}$ the ^{252}Cf neutron events are used. In the Gd-analysis this term will be called f_{Gd}, analysing the Gd-capture events in the ν-target. Secondly, the ε_{cut} is studied using the IBD neutrons distributed in the entire detector. As a cross-check for this efficiency, Cf source neutrons as a point-like source can be used. Thirdly, the $\varepsilon_{\text{spill}}$ is not studied with natural sources. Simulations are implemented in order to evaluate this term. In the next two subsections the terms computed using the ^{252}Cf source will be defined: the fraction of neutron captures on Gd-nuclei f_{Gd} and the IBD selection cut dependent efficiency ε_{cut}.

Fraction of neutron captures on Gd-nuclei

The neutron capture is a competitive process between the different isotopes in the detector liquid scintillator. It depends on the neutron capture cross-section and the abundance of the isotopes present in the medium. In the ν-target, this competitive process is mainly taking place between the Gd and the H nuclei (more than a 99% of the neutrons are captured on them). The neutrons captured by Gd release gammas with energies around 8 MeV, where the H captures are at 2.2 MeV. Considering the energy spectra for data and simulations in Fig. 3.2.2, it is possible to see that the Gd-capture events are mainly distributed with energies between 3.5 and 10 MeV (Gd-capture peak and its tail). The H-captures are distributed with visible energies in the range [1.3, 3.5] MeV. Where the lower energy cut for the Hydrogen captures is considered in order to exclude the region with correlated background Fig.3.2.2b and 3.2.2c. For those reason and taking into account that any selection efficiency in general is defined as a ratio of events in two sub-samples,

$$\varepsilon_{\text{x}} = \frac{\text{n}_{\text{x}}}{\text{m}} = \frac{\text{N(selection with cuts x)}}{\text{N(opened selection cuts)}} \tag{3.2}$$

the fraction of neutron captures on Gd nuclei can be defined as

$$\text{f}_{\text{Gd}} = \frac{\text{N}(3.5 < \text{E}_{\text{delayed}} < 10\text{MeV})}{\text{N}(1.3 < \text{E}_{\text{delayed}} < 10\text{MeV})}\,. \tag{3.3}$$

With this definition the energy spectra is divided in events due to H- or Gd-captures (see Fig. 3.2.3). Then in the same way, it is possible to define the fraction of neutron captures by H-nuclei as:

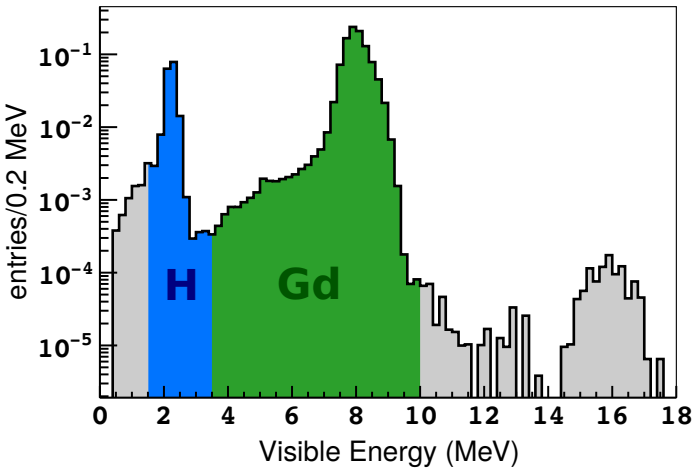

Figure 3.2.3: Gd-fraction definition considering the energy cuts from Eq. (3.3). Blue (green) area corresponds to the H-(Gd-)capture event ranges.

$$f_H = 1 - f_{Gd} = \frac{N(1.3 < E_{delayed} < 3.5MeV)}{N(1.3 < E_{delayed} < 10MeV)}. \tag{3.4}$$

It is important to point out that the small amount of carbon captures happening at 5 MeV are included in the Gd-captures region because these events are part of the IBD candidate selection in the Gd-channel analysis. Besides, the double captures due to Gd+H at $\sim$ 10.2 MeV and Gd+Gd at $\sim$ 16 MeV are neglected in this analysis.

IBD selection cuts dependent efficiency

This section studies the efficiency in the IBD selection. In the DC-IV Gd-channel the selection cuts are the ones given in Table 3.2.1, and considering the efficiency definition in Eq. (3.2) the simplest way to define it is:

$$\varepsilon_{semi} = \frac{N(4 < E_{delayed} < 10\,MeV \cap \Delta R < 1\,m \cap 0.5 < \Delta t < 150\,\mu s)}{N(3.5 < E_{delayed} < 10\,MeV)}, \tag{3.5}$$

where this definition accounts for all correlations between different cuts. It is called *semi-inclusive efficiency* because it includes all selection efficiencies at the same time, except for the Gd-fraction.

Table 3.2.1: Selection cuts for the IBD Gd-selection in the DC-IV analysis.

Cut variable	Selection
Delayed energy	$4 < E_{delayed} < 10\,MeV$
Correlation time	$0.5 < \Delta t < 150\,\mu s$
Correlation distance	$\Delta R < 1\,m$

Another possible way to compute this efficiency is considering all the selection cuts separately, being the ε_{cut} written as

$$\varepsilon_{exc} = \varepsilon_{E_{delayed}} \cdot \varepsilon_{\Delta t} \cdot \varepsilon_{\Delta R}, \tag{3.6}$$

where $\varepsilon_{E_{delayed}}$ is the delayed energy cut efficiency, $\varepsilon_{\Delta t}$ the correlation time cut efficiency, and $\varepsilon_{\Delta R}$ the correlation distance cut efficiency. This was the way to define the Gd- and H-analysis cut dependent efficiency in DC I and II analysis. For that reason it is defined as an *exclusive* efficiency $\varepsilon_{exc} = \Pi_i \varepsilon_i$. Each term in this efficiency is defined as:

$$\varepsilon_E = \frac{N(4 < E_{delayed} < 10\,MeV)}{N(3.5 < E_{delayed} < 10\,MeV)}, \tag{3.7}$$

$$\varepsilon_{\Delta t} = \frac{N(4 < E_{delayed} < 10\,MeV \cap \Delta R < 1\,m)}{N(4 < E_{delayed} < 10\,MeV)}, \text{ and} \tag{3.8}$$

$$\varepsilon_{\Delta R} = \frac{N(4 < E_{delayed} < 10\,MeV \cap \Delta R < 1\,m \cap 0.5 < \Delta t < 150\,\mu s)}{N(4 < E_{delayed} < 10\,MeV \cap \Delta R < 1\,m)}. \tag{3.9}$$

Nevertheless, even if the exclusive efficiency yields the same result as the semi-inclusive one, there could be discrepancies because the last one does not ensure no double counting in the uncertainty estimation. However, it has been used right now as a cross check for the cut efficiency.

Normalization correction factors

In order to do the θ_{13} fit, some parameters called correction factors are used. These terms relate the selected data in both detectors and the selected data to the MC simulated neutrino flux. Regarding the neutron detection efficiency, the correction factor is determined as

$$c(\mathrm{X:Y}) = \frac{\varepsilon^{\mathrm{X}}}{\varepsilon^{\mathrm{Y}}} \quad \text{and} \quad c(\mathrm{X:MC}) = \frac{\varepsilon^{\mathrm{X}}}{\varepsilon^{\mathrm{MC}}} \quad \text{where} \quad \mathrm{X,Y = FD,ND} \quad \mathrm{X \neq Y} \quad . \tag{3.10}$$

This correction factor is then the product of the cut dependent efficiency correction and the Gd-fraction correction $c = c_{\mathrm{cut}} \cdot c_{\mathrm{Gd}}$ for both data to data and data to MC simulation comparison.

Efficiency statistical uncertainty

Before finishing this chapter it is important to compute the statistical uncertainty of the efficiencies. In any efficiency estimation, two numbers are considered (from Eq. (3.2)): the selected events in a wide range m and the events passing the cut x ($\mathrm{n_x}$). These two numbers depend on each other, because $\mathrm{m} = \mathrm{n_x} + \mathrm{r}$ where r are the events not passing the cut x. Then the relation between the number of events on m and $\mathrm{n_x}$ is described by a binomial law [45]:

$$\mathrm{p}(\mathrm{n_x}|\varepsilon, \mathrm{m}) = \binom{\mathrm{m}}{\mathrm{n_x}} \varepsilon^{\mathrm{n_x}} (1-\varepsilon)^{\mathrm{m-n_x}}, \tag{3.11}$$

where p is the probability of having $\mathrm{n_x}$ events out of m tries, each with a probability of success ε. The important properties of this distribution are that the mean number of success is $< \mathrm{n_x} >= \mathrm{m} \cdot \varepsilon$ with a standard deviation $\sqrt{\mathrm{Var(n_x)}} = \sigma_{\mathrm{n_x}} = \sqrt{\mathrm{m}\varepsilon(1-\varepsilon)}$. From here it is possible to compute the uncertainty of ε as

$$\delta\varepsilon_{\mathrm{x}} = \frac{\delta < \mathrm{n_x} >}{\mathrm{m}} = \frac{\sqrt{\mathrm{m}\varepsilon(1-\varepsilon)}}{\mathrm{m}} = \sqrt{\frac{\varepsilon(1-\varepsilon)}{\mathrm{m}}} \quad . \tag{3.12}$$

Concluding that for any selection efficiency, it will be written $\varepsilon_{\mathrm{x}} \pm \delta\varepsilon_{\mathrm{x}}$ using Eq. (3.2) and (3.12).

Chapter 4

Neutron detection efficiency in the ν-target

Neutron detection efficiency terms has been studied along this chapter. The Gd-fraction f_{Gd} estimation in the ν-target liquid scintillator allows us to study the concentration of Gd atoms in it. Several studies have been performed testing the stability of this concentration in terms of time and considering the different deployment positions for the new era of data taking in the Double Chooz detectors. Besides, a detailed study of the systematic effect of this measurement has been developed, to estimate the neutron detection efficiency fit parameter and its uncertainty used in the DC-IV analysis. The semi-inclusive efficiency has been also tested using Cf-neutrons. And the obtained values has been used as a cross-check of the final parameter estimated using IBD neutrons.

4.1 Gd-fraction detection efficiency in the ν-target

Due to the homogeneously ad-mixed liquid scintillator, the Gd-fraction f_{Gd} should be uniform in the entire ν-target volume. Nevertheless, when an event happens close to the target borders, either neutrons or gammas can escape from the detector. As the Gd-fraction is strongly sensitive to the visible energy distributions (Gd-fraction is defined by energy intervals, see Section 3.2), the study of this parameter at the target centre allows to estimate the expected value for a homogeneous capture concentration without gamma-loss or neutrons moving close to the Gd-free γ-catcher. In this section, data and simulations are studied for a ^{252}Cf calibration source at the target center (x,y,z) = (0,0,12)mm. Considering the Gd-fraction definitions in Eq. (3.3), the delayed events with energies between 1.3 and 10 MeV are divided in two intervals attributed to H- and Gd-captures, respectively. Also to calibrate the IBD detection rate in the Gd-analysis, the correction factors c_{Gd} (data to data, and data to MC) defined in Eq. (3.10) are estimated. The obtained results from the

Table 4.1.1: Results for the Gd-fraction and correction factors at the ν-target center using the 5th Calibration Campaign data and simulations. Uncertainties are only statistical, where the correction factor ones are estimated via error propagation. For runs and deployment time information see Appendix A.

	Far Detector f_{Gd}	**Near Detector** f_{Gd}	c_{Gd} (FD:ND)
DATA	85.62 ± 0.04 %	85.41 ± 0.03 %	100.25 ± 0.06 %
MC	87.66 ± 0.04 %	87.61 ± 0.03 %	
c_{Gd} (DATA:MC)	97.67 ± 0.06 %	97.49 ± 0.05 %	

high statistics 5th Calibration Campaign (almost 45h of source deployment in the near detector and 24h in the far detector) are summarized in Table 4.1.1.

On the one hand, the Gd-fraction for both detector data is $\sim 85\%$ and for MC simulations around $\backsim 87\%$. This 2% discrepancy between data and MC simulation Gd-fractions was already observed in previous DC analyses. Besides several studies using IBD and spallation neutrons in DC-III analysis [44], several MC generators were used: Geant-4 and Tripoli4. In both of them a similar discrepancy was observed, a 2.08% for the Geant4-based MC simulation, and 2.36% with the alternative Tripoli4 [32]. A dependency on the neutron kinetic energy could consequently be excluded. This discrepancy is the main reason of computing a data to MC Gd-fraction correction factor. On the other hand, the data to data Gd-fraction correction factor presented a discrepancy of $(0.25 \pm 0.06\,(\text{stat}))\,\%$. No significant inconsistency is expected because the same scintillator liquids are used in both detectors and they have an almost identical geometry. Due to the long time exposure of the Cf source in the detector, the low statistical uncertainties could reveal this discrepancy. For that reason, systematic effects have been studied to test whether they could cause a discrepancy between detectors' Gd-fraction or not. In the Section 4.2 more information and analyses can be found about these systematics measurements. And in the next Chapter 5 an explanation is presented which might explain this discrepancy.

4.1.1 Time stability of the n-capture efficiency

Several calibration campaigns have been done in the Double Chooz detectors during their operation time. The Gd-fraction has always been evaluated along the five calibration campaigns (only two for the "younger" near detector). The comparison of these values is an important tool to test the time stability of the Gd concentration. In organic liquid scintillators doped with Gd-nuclei, the homosgenously distributed concentration of Gd-nuclei could be lost after some time. Gadolinium nuclei and complexes could plate out due to chemical reactions and solubility loss (e.g polymerazion). The best way to see if the concentration of Gd is constant in terms of time is studying the Gd-fraction at the detector centre and along the z-axis. The Gd-fraction results for the first and second campaigns were estimated during the DC-III analysis, and have been re-analysed for this study considering the DC-IV cuts. The third campaign is neither used in the DC-III nor DC-IV analyses. The light noise rate was higher during the period of time when it has been performed, and the trigger threshold was raised in comparison to the other calibration campaigns [32]. The fourth and fifth calibration campaigns are estimated in the DC-IV analysis, having data for both detectors. The Gd-fraction f_{Gd} results for all of these calibration campaigns are summarized in Table 4.1.2.

Table 4.1.2: Results for the Gd-fraction at the ν-target centre using the data from all the calibration campaigns in the Double Chooz operation time. Uncertainties are only statistical, and the runs and deployment time information for all of them can be found in Appendix A.

Calibration Campaign	**Far Detector** f_{Gd}	**Near Detector** f_{Gd}
1st	85.77 ± 0.11 %	–
2nd	85.49 ± 0.08 %	–
3rd	–	–
4th	85.53 ± 0.10 %	85.35 ± 0.12 %
5th	85.62 ± 0.04 %	85.41 ± 0.03 %

A first look on these numbers show us a good agreement between different campaigns Gd-nuclei neutron capture efficiencies. The highest discrepancy between the Gd-fractions is present between the 1st and the 2nd calibration campaigns' values, that are covered by the statistical uncertainties

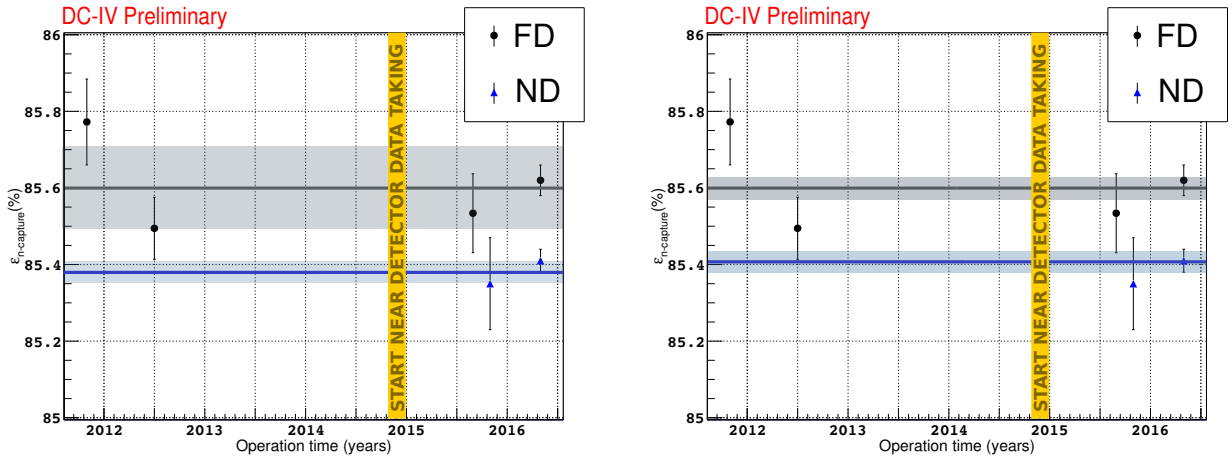

(a) **(b)**

Figure 4.1.1: Gd-nuclei neutron capture efficiencies for the different calibration campaigns in the Double Chooz detectors. Black circles correspond to far detector campaigns (since end of 2011) and blue triangles for the near detector (operating since December 2014). The gray/blue line corresponds to the **(a)** mean value **(b)** weighted mean value for the far/near detector.

(discrepancy of $(0.28 \pm 0.14)\,\%$). The Gd-fraction results in the first and the last calibration campaigns agree at $(0.15 \pm 0.12)\,\%$ and the discrepancy is fully covered by the statistical uncertainty. The presented near detector values are also perfectly in agreement, in this case with an almost negligible discrepancy of $(0.06 \pm 0.12)\,\%$.

These results are illustrated, in the Fig. 4.1.1 the Gd-fraction is plotted in terms of the detector operation time. Fig. 4.1.1a gray (blue) area represents the mean value $(85.60 \pm 0.10)\,\%$ for far detector ($(85.38 \pm 0.03)\,\%$ for near detector). All the Gd-fraction obtained values agree within its uncertainty for each detector separately. From these results it is possible to conclude that a time stability on the Gd-fraction is given. The far detector data is stable throughout time, considering its operation during almost five years. The near detector also presented a stable behaviour taking into account the two calibration campaigns in this detector.
For Fig. 4.1.1b, the weighted means are represented with a value of $(85.60 \pm 0.03)\,\%$ for the far detector and $(85.41 \pm 0.03)\,\%$ for the near one. These results are mostly weighted by the low statistical uncertainty in the fifth calibration campaign. A $\sim 0.2\,\%$ discrepancy between detectors Gd-fraction is observed. Next studies will focus to understand the origin of this discrepancy and if it is coverd by systematic uncertainties.

4.1.2 Z-axis symmetry on the n-capture efficiency

A homogeneously distributed liquid scintillator in the ν-target is expected in both detectors and consequently also an uniform n-capture efficiency. In order to test this, the different deployment positions along the Z-axis ν-target are tested using the Cf data. In this analysis, the fourth calibration campaign data has been used for the different positions presented in Table 4.1.3. These different heights have been analysed for data and also MC simulations. The ideal situation is that in all the positions, the Gd-fraction is constant along the Z-axis. However, border effects are expected for the top and the bottom part of the ν-target (close to the wall). The loss of Gd-capture events is caused by neutrons moving to the Gd-free γ-catcher, where these particles are captured

Table 4.1.3: 4th calibration campaign deployment positions and measurement time. This information is taken from the Appendix A.

(a) *Far Detector*

Position [mm]			Length [s]
x	y	z	
0	0	-1272	1 800
0	0	-960	3 600
0	0	0	13 200
0	0	+960	3 600

(b) *Near Detector*

Position [mm]			Length [s]
x	y	z	
0	0	-960	3 600
0	0	0	10 800
0	0	+960	3 600
0	0	+1160	3 600
0	0	+1210	3 600

on H-nuclei (reducing the Gd-fraction at the borders). Fig. 4.1.2a shows the Gd-fraction in both detectors for different z-axis positions. The values are presented with a stable f_{Gd} in the center region (from -1000 to 1000 mm). Then, close to the borders, the graph exhibits the expected decrease of Gd-captures.

This kind of plots are not only useful to test the Gd-fraction position stability, a relative crosscheck of the reconstructed positions can be also done. The correction factors obtained comparing the data and MC simulations are an useful tool to do it. In the Fig. 4.1.2b the correction factors between both detectors data and data to MC simulations are presented. First of all, the data to data correction factors allow us to see the already introduced $\sim 0.2\%$ discrepancy between detectors. It is not only observed in the ν-target center, but also in the other two points with lower statistics at approximately +960 and -960 mm. Secondly, the data to MC simulations fractions show again the expected $\sim 2\%$ discrepancy, and also a good agreement between detectors. There is a slight tension between the values at -960mm, where the c_{Gd}(DATA:MC) between detectors have a discrepancy of $0.7 \pm 0.35\,\%$. This discrepancy is covered within a two sigma statistical uncertainty. Any systematic shift in the deployment positions would have been observed in the other points. In any case all of them are covered by the grey area representing the average mean between detectors values and its uncertainty.

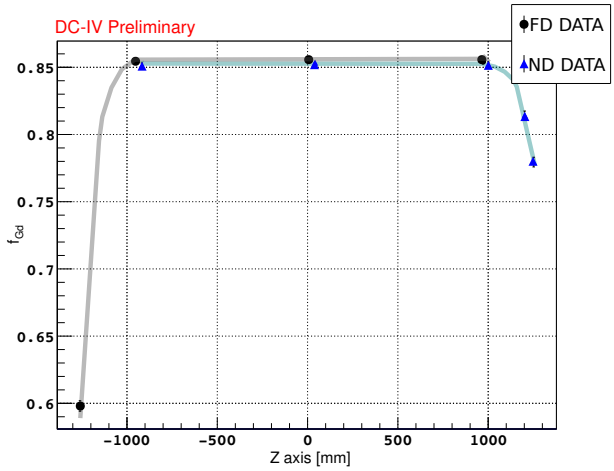

(a) Gd-fraction vs z-axis positions.

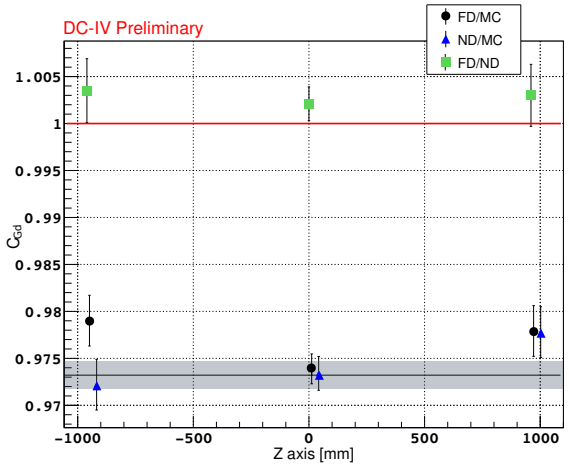

(b) Gd-fraction correction factors vs z-axis positions.

Figure 4.1.2: Gd-fraction values **(a)** and correction factors **(b)** as a function of the deployment position in the Z-axis. The positions are the ones from the Table 4.1.3 and only the statistical uncertainties are considered. The red line in the correction factor plot **(b)** corresponds to one, and the grey shaded area is the averaged mean between the two detectors centre values and its uncertainty.

The presented results along this section suggest that the Gd-fraction is stable and homogeneous in the entire ν-target volume. A little offset to one is observed in the ratio of Gd-fractions between the two detectors data in the last two calibration campaigns and along the z-axis positions. The difference could be indeed coming from a systematic effect in the measurement in one of the detectors. The next section will study the detection systematics in the Gd-fraction measurement.

4.2 Detection systematics in the Gd-fraction detection effiency

The efficiency correction factors defined in Eq. (3.10) need to be accurately estimated for the Double Chooz analysis. Any systematic bias in their measurement would affect the θ_{13} result. For the DC-IV Gd-analysis the last two calibration campaigns have been used. Two different approaches have been applied to better underestand the systematic effects. On one side, an energy cut variation study has been used. This inherited method from the DC-III Gd-analysis is applied to understand better the influence of the data to MC simulation discrepancies at low energies (already mentioned in Section 3.1.4). On the other side, a new Δt variation study has been considered in order to improve the understanding of the correlated background.

Systematics analysis 1: Energy variation studies

The measurement of the Gd-fraction given by the Formula 3.3 is directly linked to the energy definitions used to select the Gd- and the H-capture events,

$$f_{Gd} = \frac{N_{Gd}}{N_{Gd} + N_H} \text{ where } \begin{array}{l} N_{Gd} = N(3.5 < E_{visible} < 10\,MeV) \\ N_H = N(1.3 < E_{visible} < 3.5\,MeV) \end{array} \tag{4.1}$$

A modification on the energy regions used to select the captures will change the Gd-fraction result. The study of this variation can be used to estimate the systematic uncertainty. In the DC-III Gd-analysis this method was developed to compute the data to MC simulation Gd-fraction correction factor uncertainties. In the first phase of the DC-IV Gd-analysis this method is also applied to estimate the systematic uncertainties on the fourth calibration campaign data. The applied cuts are chosen in order to include possible systematic biases in the capture selection. Three different methods are applied in the DC-IV Gd-analysis, named from now on as Method A, B or C and are summarized in Table 4.2.1.

Table 4.2.1: Gd-fraction estimation criteria for the different methods applied for the detection systematics study.

	H events criteria	Gd events criteria	Comment
Method A	$0.5 < E_{visible} < 3.5\,MeV$ $1.3 < E_{visible} < 3.5\,MeV$ $1.5 < E_{visible} < 3.5\,MeV$	$3.5 < E_{visible} < 10\,MeV$	Vary energy threshold
Method B	$1.5 < E_{visible} < 3\,MeV$	$6.5 < E_{visible} < 9.5\,MeV$	No tails
Method C	$1.7 < E_{visible} < 3.5\,MeV$ for $\Delta t < 5\mu s$ $0.5 < E_{visible} < 3.5\,MeV$ for $\Delta t > 5\mu s$	$3.5 < E_{visible} < 10\,MeV$	No background

Method A: In this first method the H-capture peak minimum energy is varied in order to account for a changing fraction of events in the energy spectra where the data to MC differ (Fig. 3.2.2b and 3.2.2c). Three different minimum energies are considered: 0.5MeV, 1.3MeV and 1.5MeV. The first minimum cut was used to select the H events as done in the DC-III Gd-analysis. The second one was used in the DC-III H-analysis [46] and it is the one applied in this thesis. And the third

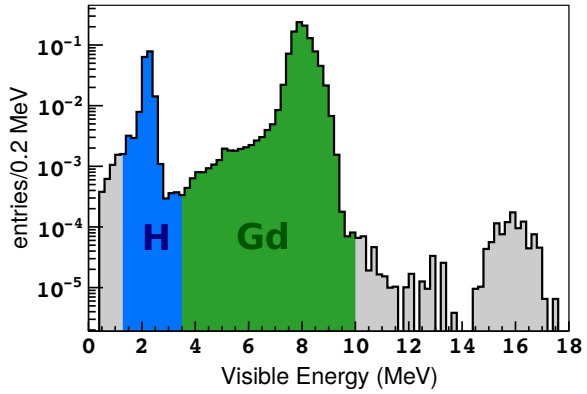

(a) Delayed energy spectra for *Method A-3*.

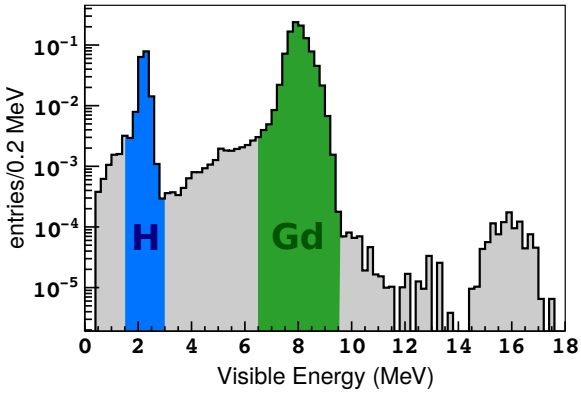

(b) Delayed energy spectra for *Method B*.

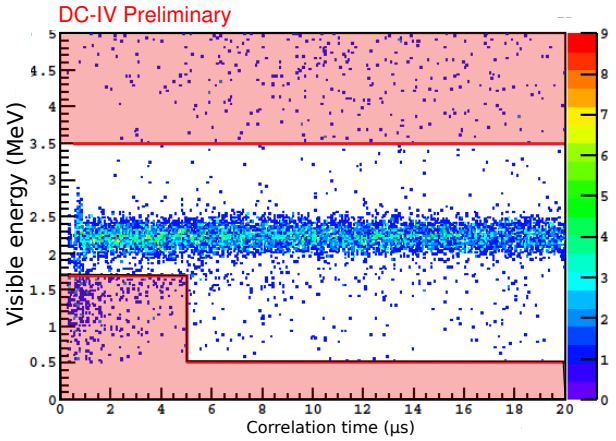

(c) Delayed energy spectra vs. correlation times for *Method C*.

Figure 4.2.1: Representation of the energy ranges used in **(a)** the Method A and **(b)** the Method B. The H-events are shown in the blue area, and the Gd-events with the green color. The rejected events are coloured in grey. **(c)** Two dimension plot of the delayed energy (y-axis) events and their correlation time (x-axis) for the far detector data only. The red lines are limiting the accepted events in the non-shaded area.

energy criteria is chosen in order to see if the selected events between 1.3 MeV and an energy closer to the peak (1.5MeV) are affecting the Gd-fraction correction factor. This third energy criteria is depicted in Fig. 4.2.1a, where the blue(green) events are the accepted H-(Gd-)capture events.

Method B:This method considers only the events in the Hydrogen and Gadolinium capture peak regions, neglecting peak-tails and the captures on Carbon. For H-capture events, the defined visible energy range is between [1.5, 3] MeV. And for the Gd-capture events, the energies are covering the range [6.5, 9.5] MeV. In Fig. 4.2.1b the considered regions in this study are represented in blue and green color respectively.

Method C: A third method is applied to remove most correlated background events. However, the obtained results from [44] are now considered. Some of the low energy events (with $E_{delayed} \lesssim 1.9\,MeV$) could be caused by a correlated background related to the Cf source, with a life time smaller than the real Cf events. A possible way to reduce this background is applying an energy-time cut. For that reason this method could be a bridge between using different energy cuts and a Δt study (as it is going to be considered in the next study). The used criteria are considered taking

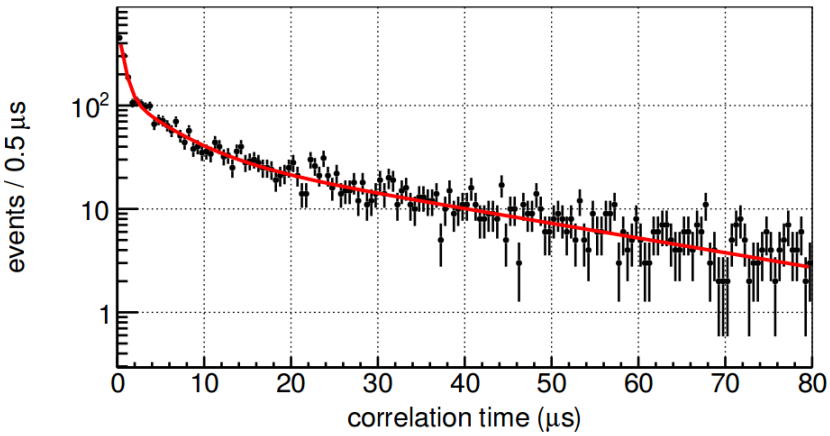

Figure 4.2.2: Correlation time distribution for $E_{delayed} < 1.9$MeV from [44]. The red line represents the fitted distribution following Eq. (4.2) with 4.3 as fitted parameters.

the information from the Fig. 4.2.1c. In this two dimension plot it is possible to see that for low correlation times a tighter energy range [1.7, 3.5] MeV is considered. For higher correlation times a loose energy cut of [0.5, 3.5] MeV. For the Gd-capture events no change in the energy criteria is applied.

Systematics analysis 2: $\Delta t_{\mathbf{min}}$ studies

Another way to study the systematic uncertainties is analysing the correlation time threshold. The idea of this analysis comes from a previous investigation developed in [44]. Low energy events correlation times were analysed to understand the data to MC discrepancy. In the Fig. 4.2.2 the correlation time spectrum for ^{252}Cf events with more than one delayed event with $E_{delayed} < 1.9$MeV is plotted. The red line corresponds to the fitted distribution following the equation

$$N(t) = \sum_{i=1}^{3} N_i \cdot e^{-t/\tau_i}. \tag{4.2}$$

If these events were produced by neutron captures on Hydrogen, an unique exponential distribution would be expected with a time constant of $\sim 30\mu$s. Nevertheless, three different time constants were obtained fitting the distribution. The decay time constants found are:

$$\begin{aligned} \tau_1 &= 30.6 \pm 2.8\,\mu\text{s} \\ \tau_2 &= 5.2 \pm 1.2\,\mu\text{s} \\ \tau_3 &= 625 \pm 85\,\text{ns}. \end{aligned} \tag{4.3}$$

The first decay time is the one consequence of the neutron captures in the target liquid. The events occurring with shorter mean correlation time (τ_2 and τ_3) might be due to a correlated background. As they satisfy the criteria of neutron multiplicities $m > 1$, these events are very likely radioactive/secondary decays of the ^{252}Cf fission fragments, not part of the MC simulation.

As these events happen at really short correlation times, we can study the impact of increasing the minimum correlation time Δt_{min} in the Gd-fraction correction factor using the delayed visible energy criteria for the DC-IV Gd-analysis of 1.3 MeV. As it was done previously, several tests taking into account different Δt_{min} are considered:

- ***Test 1:*** $\Delta t_{\text{min}} = 0\,\mu\text{s}$. This cut is applied in order to have the maximum range. In the DC-III Gd-analysis this was the used Δt_{min}.
- ***Test 2:*** $\Delta t_{\text{min}} = 0.5\,\mu\text{s}$. This minimum correlation time cut is applied in order to avoid possible detector dead-time effects. This is the one considered in this DC-IV Gd-analysis as baseline method.
- ***Test 3:*** $\Delta t_{\text{min}} = 2\,\mu\text{s}$. To possibly avoid the shortest component in the decay time ($625 \pm 85\,\text{ns}$), this test is applying as correlation time cut in order to include three times this decay time.
- ***Test 4:*** $\Delta t_{\text{min}} = 5\,\mu\text{s}$. An intermediate correlation time cut is considered.
- ***Test 5:*** $\Delta t_{\text{min}} = 15\,\mu\text{s}$. This last cut is avoiding the background with correlation decay time $5.2 \pm 1.2\,\mu\text{s}$, again considering as a correlation time cut at least three times this value.

In the DC-IV Gd-analysis a preliminary θ_{13} fit has been performed, where its results has been presented at [22] (value in Table 2.3.3). For this computation the second and the fourth calibration campaign data has been used for the Gd-fraction estimation. The fifth calibration campaign data is going to be used for the fit in the final DC-IV Gd-analysis. In this study the obtained results for the second and fourth calibration campaign systematic uncertainties are presented. Besides, a preliminary Gd-fraction proposal using the fifth calibration campaign data is going to be show for the future DC θ_{13} results.

4.2.1 Systematic uncertainties after the fourth calibration data

The Gd-fraction correction factor has been analysed for a preliminary DC-IV Gd-analysis using the second and fourth calibration campaigns' data. These two calibration data sets have been used in order to cover the Gd-fraction correction factor for the two far detector data sets (Section 2.3.3 - called FD-I and FD-II data) and the near detector data (not included before). The systematic uncertainties of the Gd-fraction corrector factor for these calibration data sets has been studied using an energy and a correlation time variation. The energy variation study has been inherited from the DC-III Gd-analysis. This contribution to the systematic covers the discrepancy at low energies in the data to MC delayed energy distributions. In the second and fourth calibration campaign this method was applied considering the Californium selection cuts from Section 3.1.2, but using the correlated time cut applied in the DC-III Gd-analysis $\Delta t_{min} = 0$ μs (inherited cut from the DC-III Gd-analysis). The obtained results using the Formula 3.3 and the cuts from Table 4.2.1 are summarized in Table 4.2.2. The statistical uncertainties are obtained using Eq. (3.12). The statistical uncertainties are related to the amount of events in the Hydrogen and Gadolinum energy regions, the variation of events in each Method is small. Consequenly, the statistical uncertainties between methods in the same detector-campaign sample are almost 100% correlated.

Table 4.2.2: Gd-fraction correction factor results using the fourth calibration campaign data for the different energy variation methods described in the Table 4.2.1.

Method	c_{Gd}(FD-II:ND)	c_{Gd}(FD-I:MC)	c_{Gd}(FD-II:MC)	c_{Gd}(ND:MC)
	1.0033 ± 0.0019	0.9718 ± 0.0015	0.9725 ± 0.0016	0.9696 ± 0.0018
Method A	**1.0026 ± 0.0019**	**0.9756 ± 0.0015**	**0.9748 ± 0.0016**	**0.9727 ± 0.0018**
	1.0024 ± 0.0019	0.9756 ± 0.0015	0.9759 ± 0.0016	0.9739 ± 0.0018
Method B	1.0023 ± 0.0019	0.9747 ± 0.0015	0.9746 ± 0.0017	0.9731 ± 0.0018
Method C	1.0034 ± 0.0019	0.9754 ± 0.0015	0.9754 ± 0.0016	0.9736 ± 0.0018

Comparing the data to MC correction factors of the far detector data sets (FD-I and FD-II), we find that both are in agreement with slight discrepancies which are covered by the statistical uncertainty. For the *Method A*, the data to MC ratio increases by raising the energy threshold. The behaviour is understood because by increasing the energy threshold, less low energy events are selected. Therefore, the selected H-area is considering less events in the discrepancy region in data and MC spectra, and the Gd-fractions get close between them (it is important to remember here that data and MC Gd-fractions differ in a $\sim 2\%$). The data to data ratios are expected to behave constant if the amount of low energy events are contributing in the same way in both detectors. Nevertheless, the data to data ratio slightly reduces by increasing the energy threshold. This result might indicate that the fraction of low energy events is not fully identical in both detectors. *Method B* was studying the Gd-fraction correction factor only selecting the events on the capture peaks. From the results in Table 4.2.2 a similar value as the one obtained with *Method A.2* (*Method A* with 1.3 MeV threshold) is observed. The results in the data to MC correction factor using *Method C* are close to the result for the Gd-fraction with an energy threshold of 1.3 MeV. But the data to data correction factors have the largest discrepancy between the *Method A.2* and the others, with a value of 0.08%.

In the correlation time variation study, different Δt cuts have been applied considering the Gd-fraction energy definition in Eq. (3.3). Considering the good agreement between the FD-I and -II results, the next study is going to consider only the fourth calibration campaign data. The obtained results for this value and the other correlation time cuts are summarized in Table 4.2.3.

For three of the different Δt_{min} cuts on FD-II and ND samples, the delayed energy spectra for data and MC simulations are illustrated in the Fig. 4.2.3. The expected behaviour is observed: increasing the minimum correlation time the discrepancy at low energies is reduced. For c_{Gd} (DATA:MC) the expected trend is that increasing the minimum correlation time cut, if the background is reduced c_{Gd} will decrease. The difference between the data and MC correlation time distributions at low Δt is the reason for this behaviour (Appendix B - Fig. B.0.1b). The neutron capture and elastic scattering are the main processes in the neutron interaction. One of them might not be properly implemented in the MC simulation. Consequently, the distributions do not present the same trend at low Δt (Fig. B.0.1b - black and blue distributions). Nonetheless, for the correction factors in Table 4.2.3 this reduction is not clearly observed in the data to MC simulation correction factors. the data to MC Gd-fraction fraction fluctuates by increasing the minimum correlation time cut, not showing a clear decrease. It could mean that an uncorrelated background is still affecting the correction factor measurement.

If the discrepancy between the detectors f_{Gd} comes from possible different contributions of correlated background events, the increase of Δt_{min} would bring the correction factor close to the unity. However, this value fluctuates and an offset remains even for the 15 µs cut. This observation concludes that the discrepancy between the detectors c_{Gd} is not coming from a possible short τcorrelated background in the source. At this level it is important to point out that the Δt_{min} cut

Table 4.2.3: Gd-fraction correction factor results for the different minimum correlation times using the data from the fourth calibration campaign of ^{252}Cf.

Δt_{min}	c_{Gd}(FD-II:ND)	c_{Gd}(FD-II:MC)	c_{Gd}(ND:MC)
0 µs	**1.0026 ± 0.0019**	**0.9748 ± 0.0016**	**0.9727 ± 0.0018**
0.5 µs	1.0022 ± 0.0018	0.9739 ± 0.0016	0.9723 ± 0.0018
2 µs	1.0024 ± 0.0019	0.9745 ± 0.0016	0.9728 ± 0.0018
5 µs	1.0030 ± 0.0019	0.9750 ± 0.0016	0.9718 ± 0.0017
15 µs	1.0028 ± 0.0021	0.9724 ± 0.0016	0.9707 ± 0.0020

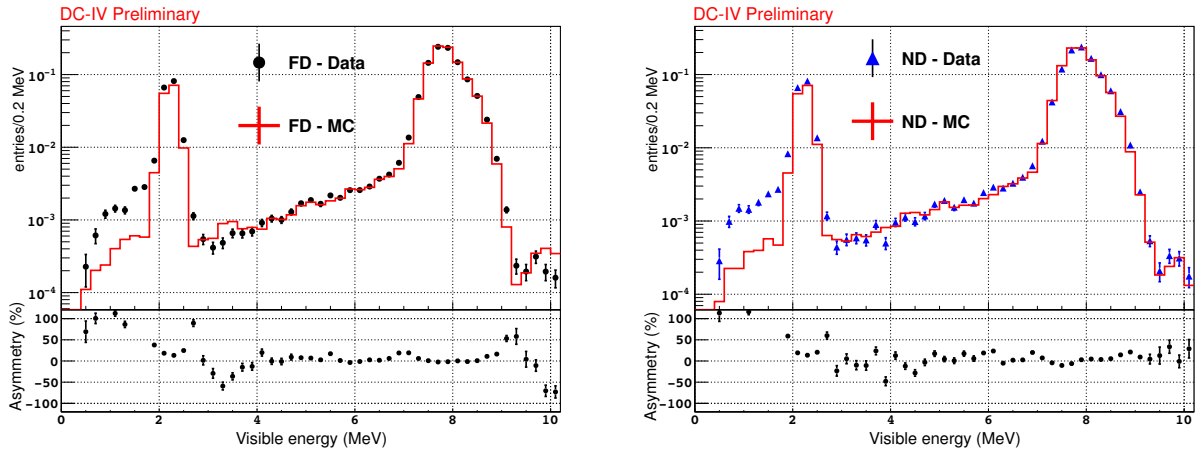

(a) Delayed energy spectra using $\Delta t_{\min} = 0\,\mu s$.

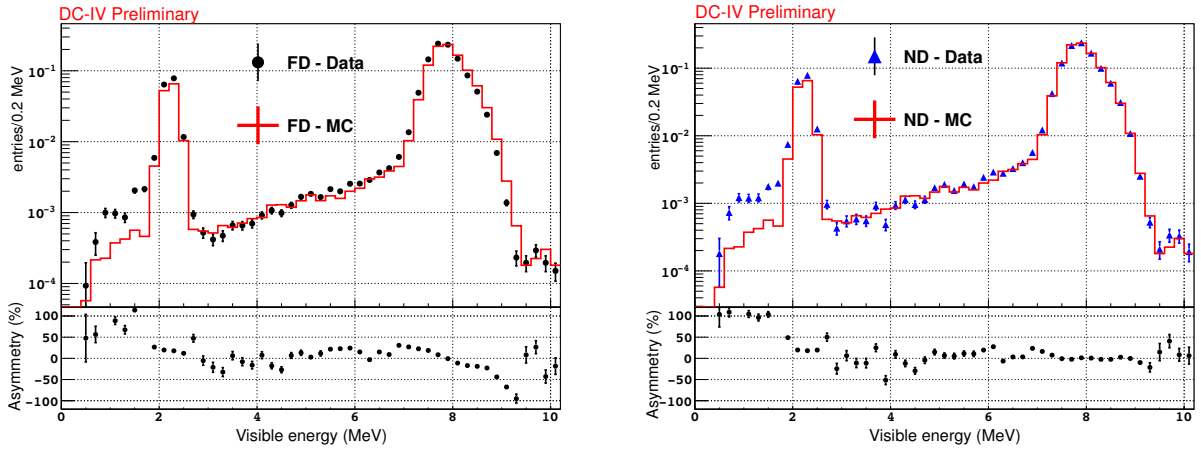

(b) Delayed energy spectra using $\Delta t_{\min} = 2\,\mu s$.

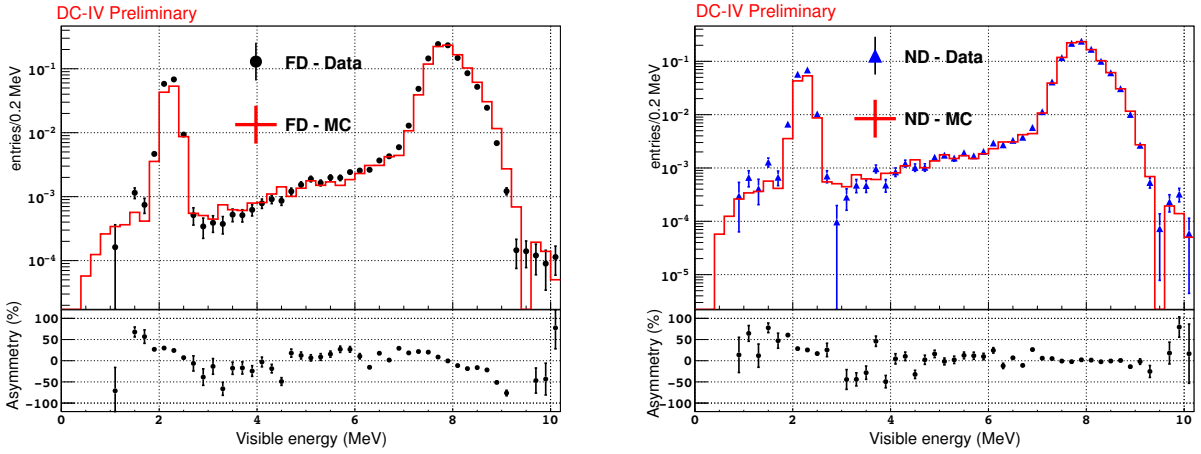

(c) Delayed energy spectra using $\Delta t_{\min} = 15\,\mu s$.

Figure 4.2.3: Data and simulation delayed energy spectra of the 4rd ^{252}Cf calibration campaign at the detector center, (x, y, z) = (0,0,12)mm, using different minimum correlation times $\Delta t_{\min}$. *Left plots* correspond to FD and *right plots* to the ND. Asymmetry plots corresponds to $2 \cdot \frac{A-B}{A+B}$ where A (B) are FD (MC) number of events. Plots scaled to the amount of events between the energy range of [7, 10] MeV.

with 0.5 µs is the one with the best agreement between detectors Gd-fraction. Considering also that this method is applied in order to avoid some detector response effects, the minimum correlation time used for the fifth calibration campaign is $\Delta t_{\min} = 0.5\,\mu s$.

Results: Considering the obtained results in Table 4.2.2 and 4.2.3, it is possible to estimate the systematic uncertainty correction factors used in the preliminary θ_{13} analysis. For the data to data correction factor, both methods (energy and correlation time variations) have presented some discrepancies between tests with the largest discrepancy of 0.08% (between energy variation *Method A* with energy threshold 1.3 MeV and *Method C*). This offset should be considered as the systematic uncertainty coming from the background events at low energies/correlation times. Then the data to data correction factor would be

$$c_{\mathrm{Gd}}(\mathrm{FD{:}ND}) = 1.0026 \pm 0.0019(\mathrm{stat}) \pm 0.0008(\mathrm{syst}) = 1.0026 \pm 0.0021(\mathrm{tot}). \tag{4.4}$$

This result is dominated by the statistical uncertainty, limited by the statistics in the fourth calibration campaign. And the systematic uncertainty covers the systematic effect of the method and the possible backgrounds.

Since data to MC correction factors agree within their uncertainties, a common value between detectors and calibration data sets is going to be considered for the final fit. And for that reason an averaged value is estimated comparing the data to MC results,

$$c_{\mathrm{Gd}}(\mathrm{DATA{:}MC}) = 0.9744 \begin{array}{ll} \pm 0.0015(\mathrm{stat}) & \text{FD-I} \\ \pm 0.0016(\mathrm{stat}) & \text{FD-II} \\ \pm 0.0018(\mathrm{stat}) & \text{ND} \end{array} \tag{4.5}$$

The statistical uncertainties are different for each detector because they are linked to the statistics in each measurement (the deployment time length). After applying an averaged value for both detectors, the systematic uncertainty should cover the far to near detectors discrepancy. For that reason the considered systematic uncertainty for these result is going to be the 0.21% difference between FD-II and ND correction factor results in bold in Table 4.2.2. Besides, it covers the discrepancies between energy and correlation variation results in Tables 4.2.2 and 4.2.3. Together with the statistical uncertainty

$$c_{\mathrm{Gd}}(\mathrm{DATA{:}MC}) = 0.9744 \begin{array}{lll} \pm 0.0015(\mathrm{stat}) \pm 0.0021(\mathrm{syst}) = \pm 0.0025(\mathrm{total}) & \text{FD-I} \\ \pm 0.0016(\mathrm{stat}) \pm 0.0021(\mathrm{syst}) = \pm 0.0026(\mathrm{total}) & \text{FD-II} \\ \pm 0.0018(\mathrm{stat}) \pm 0.0021(\mathrm{syst}) = \pm 0.0028(\mathrm{total}) & \text{ND} \end{array} \tag{4.6}$$

From results in the Eq. (4.4) and 4.6, it has been seen that final uncertainties are dominated by the systematics contributions. In the data to data correction factor the offset to unity is covered by the total uncertainty. However, this uncertianty is dominated by the statistical uncertainty. It is not possible to conclude the existence of a systematic bias with this low statistical precision. This was the main reason for taking the fifth calibration campaign in the Double Chooz detectors. High statistics samples (around 44h hours of data taking in the near detector and 25h for the far) were acquired at the target center for a detailed systematic study. This calibration campaign is the one analysed in the next subsection, and a preliminary proposal for the systematic uncertainty is going to be presented for the future θ_{13} estimation.

Table 4.2.4: Gd-fraction correction factor results using the fifth calibration campaign data for the different energy variation methods described in the Table 4.2.1.

Method	c_{Gd}(FD-II:ND)	c_{Gd}(FD-II:MC)	c_{Gd}(ND:MC)
	1.0031 ± 0.0006	0.9750 ± 0.0006	0.9723 ± 0.00005
Method A	**1.0025 ± 0.0006**	**0.9767 ± 0.0006**	**0.9748 ± 0.0005**
	1.0022 ± 0.0006	0.9773 ± 0.0006	0.9751 ± 0.0005
Method B	1.0023 ± 0.0006	0.9766 ± 0.0006	0.9744 ± 0.0005
Method C	1.0028 ± 0.0006	0.9772 ± 0.0006	0.9745 ± 0.0005

4.2.2 Systematic uncertainties for the fifth calibration data

With the high statistic samples obtained in the fifth calibration campaign, a new study on the systematic uncertainties for the correction factors obtained in Table 4.1.1 could be performed. The obtained results from this calibration campaign should be used for the final fit in the DC-IV analysis. A similar procedure to the one used in the fourth calibration campaign, is applied on these data. Energy and correlation time variation studies could be applied in order to test the low energy events and correlated background contributions. In Table 4.2.4 the obtained results for the energy variation study are presented. In this case, only the obtained results for the fifth calibration campaign are summarized. In the previous Section 4.2.1 FD-I and FD-II results were compatible between them (Table 4.2.2, FD-I:MC and FD-II:MC correction factors). Consequently, instead of using two correction two corrections (as considered in previous calibration campaign results), the obtained results for FD-II can be used for a final far detector estimation.

First of all, it is important to mention the small statistical uncertainties obtained using this campaign. This uncertainty reduction can help to understand better the discrepancies between the detectors. Secondly, fifth calibration campaign results present the same trend as in the fourth calibration campaign. The increase of the energy cut in *Method A* reduces the data to data correction factor, and brings the data to MC ratio closer to the expected 98% (mentioned in Section 4.1). Again the use of only capture peak energy regions in *Method B* does not affect the final correction factor: similar values for *Method B* and *Method A.2* are observed in data to data and data to MC correction factors. For the *Method C* correction factors, a similar value for data to MC correction factor to *Method A.2* is obtained. However, for the data to data correction factor it presents the relative largest discrepancy with a value of 0.03%.

Also the correlation time variation study has been applied in this campaign, and the obtained results are summarized in the Table 4.2.5. Again correction factor values present the same behaviour that in the four calibration campaign. The c_{Gd} (DATA:DATA) and c_{Gd} (DATA:MC) correlation factors fluctuate by increasing the minimum correlation time cut, not showing a clear increase for the data to data comparison or a decrease for the data to MC. An uncorrelated background could keep affecting the results.

Table 4.2.5: Gd-fraction correction factor results using fifth calibration campaign data for the different energy variation methods described in the Table 4.2.1.

Δt_{min}	c_{Gd}(FD:ND)	c_{Gd}(FD:MC)	c_{Gd}(ND:MC)
0 µs	1.0028 ± 0.0006	0.9776 ± 0.0006	0.9754 ± 0.0005
0.5 µs	**1.0025 ± 0.0006**	**0.9767 ± 0.0006**	**0.9748 ± 0.0005**
2 µs	1.0024 ± 0.0006	0.9773 ± 0.0006	0.9756 ± 0.0005
5 µs	1.0023 ± 0.0006	0.9771 ± 0.0006	0.9755 ± 0.0006
15 µs	1.0021 ± 0.0006	0.9733 ± 0.0006	0.9722 ± 0.0005

Results: Considering the previous results and discussions, a preliminary value for the correction factor systematic uncertainty using the fifth calibration campaign can be suggested. For the data to data correction factor systematic uncertainty, a similar procedure could be considered. The maximum discrepancy between correction factors using the energy variation method is 0.03%. This number comes from the discrepancy between the *Method A.2* and the *Method C*. Also in the correlation time variation method a discrepancy of 0.04% is observed between the correction factor using $\Delta t_{\text{min}} = 0.5\mu$s and the minimum time cut of 15 µs. These two discrepancies could be considered as a systematic uncertainty due to low energy and correlation time background events. Then a proposal for the the data to data correction factor systematic uncertainty would be ± 0.0003(syst-low E events) $\pm\, 0.0004$(syst-correlated bkg), being the correction factor written

$$c_{\text{Gd}}(\text{FD:ND}) = 1.0025 \pm 0.0006(\text{stat}) \pm 0.0005(\text{syst}) = 1.0025 \pm 0.0008(\text{tot}) \tag{4.7}$$

In the computed value for the fourth calibration campaign (Eq. (4.4)) the $\sim 0.2\%$ discrepancy of the data to data correction factor was covered by the total uncertainty. Nevertheless, with the new calibration campaign data this discrepancy is no longer covered. Considering these results, the $\sim 0.2\%$ discrepancy between the two detectors is significant and should be studied in detail in order to understand its nature.

For that reason, a proposal for the data to MC correction factor using the fifth calibration campaign is to consider two different data to MC correction factors,

$$\begin{array}{l} c_{\text{Gd}}(\text{FD:MC}) = 0.9767 \pm 0.0006(\text{stat}) \\ c_{\text{Gd}}(\text{ND:MC}) = 0.9748 \pm 0.0005(\text{stat}) \end{array} . \tag{4.8}$$

The systematic uncertainty for the data to MC correction factors could be also estimated (as for the fourth calibration data) from the difference between FD and ND correction factor results. This 0.24% discrepancy also covers the discrepancies between energy and correlation variation results in Tables 4.2.4 and 4.2.5. The suggested result for the data to MC correction factors would be

$$\begin{array}{l} c_{\text{Gd}}(\text{FD:MC}) = 0.9767 \pm 0.0006(\text{stat}) \pm 0.0024(\text{syst}) = 0.9767 \pm 0.0025(\text{total}) \\ c_{\text{Gd}}(\text{ND:MC}) = 0.9748 \pm 0.0005(\text{stat}) \pm 0.0024(\text{syst}) = 0.9748 \pm 0.0025(\text{total}) \end{array} . \tag{4.9}$$

The total uncertainties are estimated in order to be dominated by the systematic bias produced by the discrepancy between detectors. In that way, the proposed results for the fifth calibration campaign data to MC correction factor are in agreement between them considering the total uncertainty.

4.3 IBD cut dependent efficiency at the ν-target centre

In the neutron detection analysis a term analysing the IBD selection cut efficiency ε_{cut} (Eq. (3.1)) is also included. This neutron efficiency can be accurately estimated using the neutrons from IBD reactions of reactor antineutrinos (part of the neutrino signal), as they are homogeneously distributed in the entire detector volume. The Californium neutrons can also be used to estimate this parameter. But as Cf-neutrons can only provide a value for a specific deployment position, they are used as a cross-check of this neutron efficiency at the target center. The obtained results for the DC-IV analysis are retrieved by D. Navas (CIEMAT Madrid - Spain) about the semi-inclusive studies using IBD neutrons [48]. Along this section the obtained results are going to be summarized. Also, the values using Cf-neutrons are going to be presented as a cross-check for the final ε_{cut} fit value.

4.3.1 Semi-inclusive efficiency using IBD neutrons

IBD neutrons are selected following an extended selection similar to the used in the reactor signal (Section 2.3.2). IBD selection cut efficiency definitions are different for IBD and Cf neutrons, because signal neutrons should also include the candidate isolation cut and need to optimized in terms of signal to background ratio. The used semi-inclusive efficiency definition for IBD neutrons is

$$\varepsilon_{\text{semi}} = \frac{\text{N}(4 < \text{E}_{\text{delayed}} < 10\,\text{MeV} \cap \Delta R < 1\,\text{m} \cap 0.5 < \Delta t < 150\,\mu\text{s})}{\text{N}(3.5 < \text{E}_{\text{delayed}} < 10\,\text{MeV} \cap \Delta R < 1.7\,\text{m} \cap 0.25 < \Delta t < 200\,\mu\text{s})} \quad . \tag{4.10}$$

For the exclusive efficiency definition, $\varepsilon_{\text{exc}} = \varepsilon_{\text{E}_{\text{delayed}}} \cdot \varepsilon_{\Delta t} \cdot \varepsilon_{\Delta \text{R}}$ each term is defined as

$$\varepsilon_{\text{E}} = \frac{\text{N}(4 < \text{E}_{\text{delayed}} < 10\,\text{MeV} \cap \Delta\text{R} < 1\,\text{m} \cap 0.5 < \Delta\text{T} < 150\,\mu\text{s})}{\text{N}(3.5 < \text{E}_{\text{delayed}} < 10\,\text{MeV} \cap \Delta\text{R} < 1\,\text{m} \cap 0.5 < \Delta\text{T} < 150\,\mu\text{s})} \quad , \tag{4.11}$$

$$\varepsilon_{\Delta t} = \frac{\text{N}(4 < \text{E}_{\text{delayed}} < 10\,\text{MeV} \cap \Delta\text{R} < 1\,\text{m} \cap 0.5 < \Delta\text{T} < 150\,\mu\text{s})}{\text{N}(4 < \text{E}_{\text{delayed}} < 10\,\text{MeV} \cap \Delta\text{R} < 1\,\text{m} \cap 0.25 < \Delta\text{T} < 200\,\mu\text{s})} \quad , \tag{4.12}$$

$$\varepsilon_{\Delta R} = \frac{\text{N}(4 < \text{E}_{\text{delayed}} < 10\,\text{MeV} \cap \Delta\text{R} < 1\,\text{m} \cap 0.5 < \Delta\text{T} < 150\,\mu\text{s})}{\text{N}(4 < \text{E}_{\text{delayed}} < 10\,\text{MeV} \cap \Delta\text{R} < 1.7\,\text{m} \cap 0.5 < \Delta\text{T} < 150\,\mu\text{s})} \quad . \tag{4.13}$$

For more information about these efficiency definitions see [49]. As IBD neutrons are homogeneously distributed in the target volume, it is possible to estimate a volume-wide detection efficiency. The obtained results for the semi-inclusive and exclusive efficiencies correction factors for the first stage of the DC-IV analysis are summarized in Table 4.3.1.

Table 4.3.1: Selection cut efficiencies using 9 months of IBD data in the entire detector volume. Efficiency definitions and results are are from [48]. Uncertainties are considering the statistical fluctuation and the systematic method effect.

Efficiency	$c_{\text{cut-IBD}}$(FD-II:ND)	$c_{\text{cut-IBD}}$(FD-II:MC)	$c_{\text{cut-IBD}}$(ND:MC)
$\varepsilon_{\text{semi}}$	0.9985 ± 0.0028	0.9973 ± 0.0026	0.9986 ± 0.0009
ε_{exc}	0.9994 ± 0.0027	0.9979 ± 0.0021	0.9983 ± 0.0008
Δt	0.9987 ± 0.0014	0.9963 ± 0.0014	0.9976 ± 0.0005
E_{d}	0.9999 ± 0.0015	1.0007 ± 0.0015	1.0005 ± 0.0004
ΔR	1.0008 ± 0.0006	1.0009 ± 0.0013	1.0004 ± 0.0005

The uncertainties include statistical fluctuations and the systematic uncertainties, where these ones are estimated considering the fraction of events reconstructed in bottom half of the ν-target compared to the full target volume. All the efficiencies are in accordance with respect to the uncertainties. Exclusive efficiencies are in agreement with the semi-inclusive values for data to data and data to MC correction factors. FD-II to MC result is also in agreement with the obtained result for the DC-III analysis, $c_{\text{cut-IBD}}$(FD-I:MC) = 0.9996 ± 0.0021 (tot) [49]. The projected semi-inclusive efficiencies on the z-axis are given in Fig 4.3.1. Border effects on the ν-target can be observed by a semi-inclusive efficiency drop down.

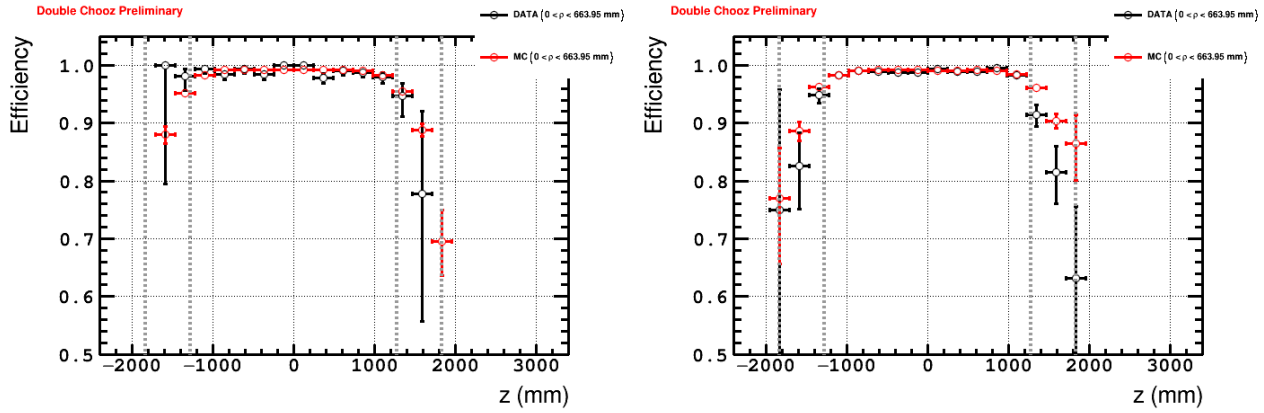

(a) Far detector Data and MC simulations

(b) Near detector Data and MC simulations

Figure 4.3.1: Data and simulation semi-inclusive efficiences map projection into z-axis position for $\rho < 663.95\,\text{mm}$ using 9 months of IBD data **(a)** to FD and **(b)** to ND. Dashed lines are the ν-target and γ-catcher walls [48]

.

4.3.2 Semi-inclusive efficiency using Cf-neutrons

The Californium neutrons are used to estimate a IBD selection cut for specific points of the detector. Its estimation at the target center can be used as a cross-check for the volume-wide efficiency results using IBD neutrons. A semi-inclusive efficiency has been estimated using Cf neutrons from the fourth calibration data, and it has been compared to the obtained result using IBD neutrons [48]. The obtained results for the cut efficiency correction factor using the Cf source at target center are summarized in Table 4.3.2. The IBD selection cut efficiencies are previously defined in Section 3.2 (Eq. (3.5) and 3.6).

The semi-inclusive efficiency correction factor for far and near detectors present a good agreement to the exclusive efficiency correction factor. The estimated values for far and near detector data to MC correction factors seem slightly higher than the obtained results for the DC-III analysis using Cf-neutrons, $c_{\text{cut-Cf}}(\text{FD-I:MC}) = 1.00034 \pm 0.00035\,(\text{stat})$ [47]. It seems that correlation space cut is not well optimize, and is causing this discrepancy. This parameter efficiency presents a statistically significant discrepancy to one (see Table 4.3.2 values) for data to MC correction factors. Where correlation time and energy correction factor efficiencies are in agreement. Consequently, the exclusive (and the semi-inclusive) efficiency show a higher correction factor. Even though, these correction factors are agreement between them and with one within two times their statistical uncertainty.

For those reason, they can be compared to the obtained results from IBD neutrons as they are an independent result (since they are obtained from independent analyses, different data samples and cover different volumes of the detector). In this case, both numbers are in agreement within their

Table 4.3.2: Selection cut efficiencies using Cf source data at the target center from the fourth calibration campaign. Efficiency definitions are in Eq 3.5 and 3.6. Uncertainties are only statistical, estimated using Eq. (3.12)

Efficiency	$c_{\text{cut-Cf}}(\text{FD-II:ND})$	$c_{\text{cut-Cf}}(\text{FD-II:MC})$	$c_{\text{cut-Cf}}(\text{ND:MC})$
$\varepsilon_{\text{semi}}$	1.0009 ± 0.0005	1.0014 ± 0.0004	1.0010 ± 0.0006
ε_{exc}	1.0009 ± 0.0005	1.0014 ± 0.0005	1.0009 ± 0.0005
Δt	1.0000 ± 0.0003	0.9994 ± 0.0003	0.9990 ± 0.0003
E_d	1.0000 ± 0.0002	1.0003 ± 0.0002	1.0001 ± 0.0002
ΔR	1.0008 ± 0.0003	1.0017 ± 0.0003	1.0018 ± 0.0004

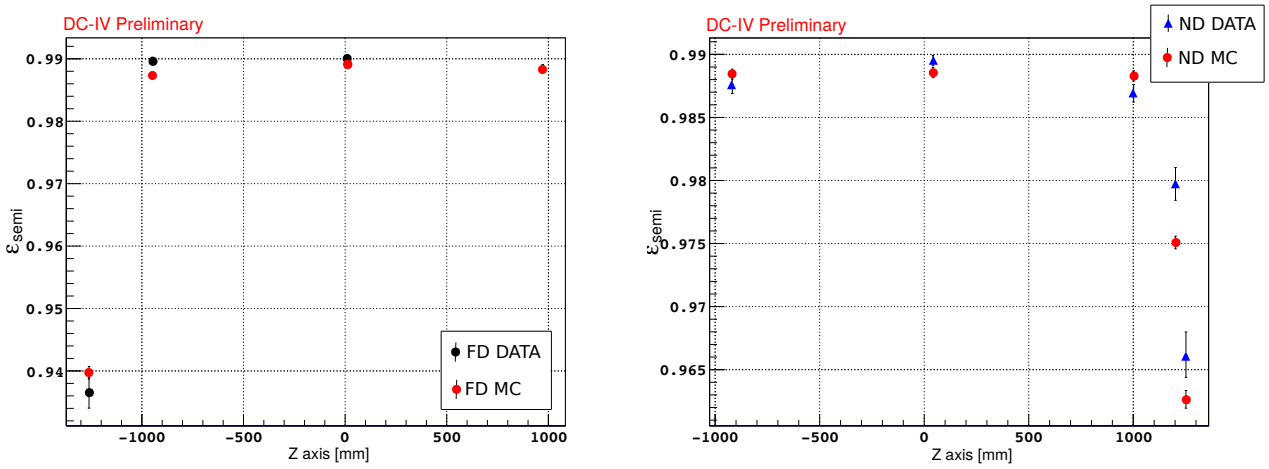

(a) Far detector data and MC simulations.

(b) Near detector data and MC simulations.

Figure 4.3.2: Semi-inclusive efficiencies for different deployment positions along the z-axis ν-target using Cf source data from the fourth calibration campaign. Uncertainties are only statistical.

uncertainties for the data to data correction factor. For data to MC values there is an accordance with the obtained results for FD-I in the DC-III Analysis. Note that the IBD values are estimated considering the entire volume, and considering the border effects close to the ν-target wall observed in Fig. 4.3.1. Therefore, the volume-wide efficiency using IBD neutrons is going to be different to the measured value at the ν-target center. For that reason, the values for the semi-inclusive efficiency in the different deployment positions of the Cf source are presented for the fourth calibration data and MC simulations in Fig. 4.3.2. Comparing these plots to the semi-inclusive projection maps in Fig. 4.3.1 using IBD neutrons, a good agreement between their values is observed. The same trend for the semi-inclusive efficiency in terms of the Z-axis position is presented. A similar plot

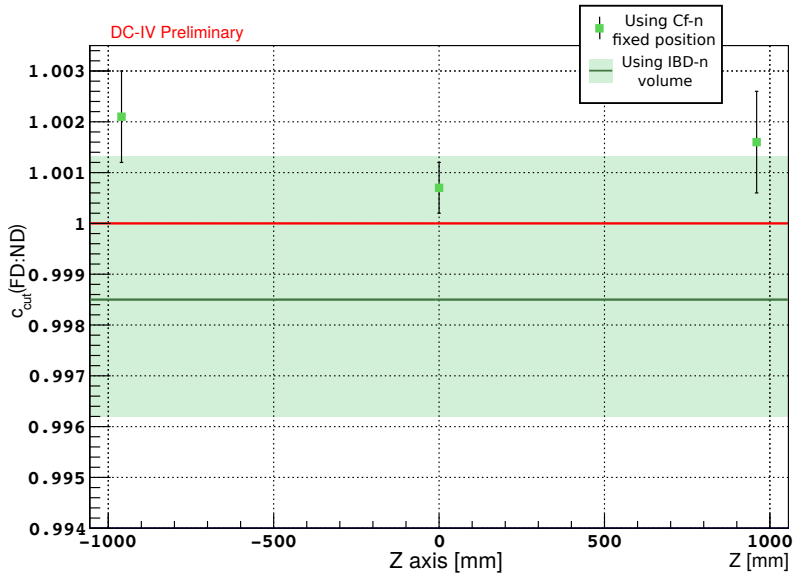

Figure 4.3.3: Semi-inclusive efficiency correction factors for detectors data using different Cf deployment positions (green squares, only statistical uncertainties are considered) and the volume-wide efficiency using IBD neutrons (value from Table 4.3.1).

showing the data to data semi-inclusive correction factor is given in Fig. 4.3.3 for three deployment positions. Also the volume-wide efficiency value from Table 4.4.2 is included. Both, the Cf and the IBD results present a semi-inclusive efficiency correction consistent between methods.

4.4 Conclusion

Along this chapter the neutron detection efficiency has been evaluated for the DC-IV analysis using Cf neutrons. Initially the Gd-fraction efficiency has been analysed in the ν-target in order to understand the neutron detection efficiency in the Double Chooz detectors. The covered topics could be divided in three parts.

First of all, the measurement of the Gd-fraction at the ν-target center has been estimated using the fifth calibration campaign data. A clear discrepancy between detector values has been observed. The far to near detector Gd-fraction presented a discrepancy to unity of $(0.20 \pm 0.06)\%$. Several reasons could explain this discrepancy. A wrongly subtracted background in one of the detectors may explain it. Also, systematic effects in the measurement could affect the Gd-fraction estimation. For that reason, a detailed study on the systematic uncertainties has been done and it is summarized below. Also from these results using the fifth calibration campaign, the data to MC fractions presented the already observed $\sim 2\%$ discrepancy in the DC-III Gd-analysis. The nature of this value has always been coming from the imperfect neutron simulation at low kinetic energies.

Secondly, to test the Gd-fraction a study about its stability has been developed. Several calibration campaigns have been used to estimate the Gd-fraction. All the values are in agreement considering only the statistical uncertainty, proving the constant value of the time stability of this parameter. Also, the discrepancy between detectors Gd-fraction considering the fourth and fifth calibration campaign data has been observed.
Besides, calibration data along the symmetry z-axis in the detectors has been used to prove the spatial stability of this efficiency. The fourth calibration campaign data provided several points along the axis. Their Gd-fractions show the already mentioned good agreement between the center and ±960mm values. Furthermore, the previously mentioned discrepancies between data to data values and data to MC fractions are clearly observed not only for the centre value. These results show no hint for a possible position offset in the source deployment.

Finally, a discussion about the systematic uncertainties in the measurement of the Gd-fraction at the ν-target centre has been included. Two different studies have been applied to disentangle possible background events. Variation methods studying low energy (below the H-capture peak) and short correlation times. Both studies have been applied in the fourth calibration campaign, obtaining the systematic uncertainties for the Gd-fraction correction factors in Table 4.4.1. Final uncertainties for the data to data correction factor are estimated considering statistical uncertain-

Table 4.4.1: Gd-fraction correction factor results for the fourth and fifth calibration campaigns. The uncertainties cover the total uncertainty in the measurement: statistical and systematic.

$c_{\text{cut}}(\text{f}_{\text{Gd}})$	4th Calib. Camp.	5th Calib. Camp.
FD-II:ND	**1.0026 ± 0.0021** (± 0.0019 (stat) ± 0.0008 (syst))	1.0025 ± 0.0008 (stat+syst)
FD-I:MC	**0.9744 ± 0.0025** (± 0.0015 (stat) ± 0.0021 (syst))	0.9967 ± 0.0025 (stat+syst)
FD-II:MC	**0.9744 ± 0.0026** (± 0.0016 (stat) ± 0.0021 (syst))	0.9967 ± 0.0025 (stat+syst)
ND:MC	**0.9744 ± 0.0028** (± 0.0018 (stat) ± 0.0021 (syst))	0.9748 ± 0.0025 (stat+syst)

Table 4.4.2: Obtained numbers for the semi-inclusive efficiency correction factors using Cf-neutrons at the target center (DC-III [47] and DC-IV Table 4.3.2) and IBD-neutrons in the entire volume (DC-III and IV results and definitons from [48]).

$c_{\mathrm{cut}}(\varepsilon_{\mathrm{semi}})$	Cf-n Centre	IBD-neutrons Volume
FD-II:ND	1.0009 ± 0.0005 (stat)	**0.9985 ± 0.0028** (± 0.0017 (stat) ± 0.0022 (syst))
FD-I:MC	1.0034 ± 0.0035 (stat)	**0.9996 ± 0.0021** (± 0.0010 (stat) ± 0.0019 (syst))
FD-II:MC	1.0014 ± 0.0004 (stat)	**0.9973 ± 0.0026** (± 0.0016 (stat) ± 0.0021 (syst))
ND:MC	1.0010 ± 0.0005 (stat)	**0.9986 ± 0.0009** (± 0.0007 (stat) ± 0.0005 (syst))

ties and a systematic contribution from low energy events. The systematic effect due to correlated background is covered by this uncertainty. The data to MC correction factors have been considered equal between FD-I, FD-II and ND data sets. The systematic uncertainties have been estimated considering the discrepancy between the detectors. Due to further analyses the low energies events and correlated backgrounds are better understood. Consequently, uncertainties in using the fourth calibration campaign are lower than the ones from the DC-III analysis. The obtained results from the fourth calibration campaign have been used as input parameters for a preliminary result in the DC-IV analysis (value in Table 2.3.3, for fits in Fig. 2.3.1) [22].

The fifth calibration campaign data has been also studied along this chapter. A preliminary value for the systematic uncertainty has been proposed for the final DC-IV analysis. The suggested values are also summarized in Table 4.4.1. A similar procedure in the systematic study has been performed. Due to the low statistical uncertainty in this campaign, the discrepancy between detectors has become significant. For that reason, a different value in the data to MC correction factor in the fifth calibration campaign has been chosen.

For a final neutron detection efficiency, semi-inclusive efficiencies are also studied along this chapter. This IBD selection cut efficiency is better estimated using IBD neutrons because they are homogenously distributed in the entire ν-target volume. In the first stage of the DC-IV analysis the semi-inclusive correction factors using this neutron source are summarized in Table 4.4.2. Californium neutrons have also been used to cross-check these values. These two independent methods can be compared due to their non-correlation. The fourth calibration campaign data has been used to evaluate the semi-inclusive efficiency at the target center. The obtained values are also summarized in Table 4.4.2. Besides, an estimation of the semi-inclusive efficiency using the different deployment positions along the z-axis has been performed. A general accordance of the ^{252}Cf and IBD results is given in the total c_{cut} estimation and along the z-axis projections.

Along this chapter the preliminary DC-IV Gd-analysis results for the c_{Gd} and c_{cut} has been presented (bold numbers in Tables 4.4.1 and 4.4.2). A new estimation of the θ_{13} value has been performed using them (result in Table 2.3.3 ,presented in [22]). Gd-fraction studies have presented a discrepancy between detectors efficiencies. Different measurements, including the final result from the high statistics calibration campaign, has shown that the data to data ratio of the Gd-fraction is not unity. And its discrepancy to one (and its uncertainty) should be well measured in order to have a realistic fit input for future analyses.
In the next chapter an analysis covering the γ-catcher detector volume is going to be developed in order to study this non Gd-loaded scintillator. A H-fraction estimation in this volume is needed for a H-analysis using the Double Chooz detectors. However, a discrepancy between detectors in this volume has been also measured. The study of this discrepancy could help to understand the detectors discrepancy pointed out in this chapter.

Chapter 5

Neutron detection efficiency in the γ-catcher

The Double Chooz detector analysis using the H-channel requires the estimation of the neutron detection efficiency over the entire fiducial volume: the ν-target and γ-catcher volumes. For that reason the study of the H-captures in the non Gd-loaded liquid scintillator using the deployment of ^{252}Cf along the Guide Tube (Section 2.1.2, Fig. 2.1.2b) is necessary. Along this chapter the new far and near detector data from the fourth and fifth calibration campaigns in the γ-catcher are analysed. The first results comparing both detectors' data are presented in the first part of this chapter, showing a non-expected behaviour in the near detector γ-catcher. Several studies are developed afterwards in order to understand the nature of this disagreement between the detectors.

5.1 Neutron capture detection efficiency in the γ-catcher data

A neutron detection efficiency analysis for H-captures applies a similar procedure than the Gd-analysis. However, the fiducial volume is now covering both ν-target and γ-catcher volumes. The study of the neutron detection efficiency in the γ-catcher volume is necessary. The measured variable in a H-analysis is the Hydrogen fraction (f_H). As it was already introduced in Eq. (3.4), H- and Gd-fractions are related by the formula:

$$f_H = 1 - f_{Gd} = \frac{N_H}{N_{Gd} + N_H} \quad \text{where} \quad \begin{array}{l} N_{Gd} = N(3.5 < E_{visible} < 10\,\text{MeV}) \\ N_H = N(1.3 < E_{visible} < 3.5\,\text{MeV}) \end{array} . \tag{5.1}$$

In a previous Double Chooz analysis (the DC-III analysis), this value was estimated for the far detector. The first and second calibration campaign data were used for that. During these calibration campaigns, the ^{252}Cf source was deployed in several positions along the Guide Tube. The study of the H-captures along different positions is an important key for a H-analysis. The use of several points helps to understand the inhomogeneity of the Hydrogen capture efficiency due to the measurement of some captures on C- and Gd-nuclei (energy events between 3.5 and 10 MeV). The last ones are caused by neutron mobility, and this effect was already introduced as spill-in (Section 3.2). It occurs when for a IBD-event happening in the γ-catcher, the neutron is captured on a Gd-nuclei in the ν-target. The opposite effect (spill-out) was already observed in the study of the Gd-fraction along the z-axis in Fig. 4.1.2a. In general all the deployment positions in the γ-catcher can observe this effect. But the positions close to the ν-target wall are the most sensitive ones. In the previous DC analyses using the first and second calibration campaigns this neutron mobility effect was measured. In the Fig. 5.1.1 some deployment positions from the first and the

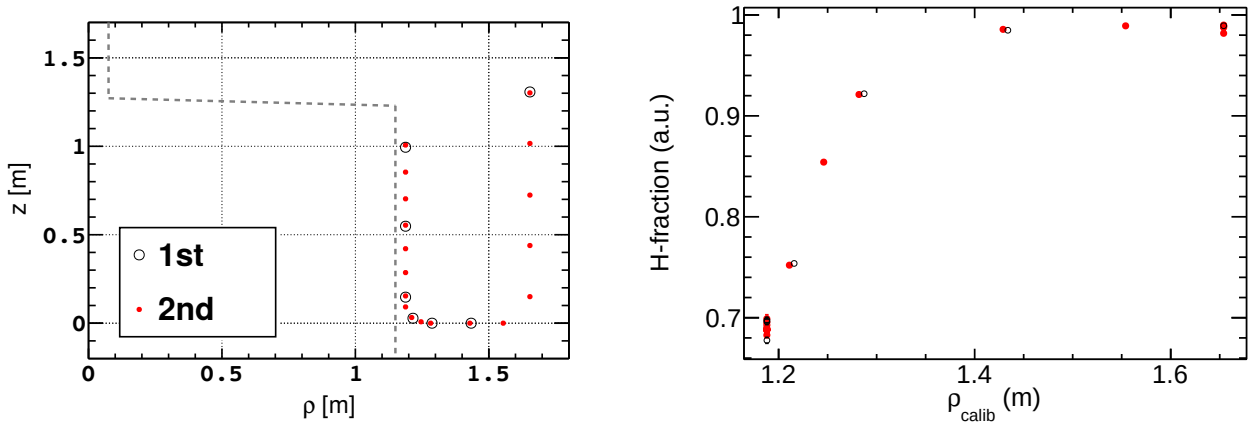

(a) Source position. **(b)** H-fraction vs ρ-axis position.

Figure 5.1.1: **(a)** Source position values in terms of (ρ, z) and **(b)** H-fraction in terms of the ρ-axis position using the first and second calibration campaigns far detector data. The H-fraction definition is the same one used in Eq. (3.4). Plots obtained from [50].

second calibration campaigns are plotted with their Hydrogen fraction value. In Fig. 5.1.1b for deployment positions close to the ν-target wall ($\rho_{\text{calib}} < 1.4\,\text{m}$) the fraction of captures on H-nuclei is reduced (and consequently, increased on Gd-nuclei). In contrast, the values obtained for the furthest positions to the wall ($\rho_{\text{calib}} > 1.4\,\text{m}$) the H-fraction is stable and close to ~ 1. With these results the importance to test different Guide Tube deployment positions is confirmed. The obtained results for the H-fraction using the fourth calibration data in different deployment positions for both detectors are presented in the next subsection.

5.1.1 Spectra distributions and H-capture efficiency for different positions

The fourth calibration campaign recollected data along the Guide Tube for both Double Chooz detectors. Depending on the deployment position a different value of the H-fraction is obtained. For that reason, some strategic positions along the Guide Tube data are going to be analysed. In Fig. 5.1.2 fourth calibration campaign data positions are represented. The used ones in this analysis are highlighted; in each of them different results are expected:

- ***Position 1*:** The source is placed at $\sim (\rho, z) = (145, 1535)\,\text{mm}$. Due to its proximity to the detector chimney (volume filled with Gd-loaded scintillator) some spill-in effect is expected.
- ***Position 2 and 3*:** These two positions are the furthest ones to the ν-target wall (with $\sim (\rho, z) = (1535, 1516)\,\text{mm}$ and $\sim (\rho, z) = (1653, 1427)\,\text{mm}$ respectively). Almost no spill effect should be observed: all the neutrons will be expected to be captured on H-nuclei (f_H almost 1).
- ***Position 4*:** One of the z=0 deployment positions, $\sim (\rho, z) = (1437, 0)\,\text{mm}$, where the source is deployed at the centre of the γ-catcher. As the source will be closer to the ν-target wall than in the Pos. 2 and 3, some spill effect will be expected with a H-fraction slightly lower than in the previous case.

The obtained H-capture fractions for each of these deployment positions in both detectors are summarized in Table 5.1.1. Far detector results are in agreement with the obtained results in previous calibration campaigns (see [50]). The expected spill effects in each position are measured.

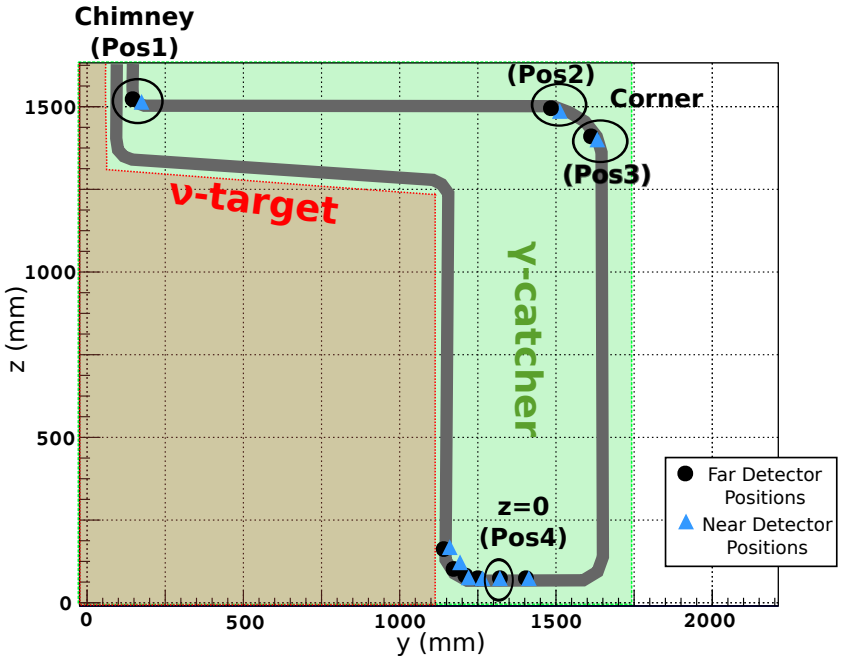

Figure 5.1.2: Detector representation along the positive (y, z) axis. Red area represents the Gd-loaded liquid scintillator volume (ν-target). Green volume limits the γ-catcher volume, Gd-free liquid scintillator (for more information, see Fig. 2.1.1). Black dots (blue triangles) corresponds to far detector (near detector) data points from the 4rd calibration data (See Appendix A). Gray line corresponds to a schematic representation of the source deployment Guide Tube.

Table 5.1.1: H-fraction values for the different deployment positions in the γ-catcher Guide Tube, illustrated in Fig. 5.1.2. Last column representes the fraction between far and near detectors' H-fraction, $c_{\mathrm{H}}(\mathrm{FD{:}ND}) = \mathrm{f_H(FD)}/\mathrm{f_H(ND)}$

	Position (ρ, z) **[mm]**	$\mathrm{f_H(FD)}$	$\mathrm{f_H(ND)}$	$c_{\mathrm{H}}(\mathrm{FD{:}ND})$
Pos. 1	(146, 1535)	0.8928 ± 0.0029	0.8499 ± 0.0023	1.0504 ± 0.0044
Pos. 2	(1535, 1516)	0.9922 ± 0.0008	0.9633 ± 0.0016	1.0300 ± 0.0019
Pos. 3	(1654, 1426)	0.9908 ± 0.0008	0.9708 ± 0.0018	1.0206 ± 0.0021
Pos. 4	(1431, 0)	0.9858 ± 0.0007	0.9652 ± 0.0012	1.0213 ± 0.0014

Position 1 (close to the Chimney) has the lowest H-fraction, due to the proximity to the wall. *Position 2* and *3*, present almost all the captures on H-nuclei. In *Position 4*, the spill effect is considerable, but not as pronounced as the one observed in *Position 1*. In any case, the results are in accordance with previous calibration campaigns and the possible physical processes happening in the detector. However, a disagreement is found when far and near detector results are compared. The near detector presents in each of the situations a lower H-fraction. This discrepancy is even reaching $(5.0 \pm 0.4)\,\%$ for *Position 1*. And for *Position 2* and *3* the H-fraction is reduced to $(96 - 97)\%$ (instead of 99%, as the far detector). These discrepancies in all the positions are not covered by the statistical uncertainty.

In order to see the nature of these events, the visible energy spectra for each position is plotted in Fig. 5.1.3. Note for all the plots far and near detector data is represented in a logarithmic scale, where the histograms are scaled to the Hydrogen peak area. The expected energy distributions depend on the deployment source position. In *Position 1* and *4* some events in the 3.5-10 MeV range are expected due Carbon captures and spill effect. Nevertheless, for *Position 2* and *3* almost

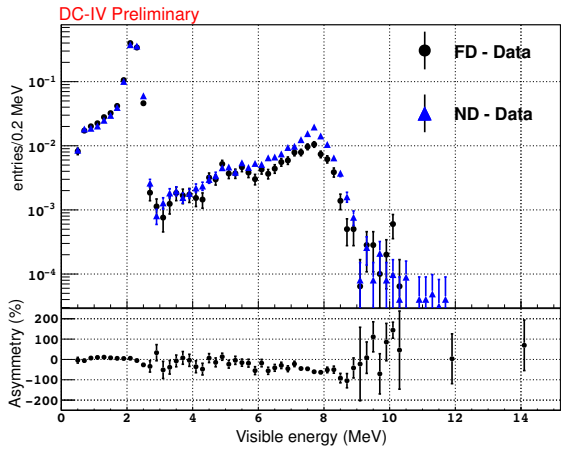

(a) *Position 1* - Chimney area.

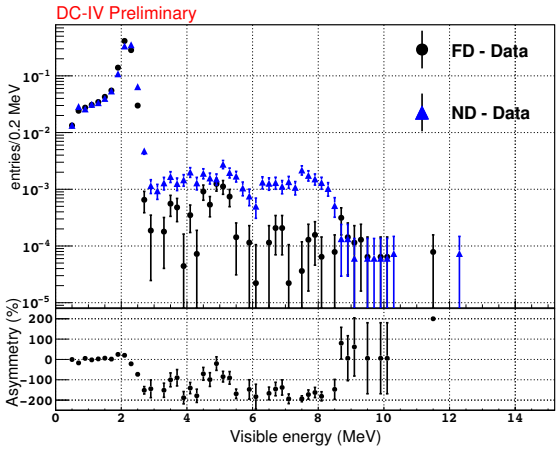

(b) *Position 2* - Corner.

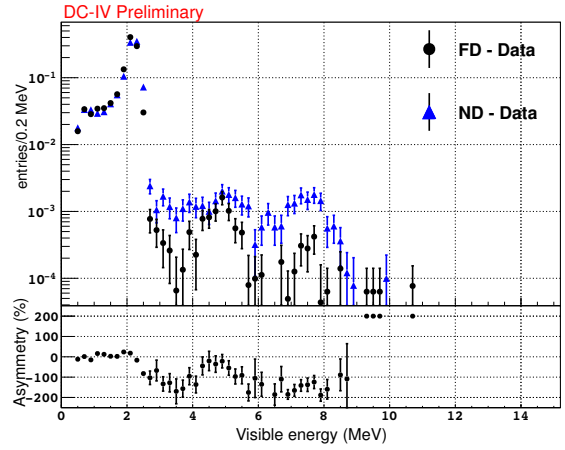

(c) *Position 3* - Corner.

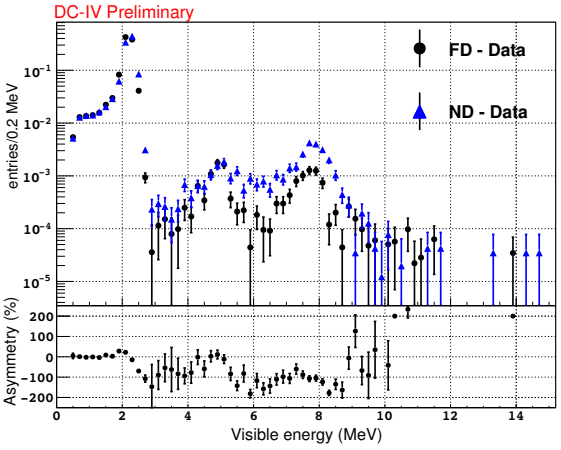

(d) *Position 4* - z=0 region.

Figure 5.1.3: Delayed energy spectra for far and near detectors data for different (x, y, z) positions in the γ-catcher. Data is taken from the 4th calibration data. Events are normalized to the [1.3, 3] MeV region (H-peak). Asymmetry plots corresponds to $2 \cdot \frac{A-B}{A+B}$ where A (B) is the FD (ND) number of events.

no events after the 6 MeV (after Carbon capture peak) are predicted. The obtained results in Fig. 5.1.3b and 5.1.3c does not reproduce the previously mentioned spectra. Looking into the asymmetry plots, the Hydrogen and Carbon capture peaks (at around 2.2 and 5 MeV) match really well between detectors. Nonetheless, the energy range where Gd-capture events should do not occur, presents a significant excess of events in the near detector data. Besides, a Compton tail of a possible 8MeV peak could be observed presenting a continuous amount of events between the 3.5 - 7 MeV. For the Fig. 5.1.3a and 5.1.3d an excess of events around 8 MeV are observed in both detectors because of spill-in to the ν-target. But looking into the asymmetry plot, the amount of events in the near detector is higher than in the far one. The magnitude of these events with energies in the Gd-capture region it is hard to estimate on from these logarithmic plots. But considering the obtained results on the H-capture fraction in Table 5.1.1 and the visual behaviour in Fig. 5.1.3 a significant discrepancy between far and near detector γ-catcher H-fraction is presented.

These results could be caused by different reasons that needed to be studied. For that reason, the rest of this chapter it is going to be focus on understanding the neutron capture efficiency in the γ-catcher. Next Section 5.2 it is going to be divided in different subsections analysing these high energy capture events.

5.2 Study on the far to near detector discrepancy

The obtained results from the Californium source deployment along the Guide Tube have represented an important investigation in this thesis. The H-fraction discrepancies in Table 5.1.1 could be caused by different reasons:

- A first idea to explain far and near detector discrepancy is a difference in the deployment position between detectors. Due to the closeness to the γ-catcher borders, the H-fractions are strongly sensitive to the deployment position due to spill efects.
- Another explanation could be that some H-capture gammas are lost in the detection. The H-fraction definitions are linked to the amount of events in both energy regions. And all the energy spectra are scaled to one of the capture peaks (in this case to the H-capture peak). If some of the H-capture events are lost (e.g, because they escape to the Buffer), the Gd-capture peak height could apparent look higher compared to the Hydrogen one. Consequently, the H-fraction will be reduced.
- In addition to all of these considerations, a final reason would be that the γ-catcher liquid is not free of Gd atoms in the near detector. With a non-zero Gd concentration, the excess of Gd-captures in this detector volume could be explained.

In order to investigate all of these possible explanations, several studies have been performed as a consequence. First of all, the source deployment position is going to be investigated. Secondly, two separated analysis in order to see if there is a deficit of H-capture gammas or an excess of Gd-capture events are performed. Finally, in order to see if a non-zero Gd-concentration is observed in the γ-catcher, a test using a Gd-loaded γ-catcher MC simulation is going to be done.

5.2.1 Study on the source deployment position

A shift in the Guide Tube deployed position could explain the increase of Gd-capture events in the near detector data. If the Californium source is close to the ν-target wall, an excess of Gd neutron capture events will be observed. In Fig. 5.2.1 first and second campaign Guide Tube data is represented, where at the right plot the H-fraction in terms of the distance to the nearest ν-target wall is also plotted [50]. From this figure it is possible to see that getting close to the ν-target wall

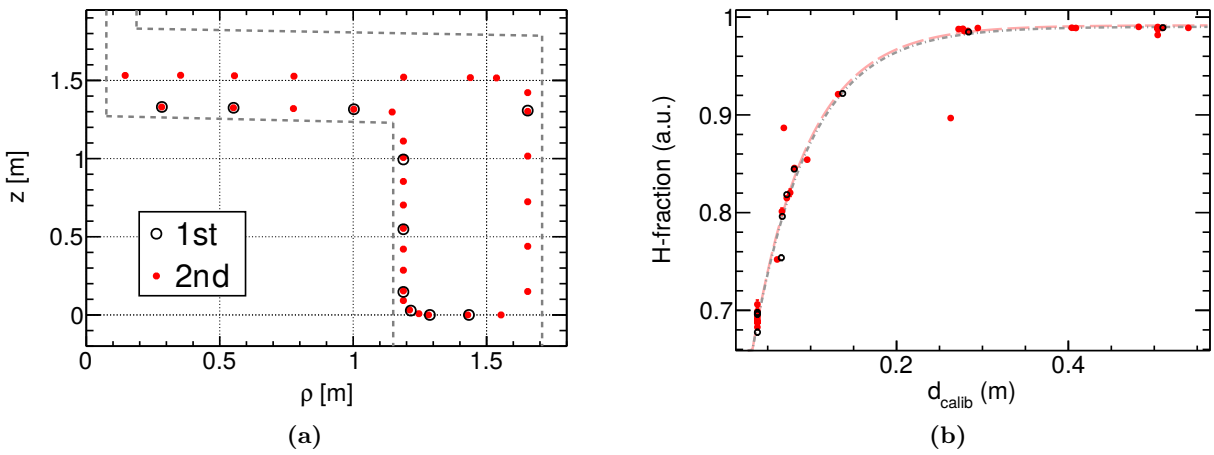

Figure 5.2.1: **(a)** Source position values in terms of (ρ,z) using the first and second calibration campaigns far detector data and **(b)** H-fraction values for this data in terms of the distance to the nearest ν-target wall d_{calib}. The H-fraction definition is the same one used in Eq. (3.4). Plots obtained from [50].

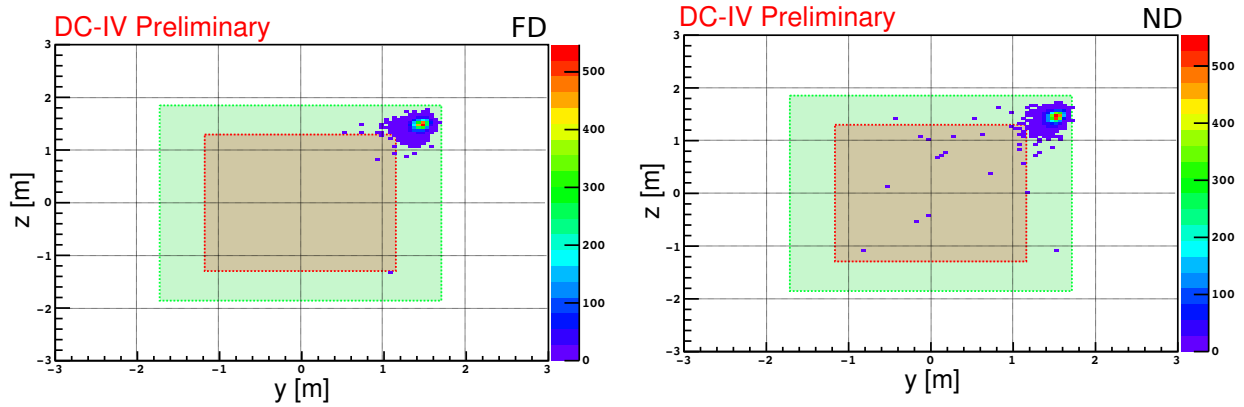

(a) *Position 2* - Corner (y, z) ≈ (1535, 1516) mm.

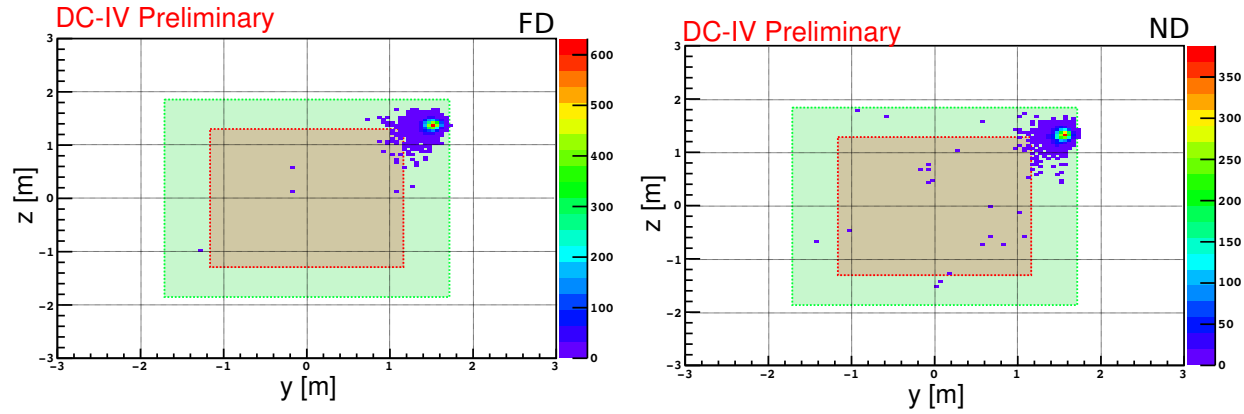

(b) *Position 3* - Corner (y, z) ≈ (1653, 1427) mm.

Figure 5.2.2: Prompt event reconstructed position in the (y, z) plane, for deployed sources at Guide Tube **(a)** *Position 2* and **(b)** *Position 3*. Red (green) volume represents the ν-target (γ-catcher).

the amount of H-captures is reduced as a consequence of the increase of Gd-events due to spill effect (see Section 3.2). The events occurring at the right upper corner in the γ-catcher (largest d_{calib}) have the most stable H-fraction around the unity. For those reasons, *Positions 1* and *4* are the most sensitive to small position discrepancies due to their proximity to the target, the Gd-loaded liquid scintillator. But in order to have a visible discrepancy between near and far detector results in *Position 2* and *3*, a significant shift in the deployment position should be observed.

One way to test if there is a position shift in the Californium source data is looking into the prompt events position reconstruction. Fission gammas are the first events observed from the Californium source correlated signal. Their reconstructed position is expected close to the deployment position. In order to observe a $(3-2)\,\%$ H-fraction discrepancy between far and near detector data at *Positions 2-3*, a discrepancy in the detectors prompt event positions should be observed (where the near detector prompt position should be closer to the ν-target wall). In Fig. 5.2.2 reconstructed prompt events positions are summarized for deployment *Positions 2* and *3*. These two dimension plots are without any background subtraction (off-time events). For that reason some prompt events are observed randomly distributed in the ν-target (red volume). Not taking into account these events, most fission gammas occur in the γ-catcher one. Red bins representing the most populated areas are at the same place that the already known deployment positions. And comparing both detectors prompt events, the source looks also deployed more or less at the same position for both of them. There are no signs of any significant position shift in the near detector data in comparison

with the far detector positions (more studies about deployment position in Section 5.2.3). From this study it is possible to conclude: initially deployed source position is not causing the discrepancy between detectors H-fraction.

5.2.2 Study on low energy captures in the Guide Tube data: the H-peak events

A loss of H-capture events is another suggested idea to explain the discrepancy at high energies between far and near detector data. Californium neutron captures depend mostly on their production position. Produced neutrons from deployments on the most cornered part of the Guide Tube could: be captured on γ-catcher Hydrogen nuclei emitting a 2.2 MeV gamma; travel to the ν-target being captured on Gadolinium nuclei emitting several gammas of 8 MeV (captures on other nuclei, as the ^{12}C, are also possible but with lower probability); or move to the Buffer or other "dead" detector volume (being lost). In Fig. 5.2.3 a drawing representing these two processes is shown. Emitted gammas after neutron capture produce scintillation light observed by the Buffer PMTs. H-captures gammas in deployment positions like *Position 2* and *3* could be lost due to their proximity to the inner detector border. The scintillation photons (represented in Fig. 5.2.3 with the orange circles) can scatter with the wall losing their energy, or can be lost from the detector volume. Consequently, a lower amount of 2.2 MeV events could be observed on the H-peak. The loss of capture gammas contribute to the Compton tail in each of the capture peaks (see Section 3.1 - Fig. 3.2.1). If the loss of 2.2 MeV H-capture gammas is higher in the near detector than in the far one, the H-fraction could be affected due to the reduction of events in the H-capture peak. Besides, as the energy

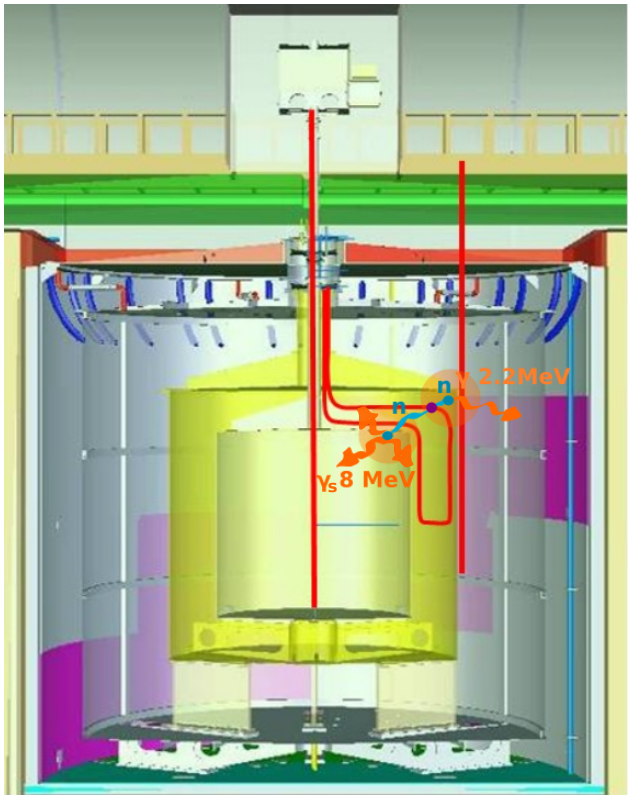

Figure 5.2.3: Depicted neutron capture processes from fission neutrons (blue dots) produced at the most corner part of the Guide Tube. Purple dot represents the source deployment position, and blue lines the neutron thermalization path. When they are captured (blue dots) gammas are emitted (orange arrows) and scintillator light is produced in the detector (orange circles).

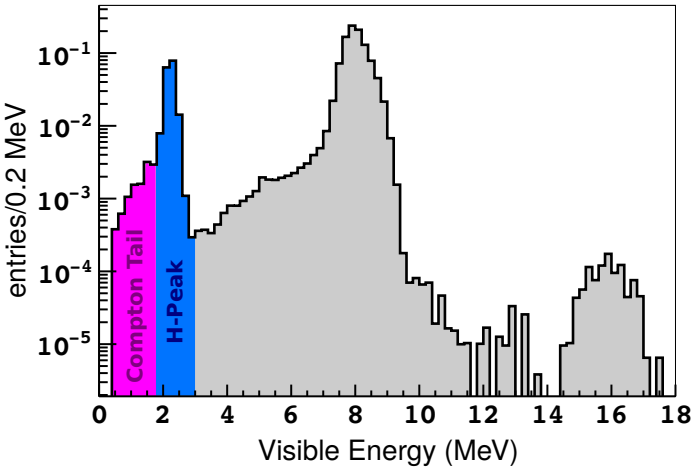

Figure 5.2.4: Delay energy spectra representing the energy regions for the Compton tail fraction on the Hydrogen events area $f_{CT}(H)$ selection. Pink region represents the Compton tail events, and dark blue the H-peak events.

spectra are scaled to the H-capture peak the events occurring with high energies could look larger. To analyse if that is the reason of discrepancy between far and near detector H-fraction results, a study of the H-peak events is done. If the amount of H-peak events is lower due to part of gamma energy loss, the number of events in the Compton tail should be higher. A way to study this effect is estimating fraction between the events on 2.2 MeV H-peak without any energy loss and the events with energy loss in the Compton tail. If the Compton tail ratio in the near detector is higher than in the far detector, the obtained results in Table 5.1.1 are consequence of H-capture events lost. In order to proceed to this study, a Compton tail fraction is going to be defined as

$$f_{CT} = \frac{\text{Number Compton tail events}}{\text{Number Compton tail + H-peak events}} . \tag{5.2}$$

For the Hydrogen peak area, energy regions to select the Compton tail events will be then

$$f^{H}_{CT} = \frac{N_{CT}}{N_{CT} + N_{Peak}} \quad \text{where} \quad \begin{array}{l} N_{CT} = N(0.5 < E_{visible} < 1.8\,\text{MeV}) \\ N_{Peak} = N(1.8 < E_{visible} < 3\,\text{MeV}) \end{array} , \tag{5.3}$$

where in Fig 5.2.4 these energy regions are represented. The used energy cuts are chosen to select the pure Hydrogen peak events on one side (taking the events with energies [1.8, 3] MeV) and the Compton tail events on the other side (with energies lower than 1.8 MeV).

The obtained values for this fraction (using the four positions on the Guide Tube data from Fig. 5.1.2) are summarized in Table 5.2.1. These results are also represented in terms of the spherical coordinate $R = \sqrt{x^2 + y^2 + z^2}$ in Fig. 5.2.5. A different value of the f^{H}_{CT} in each position is obtained. Because the loss of H-capture events is increased for deployment positions close to the inner detector border, as it is seen in Fig. 5.2.5. *Positions 2* and *3* are the most sensitive to Hy-

Table 5.2.1: Values for the f^{H}_{CT} in each of the Guide Tube deployment positions from Fig. 5.1.2 for both detectors.

	Position (ρ, z)	f^{H}_{CT}(FD) [%]	f^{H}_{CT}(ND) [%]
Pos. 1	(146, 1 535) mm	15.97 ± 0.36	15.11 ± 0.24
Pos. 2	(1 535, 1 516) mm	20.83 ± 0.34	20.76 ± 0.33
Pos. 3	(1 654, 1 426) mm	22.12 ± 0.34	21.69 ± 0.40
Pos. 4	(1 431,0) mm	10.90 ± 0.18	10.71 ± 0.19

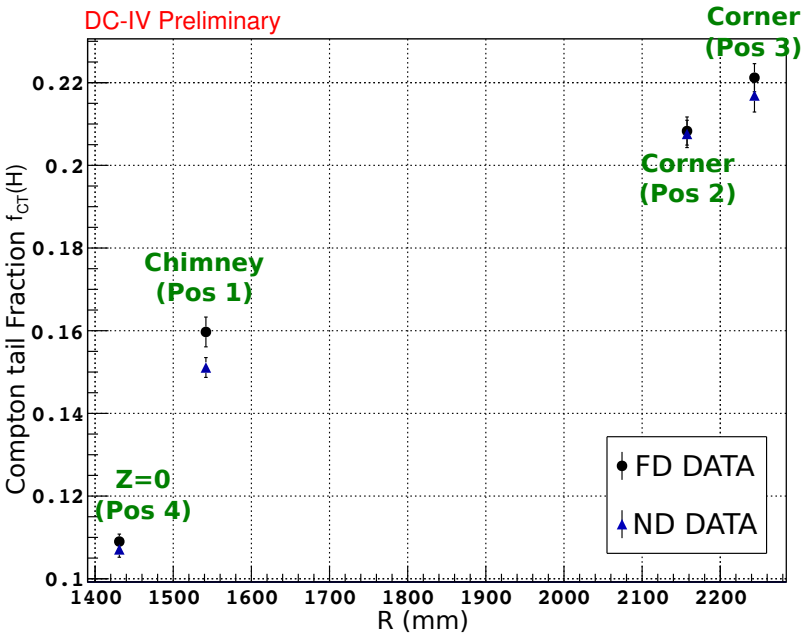

Figure 5.2.5: Fraction of Hydrogen capture events in the Compton tail represented in terms of the deployment position in the spherical coordinate R = $\sqrt{x^2+y^2+z^2}$. Values for both detectors obtained from Table 5.2.1.

drogen capture events lost, presenting a fraction of events on the Compton tail around $\sim 21/22\,\%$. In contrast, the *position 4* (closest to the ν-target wall) has only a 10 % of Compton tail events. Comparing far and near detector data results in each position, both detectors present similar fraction of events on the Compton tail region. And the values are in agreement within their statistical uncertainty. These results do not show any significant Hydrogen capture loss on the near detector that could explain the near and far H-fraction discrepancy. Also the Fig. 5.2.5 results confirm the previous subsection conclusion, no shift on the deployment positions is observed with reference to the values from Appendix A.

5.2.3 Study on high energy captures in the Guide Tube data: position reconstruction and capture times estimation

On previous subsections deployment positions were studied in order to see if a position shift was causing the discrepancy between near and far detector H-fractions. The no shift observation and the proof of no H-capture events loss bring this study to the next step. Gd-capture candidates are observed, and they are visible at high energies for deployment *Position 2* and *3* on Fig. 5.1.2. In order to study if these events are caused by spill-in effect, the reconstructed position and the capture time for the neutron capture events at high energies is going to be studied.

Vertex reconstruction. if the high energy events are caused in ν-target can be known via their position reconstruction. Besides, this study can help to finally understand if there is either a position shift or a wrong vertex reconstruction in the near detector data. Events are going to be selected as it was described in Section 3.1.2, with a different delay event energy criteria:

- For *Position 2* and *3*, the events with delayed energies higher than 3.5 MeV are going to be selected (from Fig. 5.1.3b and 5.1.3c). As only Gadolinium capture peak energy regions will not have enough statistics for an analysis, the Compton tail and the Carbon energy capture region is also included.

- In addition, the *Position 4* events are going to be studied. But in this case, as the high energy regions present a higher statistics (due to spill effect) only the events with delayed energies above 6 MeV are going to be analised (Fig. 5.1.3d). In that way, the Carbon events are going to be avoided and only the 8 MeV excess due to the Gd-captures is going to be studied.

Table 5.2.2: Visible energy criteria for prompt and delayed events for the position reconstruction study. The other correlated criteria for the Cf selection are the defined ones in Section 3.1.2.

	Position (ρ, z) [mm]	Prompt events energy	Delayed events energy
Pos. 2	$(1535, 1516)$	$4 < E_{vis} < 10$ MeV	$3.5 < E_{vis} < 25$ MeV
Pos. 3	$(1654, 1426)$		
Pos. 4	$(1431, 0)$		$6 < E_{vis} < 25$ MeV

In Table 5.2.2 the selection energy criteria used for prompt and delayed events is summarized. For these selected events, the reconstructed coordinate ρ^2_{reco} is going to be studied for each of the correlated signals. On one hand, looking into the prompt events reconstructed position, the real source position can be better tested than in Subsection 5.2. Any shift between detectors distribution can give a hint about a shift in the source. On the other hand, the delayed events are studied. If these events are occurring in the ν-target because spill effect, they will present a $\rho^2_{reco} < \rho^2_{NT}$ (see ν-target and γ-catcher limits in Section 2.1.1). Events happening in the γ-catcher (as Carbon captures) by contrast will have $1.323 < \rho^2_{reco} < 2.917\,m^2$. The obtained position distributions for prompt and delayed events are plotted in Fig. 5.2.6. Prompt events are represented without the accidental background subtraction (off-time events are included). Red and green lines represent the limits for the ν-target and γ-catcher, respectively. Additionally, the theoretical source position is represented with a gray line. Prompt and delay event distributions are illustrated with their mean value. For prompt events this is a useful tool to test any deployment position shift. In Table 5.2.3 the theoretical deployed positions and the distributions mean values are summarized for both detectors.

Comparing these results, all the reconstructed distributions mean values are slightly below to where the source is expected to be. It is caused by a bias in the vertex position reconstruction. From studies using the ^{60}Co calibration source [51], a negative bias towards the detector center is noticed in the far detector. Consequently, the reconstructed prompt positions are observed slightly negatively shifted in far detector data. The near detector reconstructed mean values are close to the far detector ones. It seems that this position shift is also observed in the near detector data, with probably a lower shift (because mean values are higher for the near detector values than for the far). From these observations, it is possible to conclude a small shift in the vertex reconstruction is observed in far and near detector data. But with no significant impact on these studies because a similar shift is observed in both detectors.

From the prompt event reconstructed position study no evidences of position shift between detectors are observed. Then, it is possible to compare the delayed events ρ^2_{reco} in Fig. 5.2.6 for both detectors. For *Position 2* and *3* (Right plots in Fig. 5.2.6a and 5.2.6b) the events present a similar behaviour.

Table 5.2.3: Mean values for the prompt events reconstructed position distributions, using far and near detector data in different deployment positions. Results from Fig. 5.2.6.

	Position - $\rho^2_{theo.}$	$\overline{\rho}^2_{reco}$ (FD) [m^2]	$\overline{\rho}^2_{reco}$ (ND) [m^2]
Pos. 2	2.355 m^2	2.06 ± 0.02	2.19 ± 0.02
Pos. 3	2.735 m^2	2.28 ± 0.02	2.26 ± 0.02
Pos. 4	2.048 m^2	1.64 ± 0.02	1.79 ± 0.02

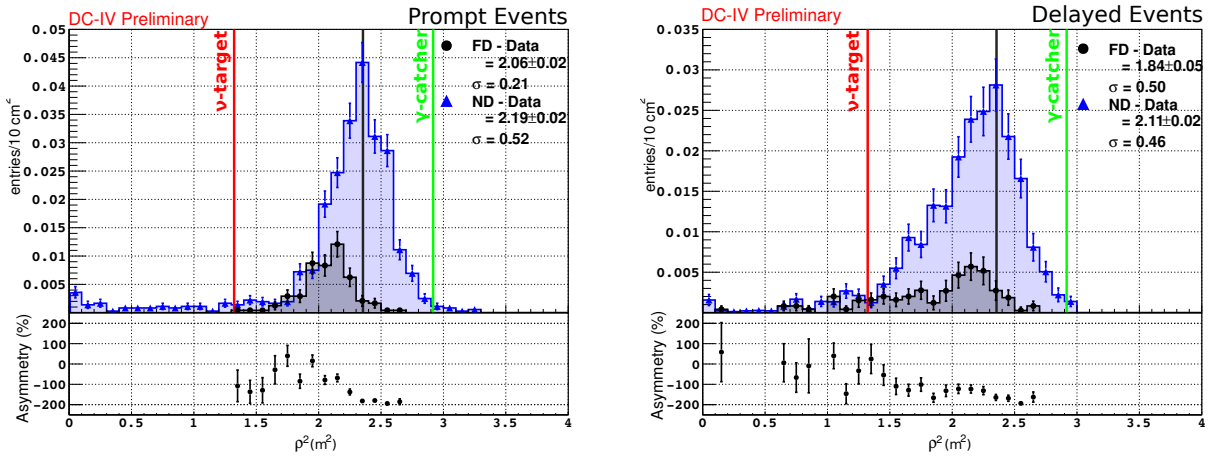

(a) Position 2 - Corner.

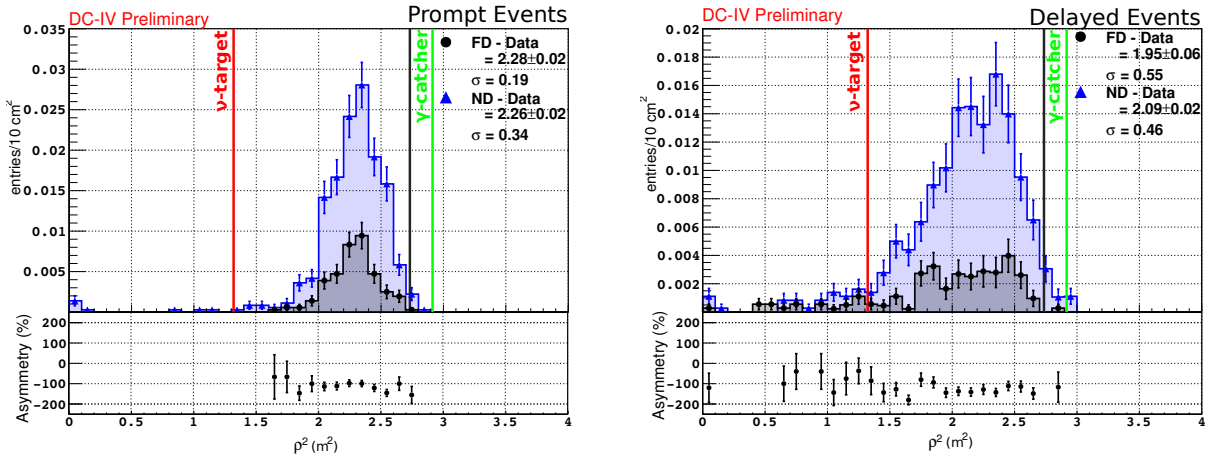

(b) Position 3 - Corner.

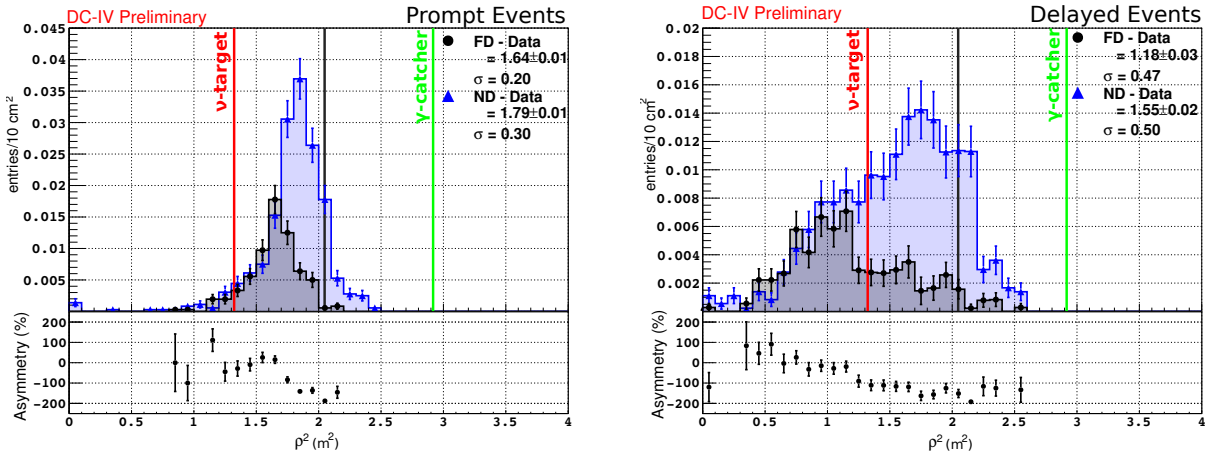

(c) Position 4 - z=0 region.

Figure 5.2.6: Vertex reconstruction for prompt (**left** plots) a delayed (**right** plots) events in several Guide Tube deployment positions. Blue (black) distribution corresponds to far (near) detector events. Both distributions are normalized to deployment time of the source in each position. The red (green) line is the limit of the ν-target (γ-catcher) wall, and the gray line corresponds to the theoretical deployed position. Prompt events are without the accidental subtraction.

For $\rho^2_{\text{reco}} < \rho^2_{\nu\text{-target}}$ far and near detector events present the same distribution and amount (looking into the asymmetry plot, values are in agreement with 0). These events are caused by the neutrons travelling into the ν-target and being captured on Gd- or C-nuclei. For $\rho^2_{\nu\text{-target}} < \rho^2_{\text{reco}} < \rho^2_{\gamma\text{-catcher}}$ both detectors present some events. In this region, captures on Carbon nuclei are in principle the only possible measurable effect. This could be the reason of events in this volume. However, the height is different in both detectors' distributions. More events with $E_d > 3.5\,\text{MeV}$ are observed in the near detector γ-catcher. *Position 4* (Fig. 5.2.6c) shows the same behaviour, but with much larger spill component. In this case only Gd captures in the ν-target should be contributing, because the events are selected with $E_d > 6\,\text{MeV}$. While for the far detector almost all the events occur in this volume, and some isolated events are observed in the γ-catcher (maybe due to wrong reconstructed spill events, or some background events not well subtracted). Near detector events are mainly observed in the γ-catcher volume. For $\rho^2_{\text{reco}} < \rho^2_{\nu\text{-target}}$ far and near detector distributions match really well. The spill events present the same amount in both detectors. Nevertheless, the significant discrepancy is observed for the γ-catcher volume ($\rho^2_{\nu\text{-target}} < \rho^2_{\text{reco}} < \rho^2_{\gamma\text{-catcher}}$) where the near detector presents an increase of events in this region.
In the three deployment positions far and near detector events with high energies match really well in the ν-target region. Spill events occur with the same intensity in both detectors. But in the near detector more capture events are measured in the γ-catcher volume than what would be expected from the values in the far detector.

Capture time. In order to understand a little bit more about the nature of these high energy events, an independent analysis to the position reconstruction study is going to be applied. The capture time provides enough information to test in which scintillator liquid captures are occurring (to test spill effect). The way to estimate it is from the correlation time distributions. They behave under the exponential distribution,

$$N(\Delta t) = N_0 \cdot e^{-\Delta t/\tau_0} + B_0 \quad , \tag{5.4}$$

where N_0 and B_0 are constants, and τ_0 is the capture time. A fit in the correlation time distributions can be applied under this distribution for the τ_0 estimation. High energy events (energy region where Gd- and C-captures occur) fulfilling the Table 5.2.2 criteria are going to be analysed. Besides, it is going to be applied also into the low energy events caused by H-captures (same definitions than before but with $E_{vis} < 3.5\,\text{MeV}$). On that way, these expected results are going to be taken into account:

- If captures happen in the same liquid, the capture time will be the same (intrinsic to the liquid). It does not matter on which nuclei these captures occur.
- In case of any spill effect, it is known from spill studies that the closer to the ν-target the source is, the shorter the capture time is going to be. That means that positions like *4* should present a capture time shorter than positions like *2* and *3*.

In Fig. 5.2.7 the correlation time distributions, and fitted functions and parameters are represented for high energy events. Besides, the obtained results for both high and low energy events capture times are summarized in Table 5.2.4. Low energy events (H-captures) present a faster capture time in the near detector for *Positions 2* and *4*, compared to the far detector. *Position 3* presents the same capture time in both detectors. However, the detector differences in *Positions 2* and *4* are within the 2 sigma fluctuations of the *Position 3* result. High energy results for *Position 2* and *3* present a similar capture time in the near detector, which is consistent with the obtained values for the H-capture events. This means that the captures are occurring in the same liquid for low and high energy captures in the near detector. In contrasts, the far detector results are

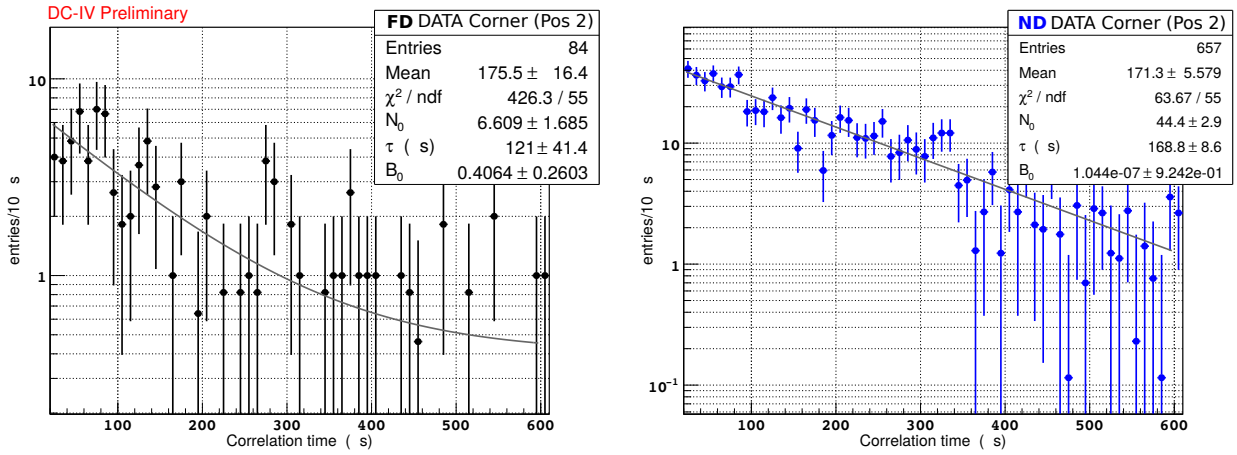

(a) Position 2 - Corner.

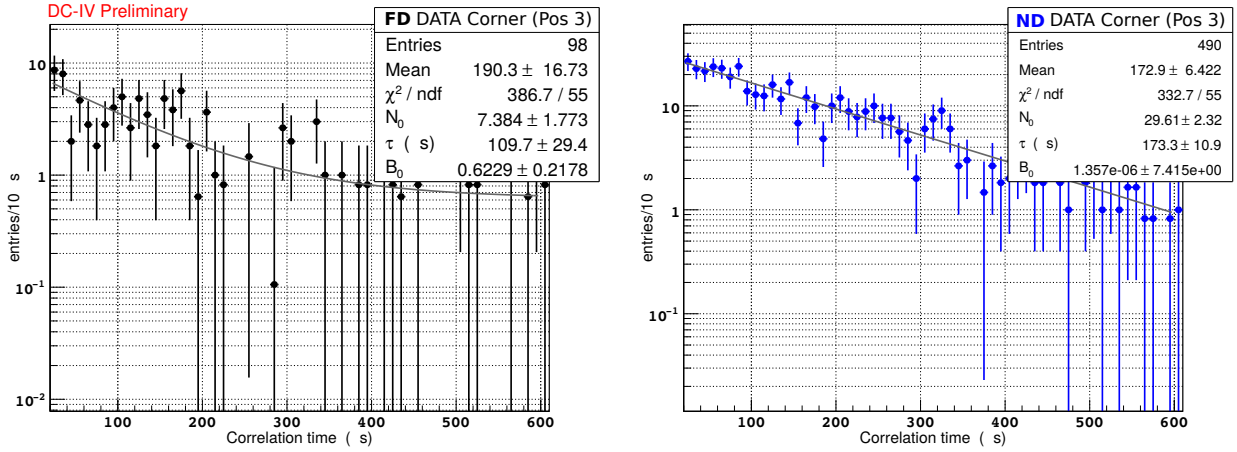

(b) Position 3 - Corner.

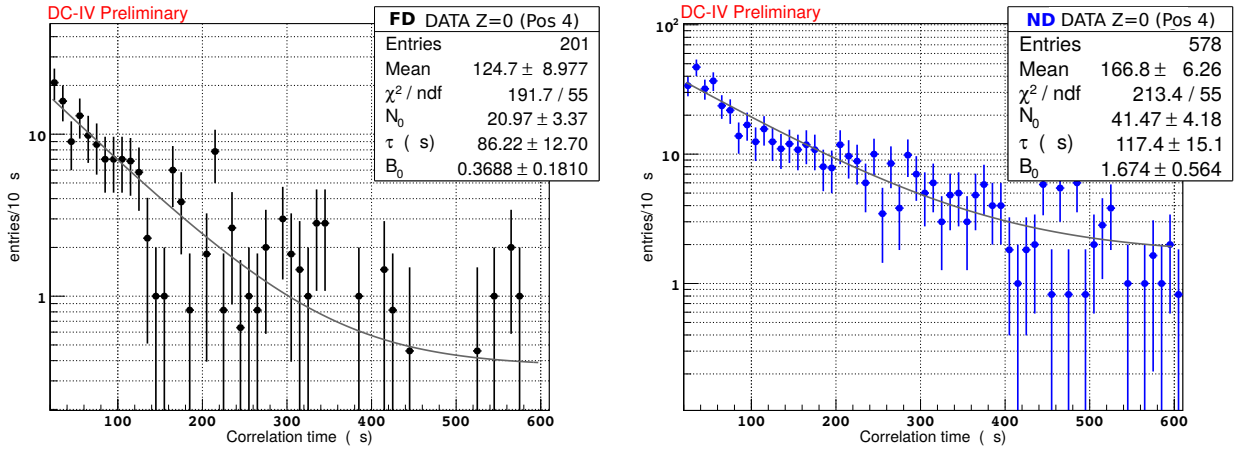

(c) Position 4 - z=0 region.

Figure 5.2.7: Correlation time distributions for high energy events in different deployment positions. Far detector in left distributions (black dots) and near detectors in right distributions (blue dots). Gray lines corresponds to the fitted function under Eq. (5.4) considering the parameters in the distributions boxes.

Table 5.2.4: Capture times obtained considering low and high energy capture events in several deployment positions. Fits are made following the Eq. (5.4). Other parameters results in Fig. 5.2.7.

Position	**H-capture** τ_0 [μs]		**High energy** τ_0 [μs]	
	FD	ND	FD	ND
Pos. 2	193 ± 3	179 ± 5	121 ± 41	169 ± 9
Pos. 3	188 ± 6	188 ± 3	110 ± 30	173 ± 11
Pos. 4	195 ± 2	184 ± 2	86 ± 13	117 ± 15

lower with reference to the near detector. It is caused by the spill events, captures at high energies being observed in the γ-catcher. However, it is important to note here that *Position 2* and *3* with high energies present not enough statistics to obtain an accurate capture time estimation. For *Position 4* (higher energies, $E_{vis} > 6\,MeV$, events with no ^{12}C contribution) a different value is again observed between far and near detectors but this time even with a statistical significance. Near detector capture time is lower than in the other positions because some spill effect is observed in this Guide Tube position (Fig. 5.2.6c). However, it is not as low as in the far detectors. This indicates the source position in the ND has less spill contribution into the target, although the Gd-fraction is higher. And different capture times mean that the captures of these high energy events do occur in the same volume but apparently different liquid compositions in both detectors.

These results discard any spill effect or a position reconstruction shift as a solution for Gd capture candidates in the γ-catcher. Considering these studies results, and the obtained ones from the vertex reconstruction study in the ρ^2 axis, a similar conclusion is found. High energy events are occurring in the γ-catcher volume, and not in the ν-target liquid. These events have energies $E_{vis} > 6\,MeV$, which means that could be caused by Gd capture candidates. Combining these studies and the obtained values for the H-fraction estimation in Table 5.1.1, a possible contribution of neutron captures in Gd-nuclei are added to the events in γ-catcher. In order to test if this is reason of discrepancy between far and near detector values, a simulated MC with a γ-catcher loaded of Gd is going to be studied in the next subsection.

5.2.4 Study on a Gd-loaded γ-catcher MC simulation

The obtained results in the previous analyses have proved an evidence of high energy events in the γ-catcher which could be caused by captures on Gd in the near detector. As all the results from these studies pointed to a possible contribution of Gd-compounds in the γ-catcher, a near detector MC simulation sample has been generated considering a Gd-concentration in it. This concentration has been estimated considering the observed discrepancy along the γ-catcher Table 5.1.1 (depending on the position within a $\sim (2-3)\%$ discrepancy). An exchange of about 50 litres of liquid scintillator between the near detector ν-target and γ-catcher volumes can be causing these neutron capture fraction discrepancies in both volumes [52]. This concentration will mean the addition of 2.4 mg/l of Gd-compunds in the γ-catcher assuming homogeneous distribution. The analysis of a MC simulation considering this Gd-concentration can test the possibility of these nuclei in the near detector liquid scintillator.

This analysis is going to be performed on for *Position 2* $(\rho, z) = (1535, 1516)$mm. In this deployment position no high energy events are expected (with a small contribution of spill events), and the analysis can be better performed. Two new near detector MC simulations of ^{252}Cf events have been generated. First of all 50 000 neutrons have been generated in a normal detector configuration. Secondly, again 50 000 neutrons have been produced in the same position, but in this

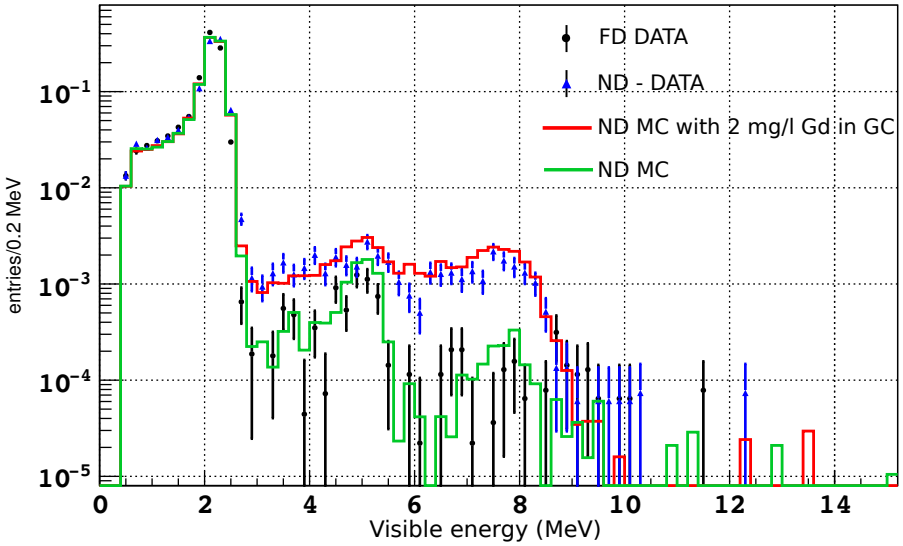

Figure 5.2.8: Delayed energy spectra using fourth calibration campaign data in far (black dots) and near (blue triangles) detectors, and the new near detector MC simulations considering (red line) or not (green line) a Gd-concentration in the γ-catcher. Events are normalized to the events in the Hydrogen peak, energy regions of [1.3, 3.5] MeV.

case considering the Gd-concentration of 2.4 mg/l in the γ-catcher (a factor 400 dilution compared to the ν-target). All the simulation information is included in the Appendix A. These new MC simulation samples have been compared to the far and near detector data in this *Position 2* using the fourth calibration campaign data.

The energy distributions for the neutron captures using these four data and MC samples are plotted in Fig. 5.2.8. Events are normalized to the H-peak events, in order to better observe the high energy region discrepancies. A first look into these events shows an agreement between near detector data and the MC simulation considering a Gd-concentration. Carbon and Gadolinium capture peaks are well reproduced in the MC simulation. Meanwhile, the near detector MC simulation with a normal liquid concentration matches with the far detector data. Being in this case a well represented Carbon peak in both samples. In order to study these data and MC samples quantitatively, two studies are going to be performed. On one hand, the H-fraction is going to be estimated in the MC simulation samples to compare it with the previous data results (in Table 5.1.1). On the other hand, the capture times are going to be computed for the MC simulation samples and again compared to the previously obtained results in Table 5.2.4.

Hydrogen fraction estimation. A first look into the new MC simulation data with Gd shows a good agreement with the near detector data. The H-fraction has been estimated to know in which level the γ-catcher with a concentration of Gd agrees with the near detector data. The H-fraction definition was already written in Eq. (3.4), where its statistical uncertainty can be computed considering Eq. (3.12). The obtained results for the previously mentioned four data and MC samples are summarized in Table 5.2.5. In this position far and near detectors data differ by $(2.89 \pm 0.18)\,\%$. Where the near detector data to the MC simulation without Gd concentration disagree with a discrepancy of $(2.66 \pm 0.16)\,\%$. From these numbers the same result that in Fig. 5.2.8 is obtained: the near detector data disagree in the same way with the far detector data than with the MC simulation without any Gd-concentration. For the obtained H-fractions using

Table 5.2.5: Fraction of Hydrogen captures following the definition of Eq. (3.12), for far and near detectors fourth calibration campaign data and MC simulations from Appendix A. Uncertainties are only statistical (using Eq. (3.12)).

	$\mathbf{f_H}$ [%]
Far Detector DATA	99.22 ± 0.08
Near Detector DATA	96.33 ± 0.16
Near Detector MC	98.99 ± 0.04
Near Detector MC with Gd	95.65 ± 0.08

the near detector data and the MC simulation with a concentration of Gd, a difference of only (0.68 ± 0.18) % is obtained. It seems that the discrepancy between near detector data and MC (without any Gd-concentration) is covered assuming that some Gd is present in the γ-catcher.

Capture times study. From the previous study a good agreement between near detector data and a Gd-loaded γ-catcher MC simulation has been observed. This could mean that the extra events observed for high energies can be caused by Gd-captures. However, to completely understand the nature of these high energy events (where these captures occur) their capture time is going to be computed. The same event selection than in the previous section is going to be applied: events are selected as in the Section 3.1.2, splitting the delayed events in two samples. Low energy events selected with $E_{vis} < 3.5\,MeV$ to study the H-capture region, and high energy events with $E_{vis} > 3.5\,MeV$. This selection has been applied into far and near detector data, and the two new MC simulation samples. The correlation times for these two samples has been fitted under the function Eq. (5.4), where the parameters B_0, N_0, and capture time τ_0 has been obtained. Some of the correlation time distributions and its fitted $N(\Delta t)$ function are plotted in Fig. 5.2.9. The obtained capture times are summarized in Table 5.2.6.

For low energy events (H-capture energies) the far detector data and the near detector MC simulation without any Gd-contribution in the γ-catcher have a similar capture time. However, the Gd in the γ-catcher shortens the capture time for H-captures. This reduction is expected when we have Gd in the γ-catcher, and is observed in the near detector data (reduction also pointed in previous subsection 5.2.3). For high energy events, due to spill events in the far detector data and the MC simulation without Gd a shorter capture time is observed. By contrast, the MC simulation with Gd-concentration presentes a higher capture time. This increase in the MC file is related to the addition of Gd-captures compared to the Carbon ones and spill events. In the near detector data, a similar value to this MC simulation one is estimated.

From these estimations, it is observed that the near detector capture times for low and high energy events behave in the same way that the MC simulation considering a Gd-concentration in the γ-catcher. Besides, the Hydrogen fractions obtained with the same samples are in agreement. With this results, the possibility of a Gd-concentration in the near detector γ-catcher explaining the detectors discrepancy is affirmed.

Table 5.2.6: Capture times for low and high energy neutron capture events, using far and near detectors fourth calibration campaign data and MC simulations from Appendix A. Values and their uncertainties obtained from the correlation time fit to the Eq. (5.4).

	H-capture τ_0 [μs]	**High energy** τ_0 [μs]
Far Detector DATA	193 ± 3	120 ± 40
Near Detector DATA	179 ± 5	169 ± 9
Near Detector MC	191 ± 2	114 ± 4
Near Detector MC with Gd	188 ± 3	166 ± 4

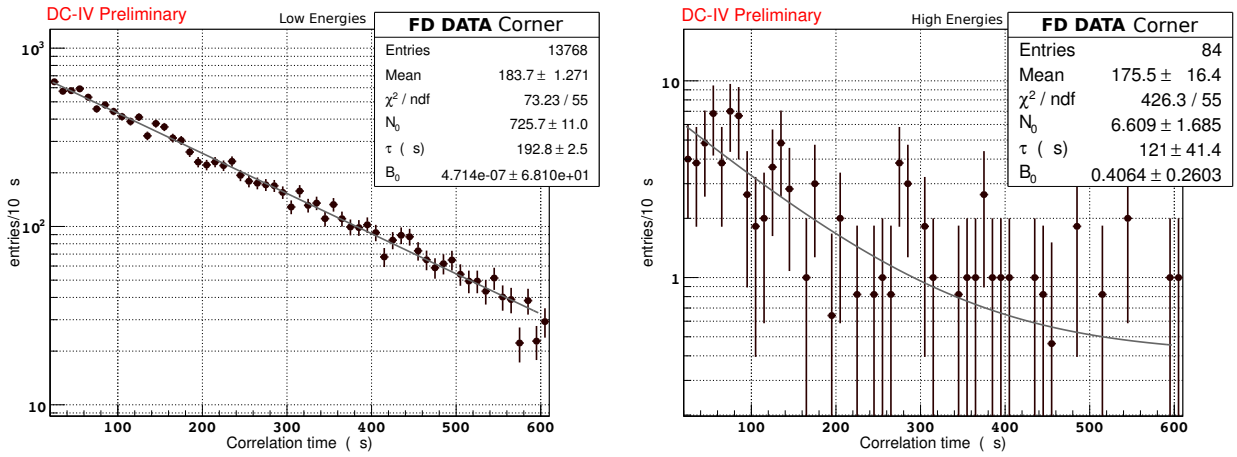

(a) Far detector data.

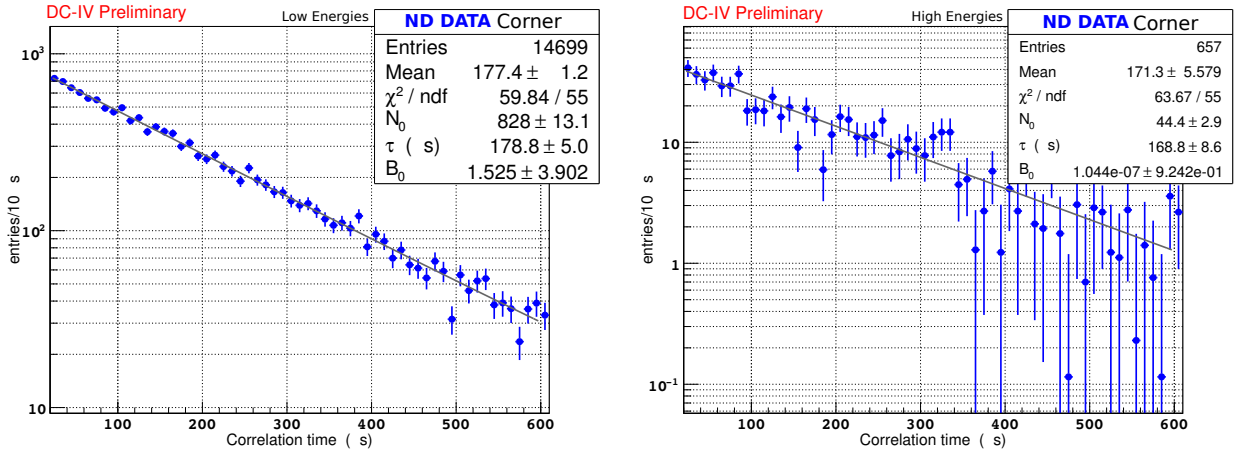

(b) Near detector data.

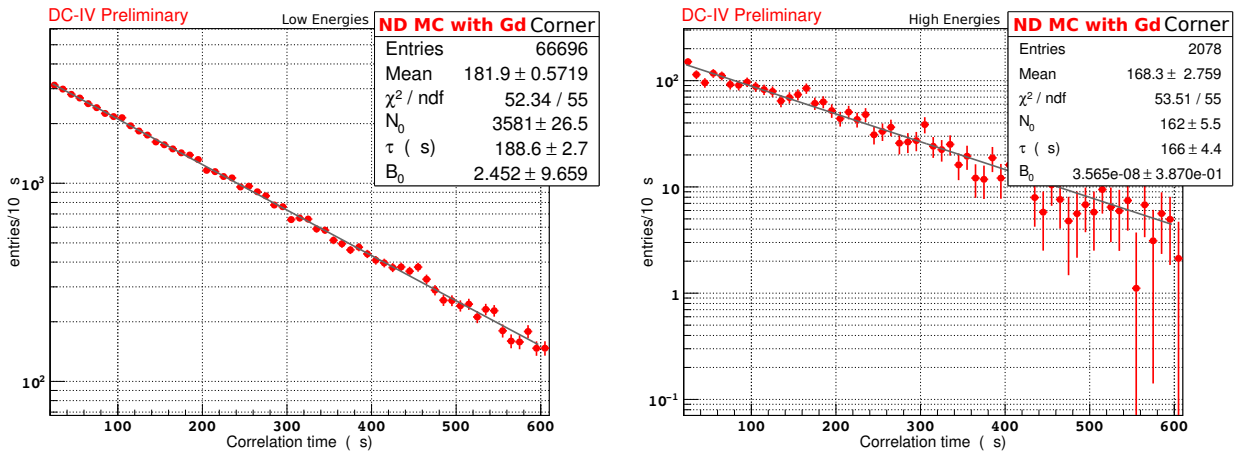

(c) Near detector MC with a Gd-concentration.

Figure 5.2.9: Correlation time distributions for low (left plots) and high energy events (right plots) for deployment position *2* in different data samples. Gray lines corresponds to the fitted function under Eq. (5.4) considering the parameters in the distribution boxes.

5.3 Conclusion

Along this chapter, the obtained results for the neutron detection efficiency in the γ-catcher using the fourth calibration campaign ^{252}Cf data have been studied. In the estimation of the Hydrogen neutron capture fraction f_H, a discrepancy between far and near detector data has been observed. The Hydrogen neutron fraction has shown a deficit in the near detector data, reaching a discrepancy of $\sim (2-3)\,\%$ between detectors (depending on the deployment position). This discrepancy is reflected in a difference of the energy spectra, where at high energies near detector data presents an excess of events with reference to the far detector events. Several analyses have been considered in order to explain this discrepancy. Some conclusions have been found from them:

- The difference is not caused by a deployment position shift. Californium prompt events has been reconstructed confirming that approximately the same deployment positions are used for both detectors.
- The excess of high energy captures is not caused by a loss of Hydrogen capture events. No significant increase of the fraction of Compton tail events is observed in the near detector data with reference to the far detector estimation. Besides, the same ratio of Compton tail events is observed (below Hydrogen capture peak) in both detectors positions, confirming the no deployment position shift.
- This excess of high energy events is not caused by spill-in effect. Analysing the high energy events ($E_{vis} > 6\,MeV$) reconstructed position, in the near detector data most of the events occur in the γ-catcher volume. While for the far detector data only contributions from ν-target spill effect are observed. In addition, the capture time of these high energy events has been analysed, proving that high energy captures occur in the same liquid than the low energy captures (because same capture time is observed in both energy ranges).

These results point towards a Gd contamination in the near detector γ-catcher. To know if a contribution of Gd-compounds in the γ-catcher is measured, a near detector MC simulation sample considering a Gd-concentration in it has been analysed. For the estimation of Gd-concentration value, the detectors discrepancy on the H neutron capture fraction on γ-catcher Guide Tube data ($\sim 2\%$, depending on the position) has been considered. In this analysis, the following was found:

- Considering Gd in the γ-catcher the discrepancy between data and MC is significantly reduced. The obtained H-fraction using this Gd-loaded MC simulation differs with the near detector data only by $(0.68 \pm 0.18)\%$.
- A similar capture time τ has been measured on the MC simulation with Gd and the near detector data.

Considering all the obtained results, the possibility of some Gd-nuclei in the γ-catcher liquid scintillator has been confirmed. At this stage of the Double Chooz analysis, other alternative and parallel studies had been performed. First of all, some γ-catcher liquid scintillator samples taken during the near detector construction had been chemically analysed. To either know if some Gd was accidentally added to the γ-catcher liquid during the liquid scintillator production at the Max-Planck-Institut für Kernphysik, or during the detector filling in Chooz. Some chemical tests (performed separately) neglected both possibilities, with no observation of Gd-nuclei in the samples [53]. With this information the idea of a possible leak between the ν-target (liquid scintillator loaded with Gadolinium) and the γ-catcher volume (Gd-free liquid scintillator) after the near detector construction had to be considered. Therefore, Cf neutrons and other neutron sources were used to study the time stability of the H-fraction in the γ-catcher.

Californium source fifth calibration campaign data: the fifth calibration campaign data in the Guide Tube had been analysed by G. Yang (IIL Chicago - USA) [54]-[55], where the fraction of Gd-captures in several source deployment positions were studied.

- In the top-corner part of the Guide Tube (called *Position 2* along this chapter), a significant increase between fourth and fifth calibration campaigns is observed. It is important to point that G. Yang fourth calibration campaign results presented a quantitative discrepancy with the obtained values along this chapter (probably caused by the addition of a fiducial cut on the neutron vertex). But they are in a qualitative agreement, where the Gd-fraction is two times higher in the new calibration campaign.
- Several deployment positions along the γ-catcher z=0 had shown a stability between calibration campaigns, with a no significant increase of the H-fraction.
- Additional Guide Tube positions along the the γ-catcher wall presented a constant f_{Gd} for far and near detectors, where in all the positions a discrepancy of around 2% has been observed.

Spallation neutrons: these background neutrons were analised by T. J. C. Bezerra (Subatech Nantes - France) [56] to study the neutron capture on Gd-nuclei during the whole data taking period and taking into account the full ID volume. In order to perform this study, the detector volume was divided in different regions for a separate n-Gd fraction check. The Gd-fraction was defined selecting only the H and Gd peaks (in this way, the Carbon captures were avoided). And the data samples (run lists) were divided in three samples of equal time. For far detector, a stable and low Gd-fraction was observed in the entire γ-catcher volume in terms of time. However, the near detector neutron Gd-fraction seemed to be increasing within one year (around a 1% increase) around the top part of the γ-catcher. And no evidences of excess Gd captures in the bottom part of the γ-catcher were found.

IBD neutrons: T. J. C. Bezerra [56] studied them to estimate the neutron capture on Gd-nuclei for different detector volume regions as previously mentioned for spallation neutrons. Using the

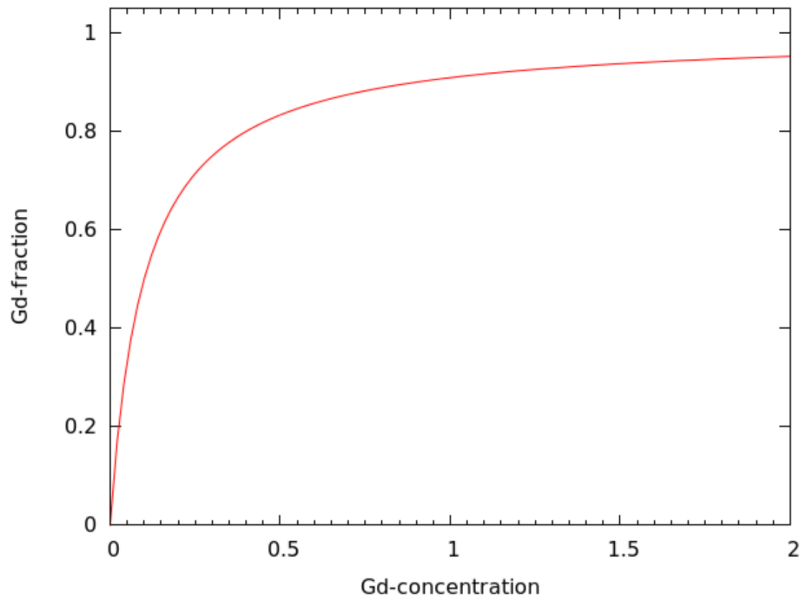

Figure 5.3.1: Illustration about the Gd-fraction trend in terms of the Gd-concentration in the liquid scintillator [52].

same Gd-fraction definition, the near detector presented an excess of events in the γ-catcher top-corner part (exactly in the same region as in the Spallation neutron analysis). Besides, D. Navas [57] performed several analyses in the neutron detection considering different IBD selection cuts. The obtained results were also consisten with the hypothesis of an amount of Gd-compounds in the γ-catcher liquid scintillator.

All the presented results along this chapter, and the previously mentioned analyses provided enough information to conclude the existence of a leak between near detector volumes. Through this leak, ν-target liquid scintillator molecules were transferred to the γ-catcher. This liquids exchange seems to be occurring gradually since the near detector construction, as it has been observed from the spallation neutron study. The exchange of liquid scintillators could explain the detector discrepancy in the Gd-fraction at the target center observed in Chapter 4. In Fig. 5.3.1 the Gd-fraction (number of neutron Gd-captures) is illustrated in terms of the Gd-concentration of the liquid. For high Gd-concentrations, a small reduction slightly decreases the number of Gd-captures. And in the near detector data a $\sim 0.2\%$ reduction was observed. For lower concentrations (or zero) the addition of Gd-nuclei significantly increases the Gd-fraction. A Gd-concentration at the level of few mg/litre matches with the observed γ-catcher discrepancy between the detectors' H-fractions. These results have been a turning point for the Double Chooz analysis. In order to perform a θ_{13} analysis, this leak and its effects on the γ-catcher liquid scintillator properties need to be well understood.

Summary

The Double Chooz (DC) experiment based on a two detectors configuration (a near (ND) and a far (FD) detector) is optimized for the measurement of flux and spectrum of the reactor electron antineutrinos. Their measurements are used to observe a disappearance of the $\bar{\nu}_e$ flux as well as a spectral distortion to estimate the value of θ_{13}. The electron antineutrinos interact on the detectors' liquid scintillator (LS) via inverse beta decay (IBD), producing a correlatd pair of signals (called prompt and delay) that corresponds to the detection of a e^+ and n, respectively. This thesis has been focussed on studying the neutron detection efficiency, a key term for understanding neutrino signal. To evaluate this parameter, several contributions need to be considered: the fraction of neutron captures on a particular element of the LS, the efficiency in the neutron selection cuts, and the effect caused by the neutron mobility between detector volumes. In previous Double Chooz analyses, these parameters were evaluated only for the far detector. The results of this thesis provided important inputs for the neutron detection efficiency estimation, with results used in the first DC multi-detector analysis including ND and FD data.
Along this work, the neutron detection efficiency was studied using a ^{252}Cf radioactive source. Radioactive sources can be deployed along the *z-axis* of the ν-target volume, and along the *Guide Tube* in the γ-catcher upper part. This isotope decays via spontaneous fission emitting several neutrons. The produced fission gammas and neutrons create a correlated signal in the detector which is used to estimate the fraction of neutron captured in the different LSs. In addition, Cf neutrons allow to study the efficiency on the IBD neutron selection. The so called *semi-inclusive efficiency* provides information about the visible energy, the coincidence time and the correlation distance selection cuts.

In the ν-target volume, neutrons are mainly captured on Gadolinium (Gd) nuclei. However, they can also be captured on Hydrogen and Carbon nuclei present in the organic LS. The calculation of the Gd neutron capture fraction (*Gd-fraction*) is used to estimate the capture stability in the ν-target volume. This stability was studied by evaluating the capture fraction both time-wise, along the life-time of the detectors, and space-wise, along different source deployment positions.
The deployment data in the ν-target center was compared between different calibration campaigns (four in the FD, two in the ND). The study resulted in a stable Gd neutron capture fraction throughout the campaigns. The spatial dependence of the Gd-fraction was studied along the symmetry axis of the detector, showing a constant behaviour for positions close to the detector center. However, the Gd-fraction dropped significantly for positions close to the ν-target wall. This is caused by the migration of the neutrons to other detector volumes, more concretely to the Gd-free volume surrounding the ν-target, the γ-catcher.
Both detectors showed a stable performance time and space-wise. However, their ratio differed by a statistically significant discrepancy from unity of $(0.25 \pm 0.06)\%$ in the ν-target center using the latest calibration campaign data. A similar offset was also observed in other points along the symmetry axis of the detector and did not correspond to what one would expect from identical detector geometries and liquids.

Together with a data to data analysis, the same z-axis deployment positions were simulated using a Monte Carlo (MC) algorithm. The obtained Gd-fractions from the MC simulation differed from the data value by a relatively large 2%. This was also observed in previous DC analyses. The offset can be explained by a incomplete modelled neutron interactions at low energies. To take into account this data to MC discrepancy, *correction factors* were introduced as the ratio between the Gd-fractions of data and MC. Their main purpose is to correct the data to MC reactor $\bar{\nu}_e$ fluxes for the θ_{13} estimation. In this thesis, the same strategy was also applied to compensate for the detectors data to data discrepancy.
These correction factors are sensitive to systematic effects in the Gd-fraction estimation, where correlated background events related to the Cf are the main source of them and are not possible to tag and subtract. Two different systematic analyses were include in this thesis. The first one studied discrepancies in the low energy regions of the neutron capture spectra. The second one checked the correlation times of Cf events to study the presence of possible correlated background events.

A correction factor of 1.0026 ± 0.0021 (stat+syst) was obtained between data to data using the second to last calibration campaign. The uncertainty was dominated by a high statistical contribution ± 0.0019 (stat) and a systematic effect of the computation method ± 0.0008 (syst). The averaged value between detectors of the data to MC correction factor was 0.9744 and presented a total uncertainty of ± 0.0025 (stat+syst) for the first phase of the far detector data (FD-I), ± 0.0026 (stat+syst) for the second one (FD-II), ± 0.0028 (stat+syst) in the case of the near detector (ND). The uncertainties were limited by the statistics of each sample and cover inter-detector discrepancies. All these values were used for the latest analysis and the θ_{13} estimation presented at [22].

A semi-inclusive correction factor was also obtained for detectors data to MC using the second to last calibration data at the target center. This value was used as a cross-check of the final semi-inclusive efficiency estimation using IBD neutrons. This neutron source is particularly useful to analyse the neutron events in the entire detector volume. These two methods are independent, and can be compared without correlations. The Californium results at the target center were in agreement with the obtained values using both the volume-wide IBD neutrons, and the ones published in the previous analyses.

Finally, the Guide Tube data were analysed, and the results represented an important input for future DC analyses. The γ-catcher deployment positions are closer to the acrylic walls than the target center. Therefore, they are more sensitive to the neutron mobility effect, giving the Gd-fraction a spatial dependence. The second to last calibration campaign data was analysed and the far detector Gd-fractions were in agreement with the obtained values of previous DC analyses. Nevertheless, a discrepancy of around $(2-3)\%$ was observed between data to data. The energy spectra for these positions also presented a discrepancy for high energy regions, probably caused by captures on isotopes other than H.
Several analyses using the Californium neutrons were applied to understand the nature of these events. Low energy events were studied and gamma losses were not observed in Hydrogen captures. These results discarded also the possibility of a position shift in the near detector deployment. Capture times and position reconstructions of near detector high energy events showed no additional Gd captures in the ν-target due to neutron mobility. Instead, they were produced in the same liquid as the low energy events, in the γ-catcher volume.

The different studies using deployment data showed evidences of high energy captures in the near detector γ-catcher volume. The scenario where Gd-compounds are included in the γ-catcher LS was studied as a follow up by simulating a Gd-loaded γ-catcher. The capture times and Gd-fractions for a Gd-loaded MC were in agreement with the near detector data results. The obtained results using the Californium source at the γ-catcher, and additional studies considering other neutron sources provided enough information to conclude the existence of a leak between near detector LS volumes. This fact can not only explain the Gd-captures γ-catcher, but also the target centre discrepancy. Further studies are required in order to understand these LSs mixture and provide an adequate systematic uncertainty for the θ_{13} estimation.

Appendix A

^{252}Cf source deployment information

The data and the MC files are selected for ^{252}Cf fissions and background using an ActionUnit based on the EUppCf252Selection code.

A.1 Second calibration campaign

A.1.1 Z-axis Calibration

Data runs

The files are used from the

- `EUppCalProduction_v4r7p0` (Singles)

The produced files are with the energy scale kESv5. Run list at target center: ***FD*** Table A.1.1.

Table A.1.1: Run information for ^{252}Cf source deployed in the Z-Axis in the ***FD*** from 2nd Calibration Campaign.

Run Number	Position [mm]			Length [s]
	x	y	z	
43705	0	0	0	3 600
43706	0	0	0	3 600
44656	0	0	0	3 600
45042	0	0	0	3 600
45700	0	0	0	1 800
45701	0	0	0	1 800

MC runs

The files are used from the

- `MC_DC3rdPub_ZAXIS_CF252_V6`, Seq# 1-60.

The produced files are with the energy scale kESv5. 150 000 events, with 2 500 events (fission + neutrons) for each detector. Run number at target center **43705**.

A.2 Fourth calibration campaign

A.2.1 Z-axis Calibration

Data runs

The files are used from the

- `EUppCalProduction_v4r8p2` (Singles)

The produced files are with the energy scale kESv10. Run list at target center: ***FD*** Table A.2.1, ***ND*** Table A.2.2.

Table A.2.1: Run information for ^{252}Cf source deployed in the Z-Axis in the ***FD*** from 4th Calibration Campaign.

Run Number	Position [mm]			Length [s]
	x	y	z	
203684	0	0	0	600
203685	0	0	0	1800
203687	0	0	0	1800
203688	0	0	0	1800
203689	0	0	0	1800
203690	0	0	0	1800
203691	0	0	-960	1800
203692	0	0	-960	1800
203693	0	0	+960	1800
203694	0	0	+960	1800
203695	0	0	-1272	1800
203696	0	0	0	1800
203697	0	0	0	1800

Table A.2.2: Run information for ^{252}Cf source deployed in the Z-Axis in the ***ND*** from 4th Calibration Campaign.

Run Number	Position [mm]			Length [s]
	x	y	z	
5217105	0	0	0	3600
5217106	0	0	0	3600
5217107	0	0	0	3600
5217108	0	0	-960	3600
5217109	0	0	+960	3600
5217110	0	0	-1160	3600
5217111	0	0	+1210	3600

MC runs

The files are used from the

- `MC_DCBothDet1stPub_ZAXIS_CF252_v3`, Seq# 1-60.

The produced files are with the energy scale kESv10. 150 000 events, with 2 500 events (fission + neutrons) for each detector. Run number at target center for ***FD*** **203687** and for ***ND*** is **5217105**.

A.2.2 Guide Tube Calibration

Data runs

The files are used from the

- `EUppCalProduction_v4r8p2` (Singles)

The produced files are with the energy scale kESv10. Run list at target center: ***FD*** Table A.2.3, ***ND*** Table A.2.4.

Table A.2.3: Run information for ^{252}Cf source deployed in the Guide Tube in the ***FD*** from 4th Calibration Campaign.

Run Number	Position [mm]			Length [s]
	x	y	z	
206418	13	145.2	1534.9	3600
206419	13	145.2	1534.9	3600
206421	13	1188.0	95.2	1200
206422	13	1188.0	95.2	1200
206424	13	1188.0	95.2	1200
206425	13	1431.0	0.0	1200
206426	13	1431.0	0.0	1200
206427	13	1431.0	0.0	1200
206428	13	1653.7	1425.9	1200
206429	13	1653.7	1425.9	1200
206430	13	1653.7	1425.9	1200
206431	13	1534.5	1516.4	1200
206432	13	1534.5	1516.4	1200
206433	13	1534.5	1516.4	1200
206447	13	1210.2	33.4	1800
206448	13	1245.9	7.6	1800
206449	13	1284.4	0.0	1800
206450	13	1349.5	0.0	1800

Table A.2.4: Run information for ^{252}Cf source deployed in the Guide Tube in the ***ND*** from 4th Calibration Campaign.

Run Number	Position [mm]			Length [s]
	x	y	z	
5215023	13	145	1532	3600
5215024	13	1653.4	1428.4	3600
5215025	13	1536.2	1516.3	3600
5215036	13	1188.0	99.1	3600
5215037	13	1211.5	32.1	1800
5215047	13	1211.5	32.1	1800
5215050	13	1211.5	32.1	1800
5215054	13	1242.3	9.2	1800
5215055	13	1282.3	0.0	1800
5215056	13	1349.5	0.0	1800
5215057	13	1430.7	0.0	3600

MC runs

The files are used from the

- ND MC: `MC_DCBothDet1stPub_GUI DE_TUBE_CF252_v3`, Seq# 1-60.
- ND MC with Gd in γ-catcher: `MC_DCBothDet1stPub_GUIDE_TUBE_CF252_v3_GCGd`, Seq# 1-60.

The produced files are with the energy scale kESv10. 150 000 events, with 2 500 events (fission + neutrons) for each detector. Run number at position $(x, y, z) = (13, 1536.2, 1516.3)$ mm for ***ND*** is **5226632**.

A.3 Fifth calibration campaign

A.3.1 Z-axis Calibration

Data runs

The files are used from the

- `EUppCalProduction_v4r8p6` (Singles)

The produced files are with the energy scale kESv10. Run list at target center: ***FD*** Table A.3.1, ***ND*** Table A.3.2.

MC runs

The files are used from the

- `MC_DCBothDet1stPub_ZAXIS_CF252_v4`, Seq# FD 1-20, ND 1-12.

The produced files are with the energy scale kESv10. 150 000 events, with 2 500 events (fission + neutrons) for each detector. Run number at target center for ***FD*** **216190 - 216214** and for ***ND*** is **5225950 - 5226001** (same runs numbers that data).

Table A.3.1: Run information for ^{252}Cf source deployed in the Z-Axis in the ***FD*** from 5th Calibration Campaign.

Run Number	Position [mm]			Length [s]
	x	y	z	
5225950	0	0	12	3600
5225951	0	0	12	3600
5225952	0	0	12	3600
5225954	0	0	12	3600
5225955	0	0	12	3600
5225956	0	0	12	3600
5225957	0	0	12	3600
5225958	0	0	12	3600
5225959	0	0	12	3600
5225960	0	0	12	3600
5225961	0	0	12	3600
5225962	0	0	12	3600
5225963	0	0	12	3600
5225964	0	0	12	3600
5225965	0	0	12	3600
5225966	0	0	12	3600
5225967	0	0	12	3600
5225968	0	0	12	3600
5225969	0	0	12	3600
5225970	0	0	12	3600
5225971	0	0	12	3600
5225972	0	0	12	3600
5225973	0	0	12	3600
5225974	0	0	12	3600
5225976	0	0	12	3600
5225977	0	0	12	3600
5225978	0	0	12	3600
5225986	0	0	12	3600
5225987	0	0	12	3600
5225988	0	0	12	3600
5225989	0	0	12	3600
5225990	0	0	12	3600
5225991	0	0	12	3600
5225992	0	0	12	3600
5225993	0	0	12	3600
5225994	0	0	12	3600
5225995	0	0	12	3600
5225996	0	0	12	3600
5225997	0	0	12	3600
5225998	0	0	12	3600
5225999	0	0	12	3600
5226000	0	0	12	3600
5226001	0	0	12	2400

Table A.3.2: Run information for ^{252}Cf source deployed in the Z-Axis in the ***ND*** from 5th Calibration Campaign.

Run Number	Position [mm]			Length [s]
	x	y	z	
216190	0	0	12	3600
216191	0	0	12	3600
216192	0	0	12	3600
216193	0	0	12	3600
216194	0	0	12	3600
216195	0	0	12	3600
216196	0	0	12	3600
216197	0	0	12	3600
216198	0	0	12	3600
216199	0	0	12	3600
216200	0	0	12	3600
216201	0	0	12	3600
216202	0	0	12	3600
216203	0	0	12	3600
216204	0	0	12	3600
216205	0	0	12	3600
216206	0	0	12	3600
216207	0	0	12	3600
216208	0	0	12	3600
216209	0	0	12	3600
216210	0	0	12	3600
216211	0	0	12	3600
216212	0	0	12	180
216213	0	0	12	3600
216214	0	0	12	3600

Appendix B

Neutron capture cross sections

The Hydrogen-rich liquid scintillator is an effective neutron moderator. Neutrons are mainly slowed down by elastic scatterings with Hydrogen atoms. This process is known as *thermalization* and occurs for neutron energies in the range of 100 MeV to 10 keV (at which the Hydrogen nucleus can be considered as free proton at rest). Below these energies the neutron capture process becomes relevant, since the neutron capture cross section strongly depends on the kinetic energy of these particles. In Fig. B.0.1a several Gd isotopes and Hydrogen nuclei capture cross sections are represented in terms of the neutron kinetic energy. The cross sections are scaled to the number of Hydrogen nuclei compared to Gadolimum in a unit volume of Double Chooz ν-target scintillator.

Neutrons created by IBD interactions will reach after several scatterings the energy range at which the neutron capture cross section becomes relevant. The neutron thermalization is in general a fast process (few µs), while the neutron capture time in Gd nuclei is $\sim$ 30µs. For that reason, the correlation time spectra in Fig. B.0.1b for Gd captures presents a rising part until a maximum (thermalization time, which depends on the scintillator composition) and an exponential decay with a decay constant (the capture time). Since the effective capture cross section for Gd is larger than the elastic scattering cross section (see Fig. B.0.1b), the majority of the neutrons will reach thermal energies and are captured on Gd. However, knowing the relative abundance of Hydrogen

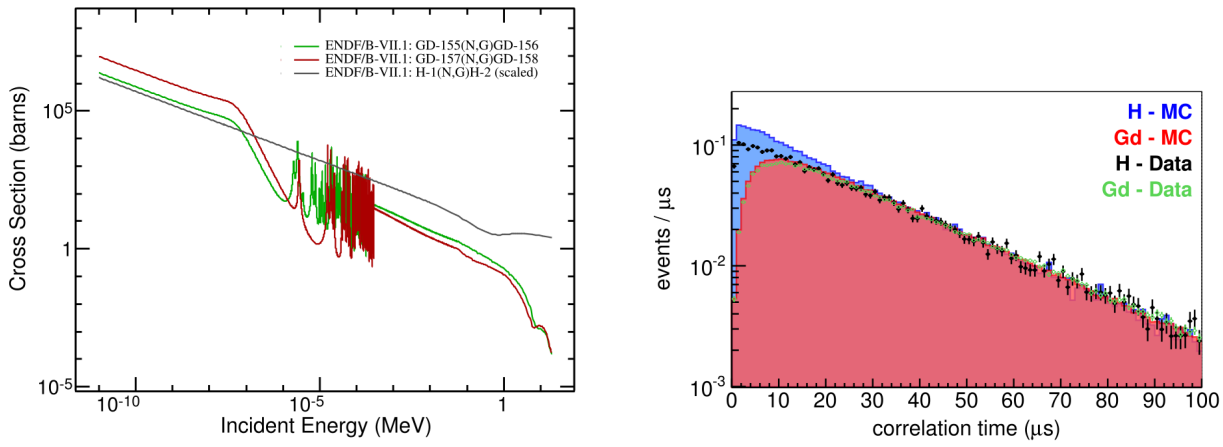

(a) **(b)**

Figure B.0.1: **(a)** Capture cross section of Gd (^{155}Gd in green and ^{157}Gd in red) and the scaled cpature cross section of Hydrogen (gray) [41]. **(b)** Correlation time of neutron captures in ^{252}Cf data and MC: H-captures (black points) and Gd-captures (green open circles) in data, and H-captures (blue filled histogram) and Gd-captures (red-filled histogram) in MC simulation [58].

atoms compared to Gd nuclei, the capture cross-section of H is larger in the keV range than for Gd. Therefore, neutrons do not need to be significantly slowed down to observe a neutron capture on H, and no rising part is seen in the capture time spectra (see Fig. B.0.1b). Consequently, the largest fraction of capture in the ν-target will occur on H- and Gd-nuclei with a mean capture time of 30 µs. And in the γ-catcher liquid scintillator captures will be on H-nuclei more than 99% of the times, with a capture time about 200 µs factor seven lower compared to the ν-target due to the lower cross section at thermal energies.

In Fig. B.0.1b also the simulated capture time spectra for Gd and H nuclei are included. It is possible to notice a discrepancy between H capture distribution shapes at low correlation times. The simulated distribution has a faster component in the first 30µs compared to the data, caused by an imperfect implementation of the neutron capture or elastic scattering cross section.

Acknowledgements

Firstly, I would like to express my sincere gratitude to my advisor Prof. Dr. Manfred Lindner for giving me the opportunity to write my thesis in the Max-Planck Institut für Kernphysik, and to work on the Double Chooz experiment. I would also like to thank Prof. Dr. Hans-Christian Schultz-Coulon for agreeing to be one of my thesis referees.

I would also thank the entire "*Reactor Neutrino Group*". Specially, I thank Dr. Christian Buck for his continuous support on my studies and related research, and Dr. Julia Haser for her guidance and motivation during all the time of research and writing this thesis. I could not have imagined better advisors and mentors for my thesis. I would also like to thank Dr. Antoine Collin for his help during my firsts months in the Institute, and Dr. Stephan Schoppmann for his conversations while I was writing this thesis. I would like to thank also Christian Roca for everything I learnt with him in the *Faraday Labor*, and the endless discussions about physics.

My sincere thanks also goes to the people in the Lindner division, mainly to the "*Xenon Group*" for the good times during the last year. I would also like to thank Priv.-Doz. Dr. Teresa Marrodán Undagoitia, her conversations and advices always motivated me.

Many thanks go to the colleagues of the Double Chooz Collaboration. Working together during last year I grew up as a physicist. I would like to thank Dr. Anatael Cabrera and Dr. Inés Gil-Botella, for their helpful suggestions and discussions. Special thanks go to Diana Navas-Nicolás for being the best collegue during the endless days she was working at the Max-Planck Institute, and a good friend during the last year.

Finally, I would like to thank Marta for her friendship during last months. I thank also Daniel and Veronica, for the time we spent during the last two years. Many thanks to Virgi and Andréé, for the great time together being the best fellow adventurers I could ever had. Specially, I thank my friend Emerick, for being a big support and for his advices always in the best moment.
And last but not the least, I would like to thank my family: sin mis padres y mi hermano no habría podido llegar a escribir esta tesis, ni llegar a donde estoy en mi vida en general; gracias por estar siempre ahí y haberme ayudado a crecer como persona.

Bibliography

[1] W. Pauli, Letter to a group of physicis in a meeting in Tübingen December (1930) http://microboone-docdb.fnal.gov/cgi-bin/RetrieveFile?docid=953;filename=pauli%20letter1930.pdf

[2] E. Fermi, *"Versuch einer Theorie der beta-Strahlen"*, I". Zeitschrift für Physik (in German). 88: 161 (1934).

[3] C. L. Cowan, Jr., F. Reines, F. B. Harrison, H. W. Kruse and A. D. McGuire, *"Detection of the Free Neutrino: A Confirmation"*, Science 124, 103 (1956).

[4] B. Pontecorvo, *"Electron and muon neutrinos"* Z theor. exp. physics. 37,1751 (1959).

[5] I.M. Vasilevsky et al, *"Search for anomalous scattering of muon neutrinos by nucleons"*, Phys.Lett 1,345 (1962).

[6] K. Kodama et al. (DONUT Collaboration) *"Observation of tau neutrino interactions"*, Physics Letters B . 504 (3): 218 (2001).

[7] B. Pontecorvo, *"Mesonium and anti-mesonium"*, Sov. Phys. JETP, 6:429 (Zh.Eksp.Teor, 33, 549, 1957), (1957).

[8] B. Pontecorvo. *"Inverse beta processes and nonconservation of lepton charge"*, Sov. Phys. JETP, 7:172–02, (Zh.Eksp.Teor.fiz, 34, 247, 1957), (1958).

[9] S. Fukuda et al., *"Solar ^8B and hep Neutrino Measurements from 1258 Days of Super-Kamiokande Data"*, Phys. Rev. Lett. 86, 5651, (2001).

[10] Q. R. Ahmad et al., *"Measurement of the Rate of $\nu_e + d \rightarrow p + p + e^-$ Interactions Produced by ^8B Solar Neutrinos at the Sudbury Neutrino Observatory"*, Phys. Rev. Lett. 87, 071301, (2001).

[11] I. Gil-Botella, *"Neutrino physics"*, CERN Yellow Report CERN-2013-003, pp.157-206 (2015).

[12] K. Zuber, *"Neutrino Physics"*, CRC Press (2012).

[13] C. Giunti, C. W Kim, *"Fundamentals of neutrino physics and astrophysics"*, Oxford University Press (2007).

[14] C. Buck, *"The Double Chooz experiment"*, Talk at Deutsche Physikalische Gesellschaft (DPG) Heidelberg (2015).

[15] C. Bemporad, G. Gratta, P. Vogel, *"Reactor-based neutrino oscillation experiments"*, Rev.Mod.Phys.74:297 (2002).

[16] T. A. Mueller et al, *"Improved predictions of reactor antineutrino spectra"*, Phys. Rev. C 83, 054615 (2011).

[17] P. Huber, *"Determination of antineutrino spectra from nuclear reactors"*, Phys. Rev. C 84, 024617 (2011).

[18] P. Vogel, L.J. Wen, C. Zhang, *"Neutrino oscillation studies with reactors"*, Nature Communications 6, 6935 (2015).

[19] Double Chooz Collaboration, *"Indication for the disappearance of reactor $\overline{\nu}_e$ in the Double Chooz experiment"*, Phys. Rev. Lett. 108, 131801, (2012).

[20] K. A. Olive et al. (Particle Data Group), Chin. Phys. C, 38, 090001 (2014).

[21] T. Konno, Talk at *"Moriond Cosmology 2012"* conference, La Thuile, (2012).

[22] M. Ishitsuka on behalf of the Double Chooz Collaboration, *"New Results of Double Chooz"*, Talk on 51st Rencontres de Moriond (2016).

[23] C. Aberle, C. Buck, B. Gramlich, F.X. Hartmann, M. Lindner, S. Schönert, U. Schwan, S. Wagner and H. Watanabe, *"Large scale Gd-beta-diketonate based organic scintillator production for antineutrion detection"*, JINST 7, P11006 (2012)

[24] C. Aberle, C. Buck, F.X. Hartmann, and S. Schönert, *"Light yield and energy transfer in a new Gd-loaded liquid scintillator"*, Chem. Phys. Lett. 5216, 257 (2011)

[25] Double Chooz Collaboration, *"First Measurement of θ_{13} from Delayed Neutron Capture on Hydrogen in the Double Chooz Experiment"*, Phys. Lett. B723 66-70, (2013).

[26] E. Calvo, M. Cerrada, C. Fernández-Bedoya, I. Gil-Botella, C. Palomares, I. Rogríguez, F. Toral and A. Verdugo, *"Characterization of large-area photomultipliers under low magnetic fields: Design and performance of the magnetic shielding for the Double Chooz experiment"*, Nucl. Instrum. Methods Phys. Res., Sect. A 621, 222 (2010).

[27] E. Blucher et al, *"OV documentation"*, Double Chooz Internal Document, DC-doc-1400-v3 (2010).

[28] J. Busenitz et al., *"Plan for deployment of radioactive sources"*, Double Chooz Internal Document, DC-doc-2049-v2, (2010).

[29] P. Vogel and J. F. Beacom, *"Angular distribution of neutron inverse beta decay"*, Phys. Rev. D 60, 053003 (1999).

[30] A. Pichlmaier, V. Varlamov, K. Schreckenbach, and P. Geltenbort, *"Neutron lifetime measurement with eh UCN trap-in-trap MAMBO II"*, Phys. Lett. B 693, 221 (2010).

[31] IAEA [International Atomic Energy Agency]: *Database of Prompt Gamma Rays from Slow Neutron Capture for Elemental Analysis*, `http://www-pub.iaea.org/books/`, STI/PUB/1263 (ISBN:92-0-101306-X), (2007).

[32] Double Chooz Collaboration, *"Improved measurements of the neutrino mixing angle θ_{13} with the Double Chooz detector"*, JHEP 10 (2014) 086.

[33] Double Chooz Collaboration, *"Measurement of θ_{13} in Double Chooz detector using neutron captures on Hydrogen with novel background rejection techniques"*, JHEP 01 (2016) 163.

[34] Double Chooz Collaboration, *"Characterization of the Spontaneous Light Emission of the PMTs used in the Double Chooz Experiment"*, JINST 11 (2016) no.08, P08001.

[35] Double Chooz Collaboration, *"Reactor $\bar{\nu}_e$ disappearance in the Double Chooz experiment"*, Phys. Rev. D86, 052008, (2012).

[36] P. Adamson et al., *"Combined Analysis of ν_μ Disappearance and $\nu_\mu \to \nu_e$ Appearance in MINOS Using Accelerator and Atmospheric Neutrinos"*, Phys. Rev. Lett. 112, 191801 (2014).

[37] Elements Data Base, *"Californium A=98"*, `http://www.elementsdatabase.com` (2015).

[38] Landolt-Bornstein New Book Series, *"Subvolume A1 – Low Energy Neutrons and their Interaction with Nuclei and Matter. Part 1: 9. Nuclear fisson, 9.3 Fission neutrons - 9.4 Fission gammas"*, Volume: 16A1, ISBN: 978-3-540-60857-8, Springer-Verlag (2000) `http://www.springermaterials.com/docs/bookshelf.html`

[39] B. E. Watt, *"Energy Spectrum of Neutrons from Thermal Fission of ^{235}U"*, Phys. Rev. 87, 1037 (1952).

[40] L. Cranberg, G. Frye, N. Nereson and L. Rosen, *"Fission Neutron Spectrum of ^{235}U"*, Phys. Rev. 103, 662 (1956).

[41] J. Haser, *"Neutrino detection uncertainties in the θ_{13} analysis of the Double Chooz experiment"*. Chapter 4, Section 4.3 *"Background reduced fission neutron data"*, Dissertation Uni-

versity of Heidelberg (2015) .

[42] C. Palomares, *"Accidental BG" - Accidental estimation for DC-IV Gd++ and Gd*, Double Chooz Internal Document, DC-doc-6739-v7 (2016).

[43] H. Almazan, E. Chauveau and R. Sharankova, *"ESv11 Systematics"*, Double Chooz Internal Document, DC-doc-6792-v2 (2016).

[44] J. Haser, *"Neutrino detection uncertainties in the θ_{13} analysis of the Double Chooz experiment"*. Chapter 5, Section 5.4 *"Gd-fraction correction: ^{252}Cf fission neutron analysis"*., Dissertation University of Heidelberg (2015)

[45] R. J. Barlow, *"A guide to the use of statistical methods in the physical sciences."*, ISBN: 0-471-92295-1, Wiley (1999)

[46] Double Chooz Collaboration, *"Measurement of θ_{13} in Double Chooz using neutron captures on Hydrogen with novel background rejection techniques"*, JHEP 01 (2016) 163.

[47] J. Haser and G. Yang, *"n-Gd DC3rdPub Cf-252 Neutron Detection Efficiency Blessing Plots"*, Double Chooz Internal Document, DC-doc-5500-v9 (2014).

[48] D. Navas-Nicolás, *"IBD method: ND+FD efficiency analysis"*, Double Chooz Internal Document, DC-doc-6539-v2 (2016).

[49] Double Chooz Analysis Group, *"Internal note of DC-III neutrino oscillation analyses using energy spectrum"*, Double Chooz Internal Document, DC-doc-5162-v23 (2013).

[50] J. Haser, *"H-fraction stability check using GT 1st and 2nd calibration campaign data"*, Double Chooz Internal Document, DC-doc-4512-v3 (2013).

[51] C. Alt, *"Vertex reconstruction systematics"*, Double Chooz Internal Document, DC-doc-6268-v1 (2015).

[52] C. Buck, *"Cf in GC"*, Double Chooz Internal Document, DC-doc-6630-v1 (2016).

[53] C. Buck, *"Gd in GC Summary"*, Double Chooz Internal Document, DC-doc-6735-v1 (2016).

[54] G. Yang, *"GC issue with new Cf data in GT "*, Double Chooz Internal Document, DC-doc-6711-v1 (2016).

[55] G. Yang, *"GC issue continue with Cf"*, Double Chooz Internal Document, DC-doc-6727-v1 (2016).

[56] T. J. C. Bezerra, *"GC analysis using spallation and IBD neutrons"*, Double Chooz Internal Document, DC-doc-6729-v2 (2016).

[57] D. Navas-Nicolás, *"Cv Delta T scan analysis"*, Double Chooz Internal Document, DC-doc-6714-v2 (2016).

[58] J. Haser, *"Neutrino detection uncertainties in the θ_{13} analysis of the Double Chooz experiment"*. Chapter 7, Section 7.3 *"Neutron scattering and Monte Carlo models"*, Dissertation University of Heidelberg (2015) .

Erklärung:

Ich versichere, dass ich diese Arbeit selbstständig verfasst habe und keine anderen als die angegebenen Quellen und Hilfsmittel benutzt habe.

Heidelberg, den (Datum) .....